Dissertation
submitted to the
Combined Faculties for Natural Sciences and for Mathematics
of the Ruperto-Carola University of Heidelberg, Germany
for the degree of
Doctor of Natural Sciences

presented by
Dipl.-Phys. Sascha Benjamin Reinhardt
born in Ellwangen(Jagst)
Oral examination: 23th November, 2005

Measurement of Time Dilation by Laser Spectroscopy on Fast Stored Lithium Ions

Referees:
Prof. Dr. Dirk Schwalm
Prof. Dr. H.-Jürgen Kluge

Zusammenfassung

In der hier vorgelegten Arbeit werden Frequenzmessungen an schnellen Lithium Ionen als Test der Zeitdilatation vorgestellt. Die Messungen sind am Speicherring TSR am Max-Planck-Institut für Kernphysik durchgeführt worden. Die Übergangsfrequenz eines Zwei-Niveau-Systems im Lithium Ion wird bestimmt, indem eine dopplerfreie Fluoreszens-Sättigungsspektroskopie verwendet wird. Die Spektroskopie wird durch zwei gegenläufige Laser verwirklicht, die kollinear zum Ionenstrahl sind. Zwei Messungen bei zwei verschiedenen Ionengeschwindigkeiten werden durchgführt, eine Messung bei 3 % Lichtgeschwindigkeit und eine bei 6,4 % Lichtgeschwindigkeit. Die gemessenen Übergangsfrequenzen werden mit der Voraussage der Speziellen Relativitätstheorie verglichen. Auch der Einfluß von magnetischen Feldern und Lichtkräften wird untersucht.
Für den Parameter $\hat{\alpha}$, der die Abweichung der Zeitdilatation von der Speziellen Relativitätstheorie in der Testtheorie von Robertson-Mansouri-Sexl angibt, wird ein Wert von $(-6.5 \pm 9.5) \cdot 10^{-8}$ bestimmt.

Abstract

In this work frequency measurements on fast lithium ions as a test of time dilation are presented. The measurements are carried out at the Max Planck Institute for Nuclear Physics in Heidelberg using the storage ring TSR. The transition frequency of a two-level system in the lithium ion is measured using a Doppler-free fluorescence saturation spectroscopy. The spectroscopy is realized by two counter-propagating lasers that are collinearly aligned with the stored ion beam. Two measurements are carried out, one at a ion velocity of 3% speed of light and one at 6.4% speed of light. The measured transition frequencies are compared with the prediction of Special Relativity. The influence of magnetic fields and light forces are also discussed.
For the parameter $\hat{\alpha}$, that describes the deviation from the time dilation of Special Relativity, of the test theory of Robertson-Mansouri-Sexl a value of $(-6.5 \pm 9.5) \cdot 10^{-8}$ is obtained.

Contents

Chapter 1

Introduction

The goal of physics is to improve the understanding and description of Nature. Every new development in theory, experiment or technology can trigger new impulses on other areas. This happened also one century ago, when Albert Einstein published his work "Zur Elektrodynamik bewegter Körper" in 1905 [Ein05]. The ideas presented in this work are known today as Special Relativity (SR) and provided a new view on time and space. Many experiments were carried out to look for deviations from the predictions of the SR. Three types of experiments are normally used to test SR. The first one was first carried out by A. A. Michelson (1881) and E. Morley (1887), even before SR existed to detect the so called ether, that was assumed to be the carrier of the electromagnetic waves. In this experiment the variation of the speed of light c as a function of the direction with respect to the ether is investigated, but the expected dependence on the direction was not found. The second one was first carried out by Thorndike and Kennedy (1932). In their experiment it is investigated, if the speed of light depends on the velocity of the system. The third and last one was first realized by Ives and Stilwell (1938); they measured the Hβ-emission wavelength from fast moving hydrogen atoms produced in a canal ray tube in different directions. This type of experiment is sensitive to time dilation, that is predicted in the SR and describes that "moving clocks running slower than clocks at rest".

In the experiments discussed in this thesis the time dilation factor is measured by Doppler-free fluorescence saturation spectroscopy on fast lithium ions, i. e. it is an Ives-Stilwell type experiment. To obtain the highest possible sensitivity, however several changes have been are used that have became available since the original experiment in 1938. With the development of the laser it is now possible to produce controllable collimated quasi-monochromatic light sources, that are necessary for precision frequency measurements. To measure the frequency ν_0 of a transition in the lithium ions, that fly with the velocity v of up to 6.4% speed of light c collinear with the laser light, the frequency ν_p of the laser parallel to the ions must be detuned according to the relativistic Doppler effect

$$\nu_p \;=\; \nu_0 \gamma \left(1 + \frac{v}{c}\right).$$

Here $\gamma = 1/\sqrt{1-(v/c)^2}$ is the time dilation factor as predicted by Special Relativity.

Because velocities can not be measured with the desired precision, a second laser counter-propagating to the ion beam is applied with the frequency

$$\nu_a = \nu_0 \gamma \left(1 - \frac{v}{c}\right).$$

By multiplying the two laser frequencies for the case if they interact with ions of the same velocity class v this velocity drops out

$$\nu_a \nu_p = \nu_0^2.$$

So only frequencies need to be measured to verify if the time dilation factor has the form required by Special Relativity. To ensure that both lasers talk to ions of the same velocity, a saturation spectroscopy is used, which was developed in the sixties of the last century [SJ63], to solve this problem. The principle is that the two counter-propagating lasers interact simultaneous with the ions if both lasers try to talk to the ions of the same velocity the transition is saturated and a so-called Lamb dip is observable in the fluorescence spectrum recorded by a photomultiplier (s. figure 1.1).

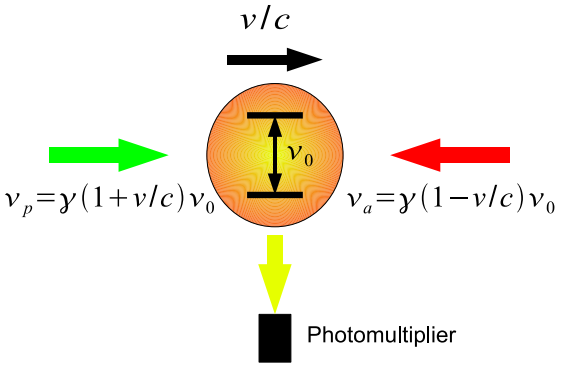

Figure 1.1: Principle of the time dilation experiment.

The width of the Lamb dip is limited by the natural linewidth of the transition, that is for the lithium ion only several MHz, which is small compared to the width of the velocity distribution in the GHz region. So it is possible to determine the absolute frequency of the Lamb dip with an uncertainty in the order of 100 kHz, i. e. a relative accuracy of 10^{-10}. It is also no problem to control the frequency of a laser better than the 10^{-10} level. In sophisticated applications levels of 10^{-16} are reached [HOW+05]. So frequency nowadays are one of the best measurable physical quantity. For the verification of the time dilation factor ν_a and ν_p must be measured, when they interact both with the same ions that have the transition frequency ν_0 known from another measurement. In previous TSR based experiments the limited knowledge of ν_0 limited the sensitivity of the experiment. As it is in chapter 2 demonstrated the relationship between ν_a, ν_p and ν_0 is modified if a more general transformation than the transformation of SR is used for testing SR. The modified relationship is

$$\nu_a \nu_p = \nu_0^2 \left(1 + 2\hat{\alpha} \left(\frac{v}{c}\right)^2\right).$$

An additional velocity depending term is introduced. For SR the parameter $\hat{\alpha}$ is zero. The sensitivity of the experiment gets higher for higher velocities due to $(v/c)^2$ dependence. If two different measurements at two different ion velocities are performed then the transition frequency ν_0 and $\hat{\alpha}$ can be determined independently. The topics of this thesis are frequency measurements at two different lithium ion velocities, i. e. at 3%

and 6.4% speed of light, as test of time dilation.
Beyond the frequency measurement, also the stored lithium ion beam must have excellent properties, because the ion beam and the laser beam must be overlapped as good as possible. So the ion beam must have a small divergence and must be stable in space to reduce the influence of systematic errors. This is fulfilled by the storage ring Test-Storage-Ring (TSR) of the Max Planck Institute for Nuclear Physics. With the built-in electron cooler an ion beam with high stability in energy and space can be produced [Beu00]. Also the width of the velocity distribution is very small compared to the mean velocity of the ions. A ratio of 10^{-5} can be given as a quality factor.

With these conditions the first measurements of the time dilation factor at the TSR was carried out by Roman Klein in 1991 [Kle91]. These measurements were improved by Ralf Grieser in 1994 [Gri94] and gave the best upper limit for deviation of the time dilation until the work of Guido Saathoff in 2002 [Saa02][SKE$^+$03] further improved the understanding and sensitivity of the experiment. The present work is directly connected to the work of Saathoff and is the first measurement of the transition frequency of lithium ions at 3% speed of light.

The thesis starts with a short introduction to the theory of Special Relativity and presents test theories for proving SR. The next four chapters describe the different parts of the experimental setup. First the properties of the $^7Li^+$-ion is discussed, that is stored in the storage ring. The explanations of the properties and physics of a stored ion beam in the TSR is treated in the following chapter. The next chapter discusses the setup for the frequency measurement and control of the lasers used the lithium spectroscopy which is explained in the following chapter. In the last two chapters the results together with conclusion and an outlook are given.

Chapter 2

Special Relativity and Test Theories

A short review of Special Relativity is given together with some relations important for the experiment. Because the experiment is intended to be a test of time dilation, test theories are also explained. The kinematical Robertson-Mansouri-Sexl test theory is discussed in detail. Additionally, a short treatment within a dynamical test theory, the so called Standard Model Extension, is presented. From the physical point of view the dynamical test theory is more rigorous, because it describes the modifications of the interactions and not only the modification of the kinematics. But as the kinematical test theories are more intuitive, the discussion of the time dilation tests are restrict to the Robertson-Mansouri-Sexl test theory.

2.1 Einsteins postulates and Lorentz transformation

The kinematical part of Special Relativity or Lorentz transformation is based on two postulates of Einstein.

Relativity principle

In every inertial frame the laws of physics are the same. There is no possibility to detect absolute motion and no preferred frame exist.

Constancy of the speed of light

The speed of light c in vacuum is constant and equal in all inertial frames.

With this two postulates it is possible to deduce the Lorentz transformation [SS83]. The Lorentz transformation between two inertial frames where the axes are parallel and the frame $I'(x', y', z', t')$ moves at a velocity v along the x-axis of the frame $I(x, y, z, t)$ is

given by

$$\begin{aligned} x' &= \gamma(x - vt) && (2.1)\\ y' &= y && (2.2)\\ z' &= z && (2.3)\\ t' &= \gamma\left(t - \frac{v}{c^2}x\right) && (2.4)\\ \gamma &= \frac{1}{\sqrt{1 - \left(\frac{v}{c}\right)^2}}. && (2.5) \end{aligned}$$

The electric field vector $\vec{E}$ of a monochromatic plane wave with the frequency ν in I is given by

$$\vec{E}(\vec{x}) = \vec{E_0} e^{i(\omega t - \vec{k}\vec{x})}. \quad (2.6)$$

$\omega = 2\pi\nu$ is the angular frequency of the wave, $\vec{k}$ is the wave number vector with an absolute value of ω/c. The phase $\phi = \omega t - \vec{k}\vec{x}$ is a Lorentz invariant and does not change when transformed from one frame to another frame

$$\begin{aligned} \phi &= \omega t - \vec{k}\vec{x} = \omega' t' - \vec{k'}\vec{x'} && (2.7)\\ &= \omega t - kx\cos(\theta) = \omega' t' - k' x' \cos(\theta'). && (2.8) \end{aligned}$$

Because the angular frequency is nothing else than the time derivative of the phase, the observed frequency $\nu' = \omega'/(2\pi)$ in I' can be determined as $\nu' = 1/(2\pi) \cdot d\phi/dt'$. As a result, the relativistic Doppler formula is obtained

$$\boxed{\nu' = \nu\gamma\left(1 - \tfrac{v}{c}\cos(\theta)\right),} \quad (2.9)$$

where θ is the angle between the direction of the wave and the direction of motion of I' with respect to I, measured in I.

If the wave is parallel ($\theta = 0°$) or antiparallel ($\theta = 180°$) to the direction of motion and ν' should be equal for both cases, the frequency ν_p for $\theta = 0°$ and ν_a for $\theta = 180°$ is given by

$$\begin{aligned} \nu' &= \nu_p \gamma\left(1 - \frac{v}{c}\right) && (2.10)\\ \nu' &= \nu_a \gamma\left(1 + \frac{v}{c}\right). && (2.11) \end{aligned}$$

By multiplying the last two formulas, a formula is obtained, which is in the focus of the present work:

$$\begin{aligned} \nu'^2 &= \nu_p \nu_a \gamma^2 \left(1 - \frac{v}{c}\right)\gamma\left(1 + \frac{v}{c}\right)\\ \nu'^2 &= \nu_p \nu_a \frac{1}{1 - \frac{v^2}{c^2}}\left(1 - \frac{v^2}{c^2}\right)\\ \nu'^2 &= \nu_p \nu_a. && (2.12) \end{aligned}$$

The last equation may be called the "Golden equation" and will be tested in the present experiment.

2.2 Robertson-Mansouri-Sexl Test Theory

The principles of the Robertson-Mansouri-Sexl Test Theory (RMS) were formulated by Robertson in 1949 [Rob49]. The work of Robertson postulated a preferred reference frame Σ. In this frame, the velocity of light is assumed to be isotropic and to propagate rectilinearly with a constant velocity c. The other postulate is that only the velocity vector is significant for the transformation into another reference frame. For the clock synchronization the Einstein synchronization[1] is chosen. From this postulates the transformation between the preferred frame and frame S moving with the velocity v is deduced. Compared to the Lorentz transformation, this transformation contains three additional velocity dependent parameters. Robertson showed that three types of experiments are sufficient to verify, if this general transformation is equal to the Lorentz transformation.

Michelson-Morley type experiments test, if *the total time required for light to traverse, in free space, a distance l and to return is independent of its direction.*

Kennedy-Thorndike type experiments test, if *the total time required for light to traverse a closed path in S is independent of the velocity v of S relative to Σ.*

Ives-Stilwell type experiments test, if *the frequency of a moving atomic source is altered by the factor $(1 - v^2/c^2)^{1/2}$, where v is the velocity of the source with respect to the observer.*

In 1976 Mansouri and Sexl formulated a test theory, that is based on Robertson test theory [MS77a][MS77b][MS77c]. The difference between the two works is, that Mansouri and Sexl makes a more general assumptions for clock synchronization. Today the theory of Mansouri and Sexl is commonly used as a kinematic test theory for the description of these experiments and, because of the close relationship between Robertsons test theory and Mansouri-Sexl test theory, this test theory is usually called Robertson-Mansouri-Sexl test theory (RMS).

The transformation equation between the preferred frame Σ with coordinates (X,Y,Z,T) and a frame S with coordinates (x,y,z,t) moving with the velocity[2] v with respect to Σ is given by

$$t = a(v)T + \epsilon_1 x + \epsilon_2 y + \epsilon_3 z \tag{2.13}$$
$$x = b(v)(X - vT) \tag{2.14}$$
$$y = d(v)Y \tag{2.15}$$
$$z = d(v)Z. \tag{2.16}$$

[1] The Einstein synchronization uses a light signal that is emitted from position x_0 at $t = 0$ and is reflected back from the position x_1. The light signal reaches x_0 at the time $t = t_0$ so it is assumed that a clock at x_1 records the time $t_0/2$, when the light reaches x_1.

[2] All velocities are given in units of speed of light c_0 in Σ.

Whereby - without loss of generality - the following kinematical restrictions are assumed:

- x-axes and X-axes are parallel
- the (x,z)-plane coincide with (X,Z)-plane all the time
- the origin of S moves along the X-axis with the velocity v.

The other restriction is that in Σ the velocity of light c_0 is isotropic. The functions ϵ_1, ϵ_2 and ϵ_3 are determined by the procedure of synchronization. The functions $a(v)$, $b(v)$ and $d(v)$ are determined by experiment or theory like Special Relativity. For Einstein synchronization, that is the only method considered here, ϵ_1, ϵ_2 and ϵ_3 are

$$\epsilon_1 = -\frac{av}{b(1-v^2)} \quad , \quad \epsilon_2 = 0 \text{ and } \epsilon_3 = 0.$$

Because using the Einstein synchronization, the one-way speed of light can not be measured anymore due to the back and forth movement of the light for synchronization. For moderate velocities it is common to expand the functions in orders of v^2, because of the insensitivity to the one-way speed of light

$$a(v) = 1 + \left(\hat{\alpha} - \frac{1}{2}\right) v^2 + \left(\hat{\alpha}_2 - \frac{1}{8}\right) v^4 + \ldots \tag{2.17}$$

$$b(v) = 1 + \left(\hat{\beta} + \frac{1}{2}\right) v^2 + \left(\hat{\beta}_2 - \frac{1}{8}\right) v^4 + \ldots \tag{2.18}$$

$$d(v) = 1 + \hat{\delta} v^2 + \hat{\delta}_2 v^4 + \ldots . \tag{2.19}$$

The velocity independent coefficients are defined such that they are vanishing for the case of Special Relativity. In this case $a(v)$, $b(v)$ and $d(v)$ is given by

$$a(v) = \sqrt{1-v^2} \tag{2.20}$$

$$b(v) = \frac{1}{\sqrt{1-v^2}} \tag{2.21}$$

$$d(v) = 1. \tag{2.22}$$

In [MS77a] the velocity of light in S $c(\theta)$ is calculated up to the second order of v

$$\frac{c_0}{c(\theta)} = 1 + \left(\hat{\beta} + \hat{\delta} - \frac{1}{2}\right) v^2 \sin^2\theta + (\hat{\alpha} - \hat{\beta} + 1) v^2. \tag{2.23}$$

θ is the angle between the direction of light and $\vec{v}$. The experiments to measure the parameters are the Michelson-Morley experiment that measures $(\hat{\beta} + \hat{\delta})$, the Kennedy-Thorndike experiment that measures $(\hat{\alpha} - \hat{\beta})$ and the Ives-Stilwell experiment that measure $\hat{\alpha}$. The best known Michelson-Morley experiment gives a value of $(0.5 \pm 3 \pm 0.7) \cdot 10^{-10}$[AOGS05]/$(-0.9 \pm 2.0) \cdot 10^{-10}$[STW$^+$05]. For the Kennedy-Thorndike experiment the best known value is $(1.6 \pm 3.0) \cdot 10^{-7}$ [WTB$^+$04].

2.3 The TSR experiment in the RMS-Test theory

The Ives-Stilwell experiment is analyzed by Kretzschmar [Kre92] in the formalism of the RMS-test theory. Three frames are necessary to describe the experiment. The frame Σ with coordinates $(\vec{X}, T)$ is the preferred frame, the so called ether frame. One frame is the laboratory frame S' with the coordinates $(\vec{x'}, t')$, where the lasers are at rest. The third frame is the rest frame S of the lithium ion with coordinates $(\vec{x}, t)$. The general transformation equations between Σ and S in RMS are

$$t = aT + \vec{\epsilon}\vec{x} = (\hat{a} - \hat{b}\vec{\epsilon}\vec{v})T + \hat{b}(\vec{\epsilon}\hat{\vec{n}})(\hat{\vec{n}}\vec{X}) + \hat{d}(\vec{\epsilon}[\vec{X} - \hat{\vec{n}}(\hat{\vec{n}}\vec{X})]) \quad (2.24)$$

$$\vec{x} = -\hat{b}T\vec{v} + \hat{b}\hat{\vec{n}}(\hat{\vec{n}}\vec{X}) + \hat{d}(\vec{X} - \hat{\vec{n}}(\hat{\vec{n}}\vec{X})). \quad (2.25)$$

$\hat{\vec{n}}$ is the unit vector in the direction of $\vec{v}$, which is the velocity of S relative to Σ. And the same for S' moving with the velocity $\vec{v'}$ relative to Σ

$$t' = a'T + \vec{\epsilon'}\vec{x'} \quad (2.26)$$

$$\vec{x'} = -\hat{b'}T\vec{v'} + \hat{b'}\hat{\vec{n'}}(\hat{\vec{n'}}\vec{X}) + \hat{d'}(\vec{X} - \hat{\vec{n'}}(\hat{\vec{n'}}\vec{X})). \quad (2.27)$$

Using these two sets of transformation equations, coordinates in S and S' can be connected. A time difference $\Delta t'$ in S' is connected with a time difference Δt in S by

$$\Delta t = \Gamma(\vec{v}, \vec{v'})\Delta t'. \quad (2.28)$$

$\Gamma(\vec{v}, \vec{v'})$ is comparable to the time dilation factor in Special Relativity and has the form

$$\Gamma(\vec{v}, \vec{v'}) = \frac{\hat{a}}{\hat{a'}} + \frac{\hat{b}}{\hat{b'}}(\vec{\epsilon}[\hat{\vec{n}}(\hat{\vec{n}}\vec{v} - \vec{v})]) + \frac{\hat{d}}{\hat{a'}}(\vec{\epsilon}[\vec{v'} - \hat{\vec{n}}(\hat{\vec{n}}\vec{v'})]). \quad (2.29)$$

In Special Relativity the form is

$$\Gamma_{SR}(\vec{v}, \vec{v'}) = \frac{1 - \vec{v}\vec{v'}}{\sqrt{(1 - v^2)(1 - v'^2)}} = \frac{1}{1 - \beta_{SR}^2}, \text{ with} \quad (2.30)$$

$$\beta_{SR} = \frac{\sqrt{(\vec{v'} - \vec{v})^2 - (\vec{v} \times \vec{v'})^2}}{1 - \vec{v}\vec{v'}}. \quad (2.31)$$

The Doppler formula for a light beam with the frequency $\nu^{\pm}$ in S' seen by an observer in S moving parallel or antiparallel to the light beam as frequency ν_0 is now given by

$$\frac{\nu^{\pm}}{\nu_0} = \frac{\alpha(v^2)}{\alpha(v'^2)} \cdot \frac{1 \pm \beta_{SR}}{\sqrt{1 - \beta_{SR}^2}}. \quad (2.32)$$

Here $a(v^2) = \sqrt{1 - v^2} \cdot \alpha(v^2)$ and $a(v'^2) = \sqrt{1 - v'^2} \cdot \alpha(v'^2)$ are introduced. $\alpha(v^2)$ and $\alpha(v'^2)$ are equal 1 for Special Relativity. The obtained Doppler formula is similar to the Doppler formula of Special Relativity. The difference consists in the factor $\alpha(v^2)/\alpha(v'^2)$. All other parameters are dropping out and $\alpha(v^2)/\alpha(v'^2)$ is independent to the direction

of $\vec{v}$ and $\vec{v'}$ and the kind of clock synchronization. In the experiment, two light beams with frequencies ν_a for the counter-propagating beam and ν_p for the co-propagating beam interact with lithium ions having a transition frequency in their rest frame of ν_0

$$\nu_a = \nu_0 \frac{\alpha(v^2)}{\alpha(v'^2)} \cdot \frac{1-\beta_{SR}}{\sqrt{1-\beta_{SR}^2}} \tag{2.33}$$

$$\nu_p = \nu_0 \frac{\alpha(v^2)}{\alpha(v'^2)} \cdot \frac{1+\beta_{SR}}{\sqrt{1-\beta_{SR}^2}} \tag{2.34}$$

$$\Rightarrow \nu_a \nu_p = \left(\frac{\alpha(v^2)}{\alpha(v'^2)}\right)^2 \nu_0^2. \tag{2.35}$$

This experiment is therefore sensitive to a possible deviation from special relativity that is expressed by the factor

$$\frac{\alpha(v^2)}{\alpha(v'^2)} = \frac{1+\hat{\alpha}v^2+\alpha_2 v^4+\ldots}{1+\hat{\alpha}v'^2+\alpha_2 v'^4+\ldots} \tag{2.36}$$

$$\approx 1+\hat{\alpha}(v^2-v'^2)+\ldots. \tag{2.37}$$

The velocity v' of the laboratory frame with respect to the preferred frame can amounts to 350 km/s, if the frame in which the cosmic background radiation is isotropic is chosen as ether frame. Because the velocity v of the ions with respect to the preferred frame can not be measured directly, but the velocity $\vec{\beta}$ relative to the laboratory frame, $(v^2-v'^2)$ and $\vec{\beta}$ can be expressed in a first order approximation by its special relativistic limit

$$(v^2-v'^2)_{SR} = 1-v'^2-\frac{(1-v'^2)(1-\beta^2)}{(1+\vec{v'}\vec{\beta})^2} \tag{2.38}$$

$$\approx \beta^2+2\vec{v'}\vec{\beta}. \tag{2.39}$$

Combining now eqs. 2.35, 2.37 and 2.39 the result is

$$\nu_a\nu_p = \nu_0^2(1+2\hat{\alpha}(\beta^2+2\vec{v'}\vec{\beta})+\ldots). \tag{2.40}$$

Because $\beta \gg v'$ in the present experiments it can be reduced to

$$\nu_a\nu_p = \nu_0^2(1+2\hat{\alpha}\beta^2). \tag{2.41}$$

To determined $\hat{\alpha}$ and ν_0 independent by two measurements at two different velocities β_1 and β_2 are performed

$$\nu_{01}^2 = \nu_{a1}\nu_{p1} = \nu_0^2(1+2\hat{\alpha}\beta_1^2) \tag{2.42}$$

$$\nu_{02}^2 = \nu_{a2}\nu_{p2} = \nu_0^2(1+2\hat{\alpha}\beta_2^2). \tag{2.43}$$

which leads to

$$\hat{\alpha} = \frac{1-\frac{\nu_{01}^2}{\nu_{02}^2}}{2\left(\frac{\nu_{01}^2}{\nu_{02}^2}\beta_2^2-\beta_1^2\right)} \tag{2.44}$$

$$\nu_0^2 = \frac{\nu_{02}^2-\frac{\beta_2^2}{\beta_1^2}\nu_{01}^2}{1-\frac{\beta_2^2}{\beta_1^2}}$$

$$\Rightarrow \nu_0 = \sqrt{\frac{\nu_{02}^2-\frac{\beta_2^2}{\beta_1^2}\nu_{01}^2}{1-\frac{\beta_2^2}{\beta_1^2}}}. \tag{2.45}$$

In the present experiment the velocities are chosen to be $\beta_1 = 0.03$ and $\beta_2 = 0.064$. The sensitivity on $\hat{\alpha}$ is reduced compared to a second measurement at $\beta_0 = 0$ instead of β_1, because $(\beta_2^2 - \beta_1^2)/\beta_2^2 = 0.78$ instead of 1.

2.4 Experiments sensitive to $\hat{\alpha}$

Several different types of experiments are used to measure a deviation of $\hat{\alpha}$ from zero. A list of time dilation experiments can be found in [Mac86] or [Zha97], like measurements of particle lifetimes (like muon [BBC+77]) at high β, satellite based experiments (e. g. [WP97]) or experiments performed on rotating stages using the Mößbauer effect [CIK63]. A detailed discussion in the RMS formalism of some experiments is given in [Wil92a], where it is also shown that the measured quantities are independent of the method of clock synchronization. A detailed discussion of the various measurements of $\hat{\alpha}$ can also be found in [Gwi05].

2.4.1 The original Ives-Stilwell experiment

In 1938 H. E. Ives and G. R. Stilwell [IS38] performed the first measurement of the relativistic Doppler effect at $\beta = 0.005$. They measured the wavelength of the Hβ emission generated by hydrogen canal rays in and against the direction of motion of the hydrogen with a spectrograph. The observed wavelength in the direction of motion is in Special Relativity $\lambda_+ = \lambda\gamma(1+\beta)$ and against the direction of motion it is $\lambda_- = \lambda\gamma(1-\beta)$ (λ is the wavelength at rest). The mean value of the two measured wavelength gives the contribution of time dilation

$$\lambda_m = \frac{\lambda_+ + \lambda_-}{2} = \gamma\lambda. \tag{2.46}$$

In the RMS formalism the sensitivity to $\hat{\alpha}$ is [MS77c]

$$\frac{\lambda_m - \lambda_{mo}}{\lambda_m} = -\hat{\alpha}\beta^2. \tag{2.47}$$

λ_{mo} is the measured mean value. The accuracy of the original Ives Stilwell experiment limits $\hat{\alpha}$ to

$$|\hat{\alpha}| \leq 10^{-2}. \tag{2.48}$$

2.4.2 Hydrogen beam $\beta = 0.84$

An experiment of D. W. MacArthur et al. [MBC+86] using a hydrogen beam with a β of 0.84 is one of the few really high β experiment. With the fourth harmonic of a Nd:YAG laser ($E_0 = 4.66$ eV) the fast hydrogen beam is excited from the ground state $1s$ to np by using the Doppler effect. To vary the energy E of the laser in the rest frame of the hydrogen, the angle ϕ between the hydrogen beam and laser beam is changed, i. e.

$$E = \frac{E_0}{g_0}\gamma(1 + \beta\cos\phi). \tag{2.49}$$

where g_0 is the parameter introduced by Robertson and is equal to one for Special Relativity. The disadvantage of this parameter is, that it is velocity dependent. The relation of g_0 to the parameter $\hat{\alpha}$ is $1/(\gamma g_0) = a \approx 1 + (\hat{\alpha} - 1/2)\beta^2 + \ldots$. An upper value for $|\hat{\alpha}| < \Delta g_0/(\gamma\beta^2)$ is

$$|\hat{\alpha}| < 2.0 \cdot 10^{-4}. \tag{2.50}$$

2.4.3 Two photon absorption experiment on neon

Several experiments were carried out on a neon beam with counter-propagating laser beams of equal frequency ν_L to cancel out the first order Doppler effect. The original experiment in 1985 from Kaivola et al. [KPR85] uses a three level cascade in neon and compares the frequency of the two photon transition from the level g to f with an off-resonant intermediate state with a fast neon beam of $\beta = 0.0036$, where the laser is in resonance with the transition from g to i (frequency ν_1) when co-propagating and with i to f (frequency ν_2) when counter-propagating to the neon beam. The experiment is discussed within the RMS test theory in [Wil92a]

$$\nu_L = \sqrt{\nu_1\nu_2}(1 + \hat{\alpha}\beta^2 + 2\hat{\alpha}\vec{\beta}\vec{v'} + \ldots). \tag{2.51}$$

The non sidereal term $\hat{\alpha}\beta^2$ was investigated in [KPR85] and gave an upper limit of $4{\cdot}10^{-5}$ on $|\hat{\alpha}|$. In 1988 also the sidereal part $2\hat{\alpha}\vec{\beta}\vec{v'}$ was investigated by Riis et al. [RABP88] and resulted an upper limit of $|\hat{\alpha}| < 1.4 \cdot 10^{-6}$. In 1992 McGowan et al. [MGSL93] improved the limit to $|\hat{\alpha}| < 2.3 \cdot 10^{-6}$ via the non sidereal term by remeasuring some frequencies.

2.4.4 Previous time dilation experiments carried out at the TSR

The first experiment carried out at the TSR was done by Klein in 1991 [Kle91] on a $^7Li^+$ ion-beam at $\beta = 0.064$. Instead of the two level system in $^7Li^+$ used in the present

thesis a closed three level system with a common upper level and two different ground levels was employed (Λ-system), but the measurement principle was the same as in the present work. In the RMS theory the experiment is sensitive to $\hat{\alpha}$ by

$$\frac{\nu_a \nu_p}{\nu_1 \nu_2} = 1 + 2\hat{\alpha}\beta^2 + \dots . \tag{2.52}$$

ν_a and ν_p are the laser frequencies antiparallel and parallel to the ion beam. ν_1 and ν_2 are the transition frequencies between the two ground states to the upper state. An upper limit of $1.5 \cdot 10^{-5}$ for $|\hat{\alpha}|$ was obtained. In 1994 this was improved by Grieser et al. [GBD+94] to $|\hat{\alpha}| < 8 \cdot 10^{-7}$.

In 2003, Saathoff et al. [SKE+03] obtained a new upper limit of $|\hat{\alpha}| < 2.2 \cdot 10^{-7}$ using instead of the Λ-system the same two level system as in the present thesis. This is the presently most precise verification of the relativistic time dilation factor.

It is important to mention that it is desirable to make measurements at different velocities, because from a combination of a low velocity experiment with a high velocity experiment that is more sensitive to higher orders effect, $\hat{\alpha}_2$ can be determined with a higher accuracy. As it is shown in [Gwi05] the combination of the best value of $|\hat{\alpha}| < 2.2 \cdot 10^{-7}$ obtained at the TSR [SKE+03] with the work of MacArthur et al. at $\beta = 0.84$ [Mac86] a limit on $|\hat{\alpha}_2| < 2.8 \cdot 10^{-4}$ can be given (s. equation 2.17).

2.5 Standard Model Extension

The so-called Standard Model Extension (SME) was formulated by V. A. Kostelecký and coworkers [CK97][CK98][KM02] and is a dynamical test theory. The Lagrangian includes all parameterized Lorentz- and CPT-violating terms that can be formed with known fields. The analysis of the Ives-Stilwell experiment in the photon sector (electromagnetic field) is given by M. E. Tobar et al. [TWFH05]. They start from modified Maxwell equations without source

$$\nabla \vec{D} = 0 \tag{2.53}$$

$$\nabla \vec{B} = 0 \tag{2.54}$$

$$\nabla \times \vec{E} + \partial_t \vec{B} = 0 \tag{2.55}$$

$$\nabla \times \vec{H} - \partial_t \vec{D} = 0 \tag{2.56}$$

$$\begin{pmatrix} \vec{D} \\ \vec{H} \end{pmatrix} = \begin{pmatrix} \epsilon_0(\tilde{\epsilon}_r + \kappa_{DE}) & \sqrt{\epsilon_0/\mu_0}\kappa_{DB} \\ \sqrt{\epsilon_0/\mu_0}\kappa_{HE} & \mu_0^{-1}(\tilde{\mu}_r^{-1} + \kappa_{HB}) \end{pmatrix} \begin{pmatrix} \vec{E} \\ \vec{B} \end{pmatrix}. \tag{2.57}$$

The difference between the normal Maxwell equations and the modified Maxwell equation is the relationship between $\vec{E}$, $\vec{B}$, $\vec{D}$ and $\vec{H}$. The additional tensors κ_{DE}, κ_{DB}, κ_{HE} and κ_{HB} are 3×3 matrices and vanish for the standard Maxwell equation. The number of independent coefficients contained in all tensors κ_{xx} is 19. After some calculation[3] (s.

[3] One assumption in the calculation is that Lorentz transformation is still valid for matter. Also $\tilde{\epsilon}_r$ and $\tilde{\mu}_r$ are identity matrices, because only the vacuum case is investigated.

[TWFH05]) the relation

$$\frac{\nu_a \nu_p}{\nu_0^2} = 1 + 4\tilde{\kappa}_{tr}\beta T \tag{2.58}$$

is obtained. $\tilde{\kappa}_{tr}$ is the trace of the tensor κ_{DE} divided by 1/3. T is a factor, that is introduced by the transformation from the earth bound laboratory system to a non-rotating sun-centered frame, which is the standard reference frame in this test theory. Compared to other experiments, like the Michelson-Morley- or Kennedy-Thorndike-experiments (s. [KM02]), the experiment is only sensitive to one scalar parameter, like in the RMS but it scales linear with β. Taking the results from Saathoff et al. [SKE+03], a limit of 10^{-4} to 10^{-5} on $\tilde{\kappa}_{tr}$ is obtained. A non-zero result would indicates that the phase velocity of the counter-propagating laser beams are not equal anymore.

In the work of Charles D. Lane [Lan05] the experiment is analyzed in the fermion sector of the SME. The experiment is sensitive to various combinations of Lorentz violating parameters that are related to the proton and electron (details are given in the paper). The relation between the frequency measured over the product of the two laser frequencies $\nu_a\nu_p = \bar{\nu}_{beam}^2$ and the frequency ν_{lab} measured in the rest frame of the ions is changed to

$$\frac{\bar{\nu}_{beam}^2}{\nu_{lab}^2} \approx 1 - \frac{1}{3\pi\nu_{SM}} \sum_{w=p,e} \gamma_w \left[\frac{1}{6}\beta^2 \tilde{c}_Q^w + \beta^2\beta_s \left(\frac{3}{2}\tilde{c}_{TX}^w - \frac{3}{2}\tilde{c}_{TY}^w - \tilde{c}_{TZ}^w \right) \right] \tag{2.59}$$

$$\tilde{c}_Q^w = m^w(c_{XX}^w + c_{YY}^w - 2c_{ZZ}^w) \tag{2.60}$$

$$\tilde{c}_{TJ}^w = m^w(c_{TJ}^w + c_{JT}^w) \text{ with } (J = X, Y, Z). \tag{2.61}$$

w is p for a proton and e for an electron. γ_w is $-1/15 \times 10^{-2}$ for the proton and $-1/15 \times 10^{-5}$ for the electron. ν_{SM} is the transition frequency obtained by the standard model. β is the velocity of the ions in the lab frame. β_s is the mean orbital velocity of the earth around the sun. m^w is the mass of the corresponding particle. The following limits are derivated from the results given in [SKE+03]

$$|c_{XX}^p + c_{YY}^p - 2c_{ZZ}^p| \lesssim 10^{-11}, \tag{2.62}$$

$$|c_{TJ}^p + c_{JT}^p| \lesssim 10^{-8} \ (J = X, Y, Z), \tag{2.63}$$

$$|c_{XX}^e + c_{YY}^e - 2c_{ZZ}^e| \lesssim 10^{-5} \tag{2.64}$$

$$\text{and } |c_{TJ}^e + c_{JT}^e| \lesssim 10^{-2} \ (J = X, Y, Z). \tag{2.65}$$

Chapter 3

Lithium ion

To ensure high sensitivity of the Ives-Stilwell type experiment on $\hat{\alpha}$ high velocities are favorable. Therefore charged particles i. e. ions are used, that can be easily accelerated by electric fields. For a Doppler-free saturation spectroscopy on fast ions some boundaries arise from practical issues. The transition frequency should lay in the optical region, which can be easily reached by lasers, and should have a small linewidth for good determination of the line center. Moreover the ion should have a high q/m ratio to reach a high velocity in the TSR with its finite rigidity. Possible candidates are listed in the following table.

	$^6Li^+$	$^7Li^+$	$^9Be^+$	$^{24}Mg^+$
lower level	$2s^3S_1$ (F = 2)	$2s^3S_1$ $\left(F = \frac{5}{2}\right)$	$2s^2S_{1/2}$ (F = 2)	$3s^2S_{1/2}$
upper level	$2p^3P_2$ (F = 3)	$2p^3P_2$ $\left(F = \frac{7}{2}\right)$	$2p^2P_{1/2}$ (F = 1)	$3p^2S_{1/2}$
transition wavelength [nm]	548.5	548.5	313	280
lifetime lower level [s]	50	50	∞	∞
lifetime upper level [ns]	43	43	8.7	3.7
maximal β@TSR	0.075	0.064	0.050	0.019

Of these ions, the helium-like lithium ion in the metastable triplet state are best suited for a time dilation experiment. For the experiment the $^7Li^+$ is used because of the large hyperfine-structure splitting, which is much larger than the Doppler width of the stored ion beam as it will be shown later, while the hyperfine-structure splitting of $^6Li^+$ is comparable to the Doppler width, and it was also used in all TSR based time dilation experiments before. The level scheme of $^7Li^+$ (s. figure 3.1) allows two kinds of spectroscopy by using the closed two-level system F=5/2→F=7/2 and the Λ-system F=5/2→F=5/2, F=3/2→F=5/2. The transition frequencies and level splittings are well measured as the lithium ion is a helium-like system which is of great theoretical interest. The relevant frequencies are given in table 3.1.

The natural linewidth is 3.7 MHz[1], which results from the lifetime of the upper state of 43 ns. The lifetime of the lower level is 50 s [Sag99] in vacuum but, due to interaction with rest gas and electrons of the electron cooler, this value goes down to

[1]All linewidth are defined as full-width at half-maximum (FWHM).

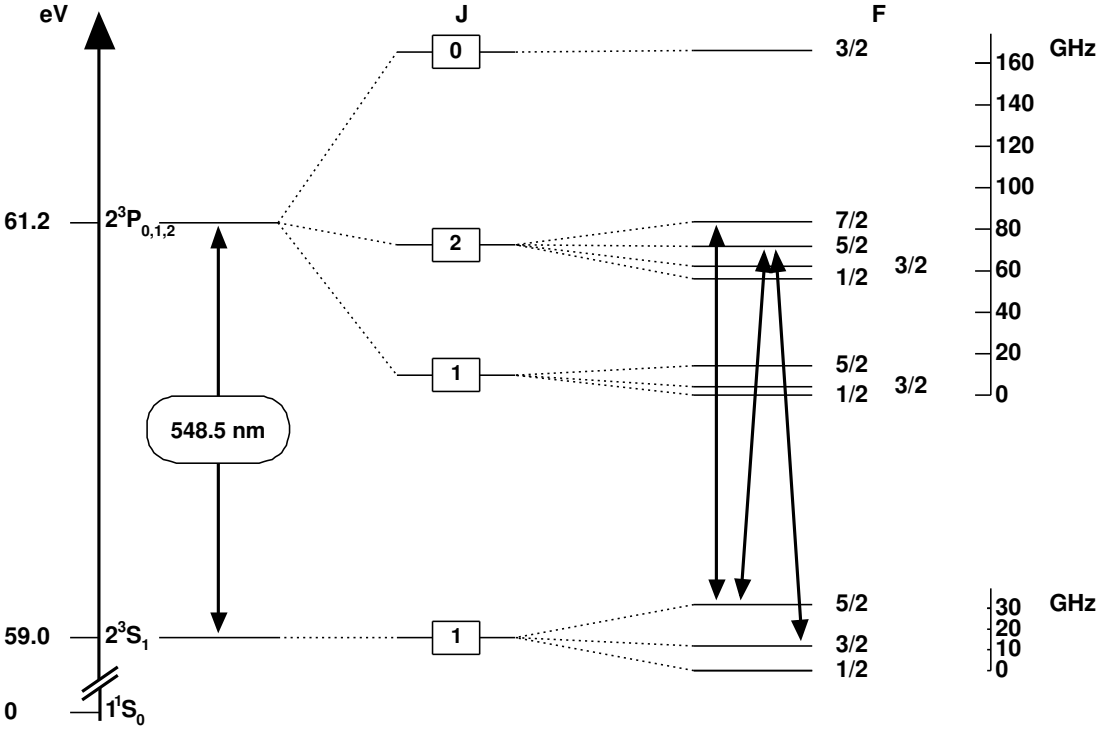

Figure 3.1: Energy level diagram of $^7Li^+$

transition	frequency [MHz]	reference
$2^3S_1(F=5/2) \rightarrow 2^3P_2(F=7/2)$	546 466 918.79(40)	Riis 1994 [RSP$^+$94]
$2^3S_1(F=3/2) \rightarrow 2^3S_1(F=5/2)$	19 817.673(13)	Kowalski 1983 [KNN$^+$83]
	19 817.90(24)	Clarke 2003 [CW03]
theory	*19 817.680(25)*	*Riis 1994 [RSP$^+$94]*
$2^3P_2(F=5/2) \rightarrow 2^3P_2(F=7/2)$	11 775.8(2)	Kowalski 1983 [KNN$^+$83]
	11 774.04(31)	Clarke 2003 [CW03]
theory	*11 773.05(18)*	*Riis 1994 [RSP$^+$94]*

Table 3.1: Frequencies that a relevant for the experiment (one sigma uncertainty).

20 s for ions stored in the TSR, but nevertheless is long enough to prepare the ion beam by electron cooling and to perform experiments. The saturation intensity of the transition is 6.7 mW/cm^2[WGG$^+$98]. The measurements of the absolute frequency of the $2^3S_1(F = 5/2) \rightarrow 2^3P_2(F = 7/2)$ transition given in [RGK$^+$98], which is 2 MHz lower than [RSP$^+$94], is disregarded for reasons explained in [SKE$^+$03].

Because the storage ring uses magnetic fields for the manipulation of the ions, also the magnetic properties of the lithium ion and the influence of the magnetic fields on the energy levels of the ion (Zeeman effect) are of interests. The following discussion is limited to low magnetic fields, which means the coupling to the magnetic field is assumed to be weak compared to the hyperfine interaction.

In this case the interaction between the magnetic moment $\vec{\mu}_F$ of the ion with an external magnetic field $\vec{B}$

$$V = -\vec{\mu}_F \vec{B} \tag{3.1}$$

leads to level shifts (s. [MK97]), which depends on the magnetic quantum number $m_F = -F, -F+1, \ldots, F$

$$\Delta E_B^{HFS} = g_F \mu_B B m_F \tag{3.2}$$

$$g_F = g_J \frac{F(F+1) + J(J+1) - I(I+1)}{2F(F+1)} - \left(g_K \frac{\mu_K}{\mu_B} \frac{F(F+1) + I(I+1) - J(J+1)}{2F(F+1)} \right) \tag{3.3}$$

$$g_J = 1 + \frac{J(J+1) + S(S+1) - L(L+1)}{2J(J+1)} \tag{3.4}$$

$$\mu_B = \text{Bohrsches magneton} \approx 1.4 \frac{\text{MHz}}{\text{Gauss}}. \tag{3.5}$$

The second term of g_F is neglected, because $\mu_K/\mu_B \approx 1/2000$. The g_F values for the two levels of interest in the present investigation are

$$\begin{aligned} \text{Ground level: } g_{\frac{5}{2}} &= 0.800 \\ \text{Upper level: } g_{\frac{7}{2}} &= 0.857. \end{aligned}$$

Now it is possible to calculate the frequency shift for the different optical allowed transitions with $\Delta m_F = m_{Fg} - m_{Fu}$ (m_{Fg} for the ground level and m_{Fu} for the upper level) (s. table 3.2). In an external magnetic field also the absorption and emission properties are modified. Looking in the direction of the magnetic field only circularly polarized light can be observed in emission (short overview of the polarization of light is given in appendix A). Transversal to the magnetic field circularly as well linearly polarized light is observable. If $\Delta m_F = -1$, then the emitted light is right circularly polarized, if $\Delta m_F = +1$, then the emitted light is left circularly polarized, and for $\Delta m_F = 0$ the light is linearly polarized. This is also true for the absorption of photons. If at the beginning the population of the single Zeeman levels are equal, this is changed by the interaction with the light beam, because the probability of spontaneous emission of left-, right- or

m_{Fg}	$\Delta m_F = +1$ [MHz/Gauss]	$\Delta m_F = 0$ [MHz/Gauss]	$\Delta m_F = -1$ [MHz/Gauss]
-5/2	-1.4	-0.2	1
-3/2	-1.32	-0.12	1.08
-1/2	-1.24	-0.04	1.16
1/2	-1.16	0.04	1.24
3/2	-1.08	0.12	1.32
5/2	-1	0.2	1.4

Table 3.2: Shift of the transition frequency normalized to one Gauss

linear polarized photon is not equal. The relative line strength are given by the square of the Clebsch-Gordon-coefficients. The relevant values are shown in figure 3.2. As it can be seen the line strengths decreasing the absolute value of the quantum number m_{Fg} of the ground state are preferred.

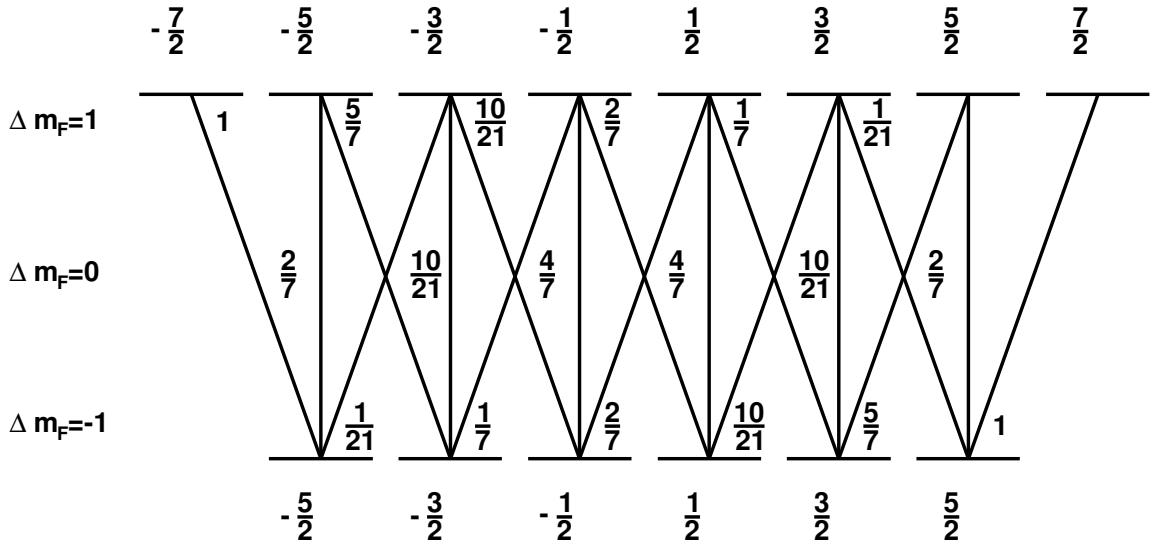

Figure 3.2: Relative line strengths for transitions between the Zeeman levels. The sum of the line strengths for transitions having the same upper state are normalized to one.

Chapter 4

Test Storage Ring

For precision spectroscopy with high accuracy and sensitivity to the time dilation factor an ion beam with good beam properties, stability and high velocity is required. The accelerators and the storage ring TSR of the Max Planck Institute for Nuclear Physics fulfill these requirements [HBB+89].

4.1 Generating and accelerating of the ions

Negatively charged $^7Li^-$ ions are produced in a metal ionized sputtering source and accelerated towards the positively charged terminal[1] of the Tandem van-de-Graaff accelerator. In this terminal a gas cell with nitrogen is placed. Electrons of the negative ions are stripped of by collisions with the gas and the ions are getting positively charged. The ions are further accelerated by the positively charged terminal to a final energy of $E = (q+1)U$, where U is the terminal voltage and q is the charged state of the stripped ion. For the single charged positive $^7Li^+$ ions used in the present experiment, the final energies are 13.3 MeV, corresponding to an ion velocity of 6.4% and 2.9 MeV for an ion velocity of 3% speed of light.

The electron stripping and recapturing processes in the terminal play are important role, because they result in a relative population of the metastable ground level of about 10%.

4.2 Test Storage Ring (TSR)

The Heidelberger Test Storage Ring consists of eight 45° dipole magnets and twenty quadrupole magnets for beam focusing. Two dipole and five quadrupole magnets form one corner of the ring, which has a square like shape. This corners are connected by straight lines that delivers the space for experimental sections and tools for operation. The total circumference is 55.4 m. In figure 4.1 an overview of the TSR is presented. The maximum possible ion velocity v is given by the maximum magnetic field B, the bending radius $\rho = 1.15$ m of the dipoles, and the mass m and charged state q of the

[1] The terminal voltage can be set up to a value of 12 MV.

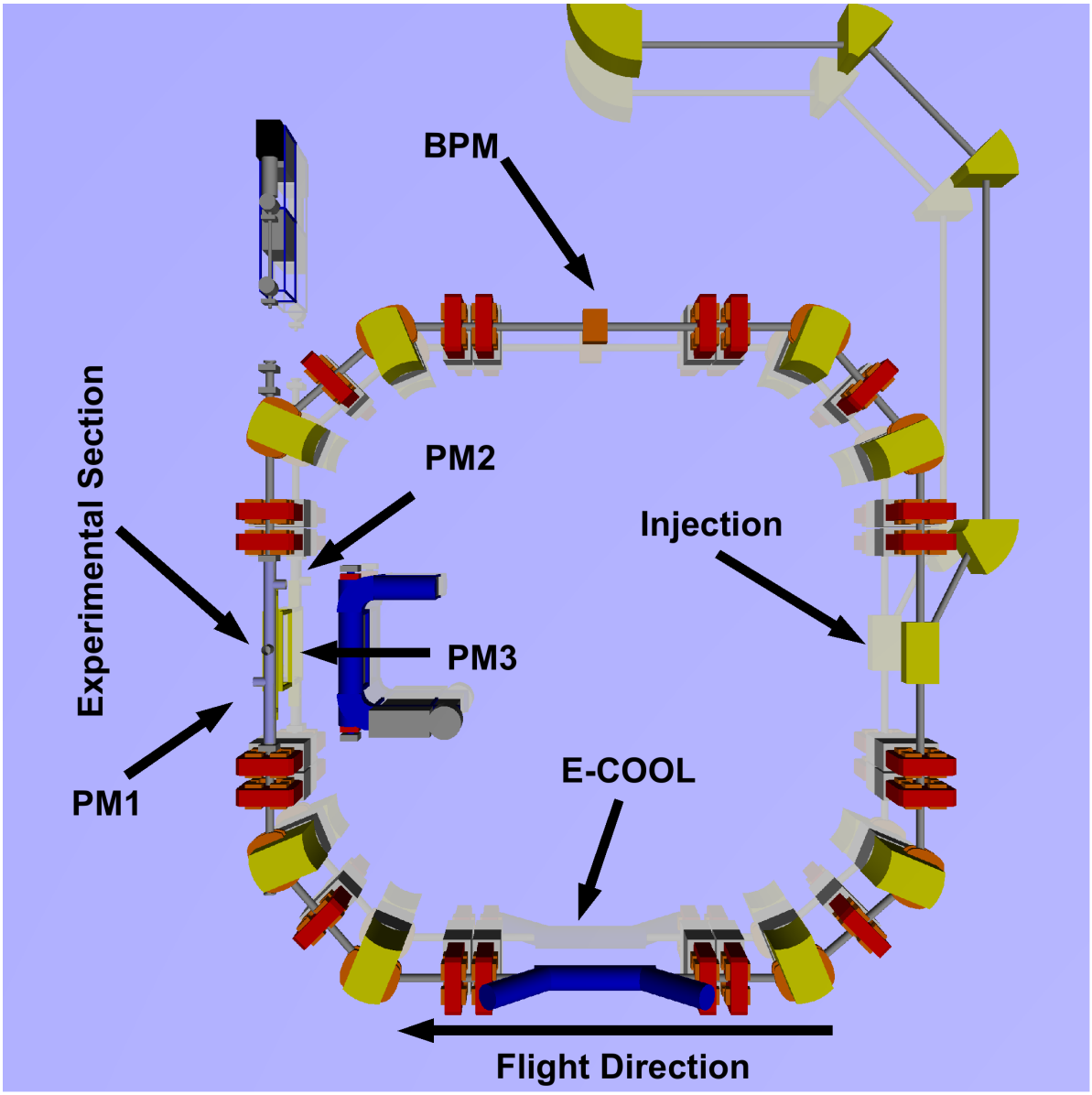

Figure 4.1: Overview of the TSR with the twenty quadrupole and eight dipole magnets. After the section of the injection comes the section of the electron cooler (E-COOL) followed by the experimental section. The last section contains the beam profile monitor (BPM). Also shown is the electron-target [SLO$^+$04] (within the ring) that is moved out of the ring during the time dilation measurements. The extended beam line in extension of the experimental section, which is used for molecular fragment detection in connection with the electron-target, is also disconnected from the ring during the measurements. The positions of the three photomultipliers PM1, PM2 and PM3 are indicated.

ion. The Lorentz force must be equal to the centripetal force

$$qBv = \frac{mv^2}{\rho} \tag{4.1}$$

$$\Rightarrow B\rho = \frac{mv}{q}. \tag{4.2}$$

The product $B\rho$ is the magnetic rigidity that has a maximum value of 1.4 Tm for the TSR dipoles, which corresponds to a velocity of $\beta = 0.064$ for a $^7Li^+$ ion. The vacuum in the TSR is in the range of $5 \cdot 10^{-11}$ mbar and leads to a $^7Li^+$-ion beam lifetime of 30 to 60 seconds.

4.2.1 Ion movement

First only the motion of a single ion in a magnetic structure is discussed (details in [Wil92b]). Only the transversal motion of the ion is described, because only magnetic fields transversal to the direction of motion are respected. The equation of motion in such a magnetic structure is described by

$$x''(s) - k(s)x(s) = 0. \tag{4.3}$$

$x(s)$ is the transversal displacement depending on the position s along the beamline. $x''(s)$ is d^2x/ds^2. The function $k(s)$ describes the focusing of the quadrupole magnets. The solution of 4.3

$$x(s) = \sqrt{\epsilon}\sqrt{\beta(s)}\cos[\Psi(s) + \phi] \tag{4.4}$$

shows that the ions perform so-called betatron oscillations around the sollbahn. $\Psi(s)$ and ϕ are phases which are not important for the further discussion. ϵ denotes the emittance, which plays a central role as shown later together with the beta-function $\beta(s)$ the beam diameter and beam divergence can be calculated at every point of the ring. $x(s)$ and $x'(s)$ define a phase ellipse with an area F equal to $\epsilon\pi$. After Liouvilles law the area of this ellipse i. e. ϵ is constant if only conservative forces are used. The amplitude $x_0(s)$ of the oscillation is

$$x_0(s) = \sqrt{\epsilon\beta(s)}. \tag{4.5}$$

If now many ions with a momentum spread Δp are analyzed, the ion beam radius x_s can be measured at one position. With this radius and the known beta-function the emittance $\epsilon = x_s^2/\beta(s)$ of the ensemble can be determined. And with the known emittance and beta-function the beam radius at all ring positions can be calculated.

The maximum beam divergence can be calculated as the maximum of the first derivative. The result of this calculation is

$$x'_{max}(s) = \sqrt{\epsilon}\sqrt{\frac{1 + \frac{\beta'(s)^2}{4}}{\beta(s)}}. \tag{4.6}$$

As mentioned before the emittance can be calculated, if the beam radius and beta-function at one position is known. The beta-function for the setting of the TSR used in the present experiments is illustrated in 4.2. The beam radius of the ion beam however must be measured. For this the so-called beam profile monitor (BPM) at the TSR is used, which is described in the following section.

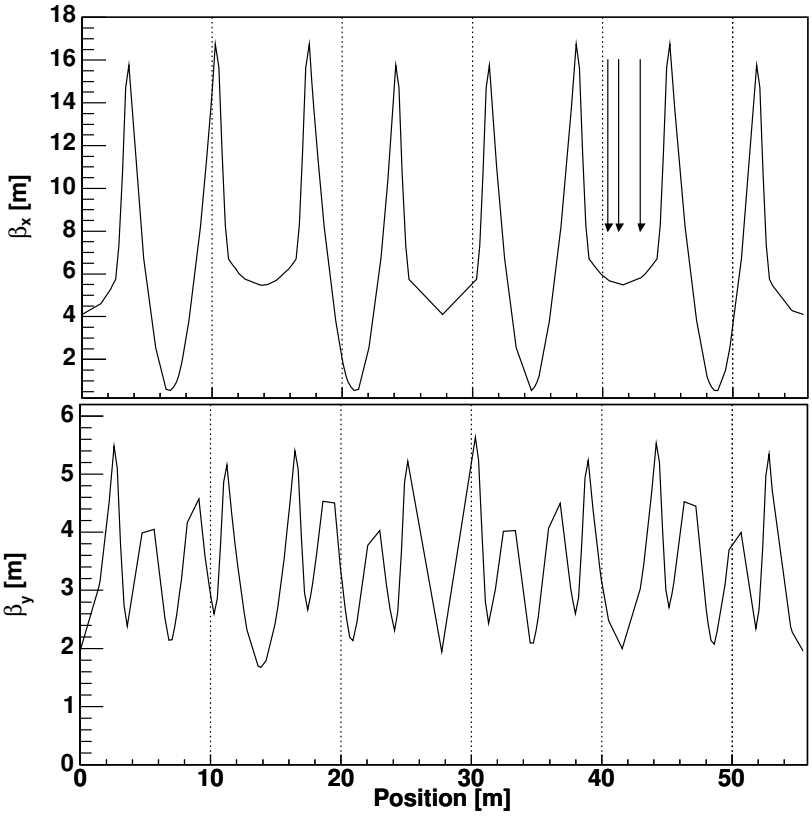

Figure 4.2: beta-function of the TSR. The arrows indicate the positions of the photomultipliers in the experimental section used for the fluorescence detection in the lithium ion spectroscopy (from left to right: PM1, PM3, PM2).

4.2.2 Beam diagnostics

Beam Profile Monitor For measuring the ion beam diameter the beam profile monitor (BPM) is used. The working principle is to detect the ionization of the rest gas by the ion beam. This process is proportional to the ion density. If the number of ionizations depending on spatial position is measured, the profile of the ion beam can be determined. The sum of the ionizations is proportional to the total number of ions.

Perpendicularly to the ion beam, an electric field is applied. The ions and electrons created from the rest gas by the ion beam are accelerated by the electric field. The ions are detected by a detector with spatial resolution, here a micro-channel plate is used. The electrons are not used for the measurements (compare figure 4.3). To measure both

dimensions perpendicular to the beam, one BPM for each dimension is installed at the TSR.

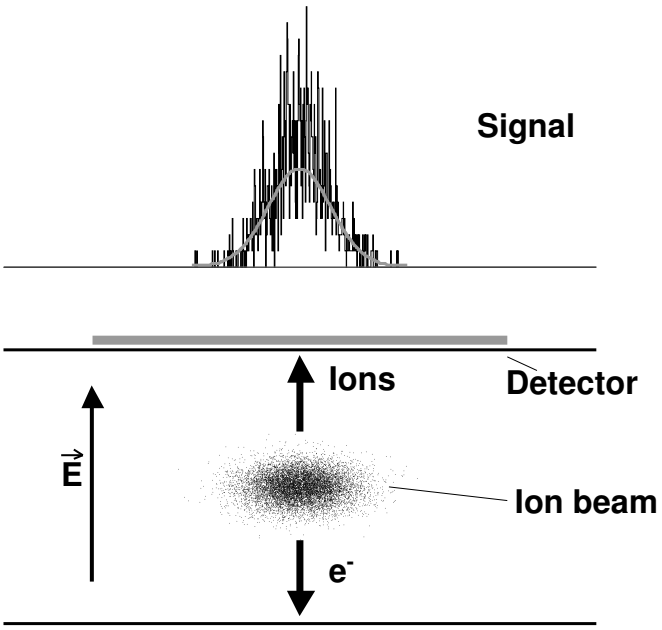

Figure 4.3: Schematic setup of a BPM. The width of the ion beam is determined by a Gaussian fit to the measured signal.

The spatial resolution of the BPM is $\sigma_{resx} = 200\ \mu m$ for the horizontal and $\sigma_{resy} = 300\ \mu$m for the vertical detection [Beu00]. The ion beam diameter x_s can be measured now at the BPM. With this information and the beta-function the emittance can be calculated with $\epsilon = x_s^2/\beta(s)$. Now the beam diameter (with 4.5) and the beam divergence (with 4.6) can be calculated for every position of the ring. With this information the influence of the ion beam properties to the lithium ion spectroscopy can be determined.

Schottky analysis To determinate the revolution frequency of the ions in the ring a Schottky analysis is used [Bou85]. The ions induce a noise signal in a capacitive pickup, which is installed in the TSR. An ion with the revolution frequency ν_r produces a line spectrum with one discrete line at each harmonic of ν_r in a Fourier expansion of the noise signal. For an ensemble of ions with the momentum p and the momentum spread Δp the lines in the spectrum have a width of

$$\Delta\nu_r \quad = \quad h\nu_r\eta\frac{\Delta p}{p}. \tag{4.7}$$

Here h is the harmonic of the revolution frequency and $\eta = 0.895$ is the slip factor of the TSR.

The momentum spread of the ion beam can be also measured with a laser, which is tuned over the velocity distribution, because frequency and velocity are connected over

the Doppler effect. In the case where $\gamma \approx 1$ (for $\beta = 0.064 \Rightarrow \gamma = 1.002$) the momentum spread can be given as frequency width $\Delta\nu_a$ measured with the antiparallel laser beam that has the frequency ν_a[Saa02]

$$\frac{\Delta p}{p} = \frac{1-\beta}{\beta}\frac{\Delta\nu_a}{\nu_a}. \tag{4.8}$$

4.2.3 Electron cooling

When the ions are injected into the TSR, the ion beam diameter is 18 mm and the beam divergence is about 2 mrad which would severely limit the frequency accuracy of the laser spectroscopy. To reduce the diameter and divergence the betatron-oscillations must be damped. This can be done using the electron cooler.

The electron cooler produces an electron beam with a small velocity distribution (or temperature) at a velocity equal to the desired ion velocity. The electrons are created by a heated cathode at a temperature of about $1100°C (\approx 140$ meV). They are guided by a strong magnetic field and accelerated by an electric field. Due to the magnetic field the transversal and the longitudinal degree of freedom are decoupled. At the beginning the electrons have the temperature of the cathode but due to the acceleration the longitudinal velocity spread goes down to 0.1 meV. The temperature of the transversal component is reduced by an adiabatic expansion of the electron beam. This is done by lowering the magnetic guiding field from high field strength B_h at the cathode to low field strength B_l. The ratio is the expansion factor, typically $B_h/B_l = 9$, is also the factor of the temperature reduction. For the transversal velocity distribution a width of 16 meV is thus obtained. These cooled electrons and the ion beam are overlapped over a distance of 1.2 m, where they interact via the Coulomb force. An extended description of electron cooling can be found in [Pot90]. The shape of cooling force F_{cooler} in the longitudinal as well as in the two transversal degrees of freedom can be approximately described as a function of the velocity mismatch $\Delta v = v_i - v_0$ by

$$F_{cooler}(\Delta v) = 3F_{max}\Delta_{max}^2\frac{\Delta v}{|\Delta v|^3 + 2\Delta_{max}^3}, \tag{4.9}$$

where v_0 is the average velocity of the electrons and v_i the ion velocity in one of the three degrees of freedom. Δ_{max} is the velocity mismatch, where the maximal cooling force F_{max} is reached. To obtain the ring-averaged force F_{cooler} must be multiplied by the ratio of the cooler length (1.2 m) with the ring circumference ($C_0 = 55.4$ m), which is equal to 0.022.

For the ions, that do not match the electron velocity, the electrons look like a moving wall of negative charge, so that an ion that is to slow will be accelerated by the wall to the velocity of the electrons. If the ion is to fast, it will be decelerated until it reaches the electron velocity. So the velocity distribution of the ions gets smaller for all three degrees of freedoms. This means the betatron-oscillations are damped and the beam quality is increased up to a value where the beam diameter is of the order of 1 mm and the beam divergence is below 200 μrad as required for the lithium ion spectroscopy (s. figure 4.4). An electron cooled lithium ion beam consist typical of about 10^8 ions

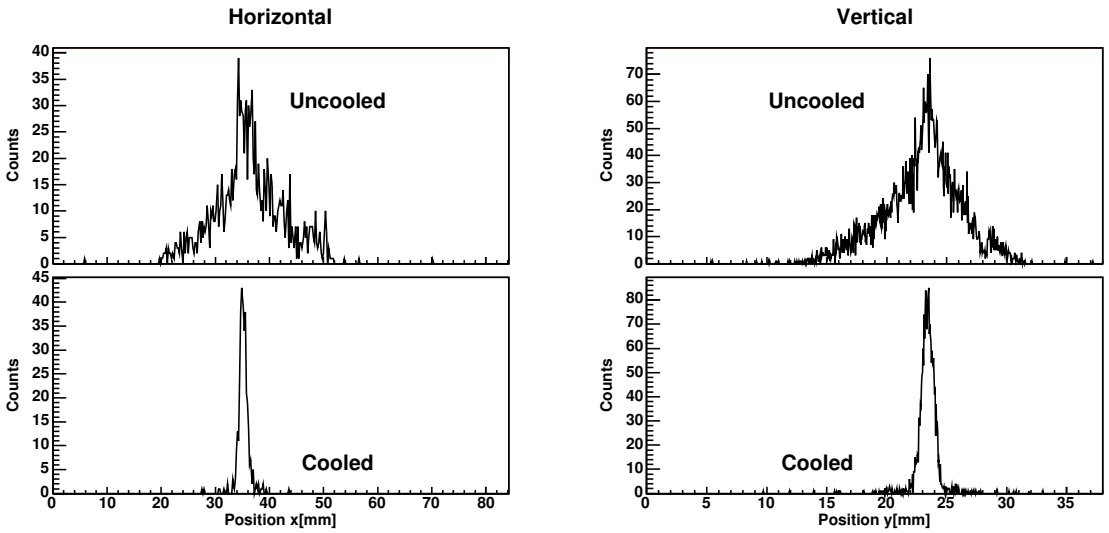

Figure 4.4: The horizontal and vertical beam profile before (upper picture) and after cooling of 19 seconds (lower picture) ($\beta = 0.03$).

whereby 10% are in the $2s^3S_1$ ground state ($\beta = 0.064$)[Saa02]. The momentum spread is in the range of $\Delta p/p = 6.5 \cdot 10^{-5}$ which is equal to a Doppler width of 2.5 GHz for the transition.

4.2.4 Bunching

Because the stability of the electron energy in the electron cooler is not sufficient for the experiment, an additional force is applied. The force is produced by an electric field with a frequency $\nu_{buncher}$, that is a multiple of the revolution frequency of the ions. Using two plates the electric field acts on the ions as it shown in figure 4.5 and, because the plates are on the same potential, no transversal force act on the ion beam. While the

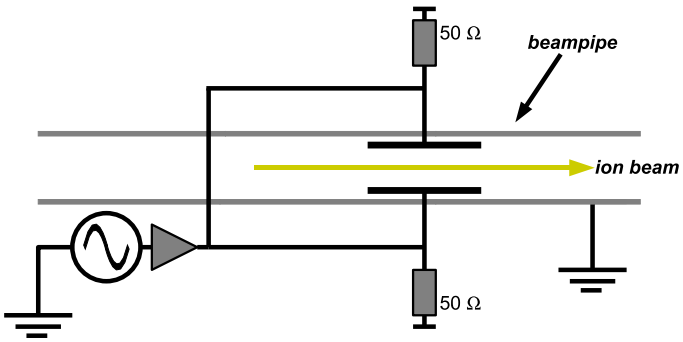

Figure 4.5: Setup of the buncher for energy stabilization of the ion beam. The length L of the plates is approximately 20 cm.

ions fly through the plates the voltage changes by $\Delta U(t) = U(t) - U(t + \Delta t)$. Because

Δt is much smaller than the period of the applied frequency, it is a good approximation to set $\Delta U(t) \approx \dot{U}(t)\Delta t$. The force averaged over one ring circumference C_0 is

$$F_{buncher}(t) = \frac{e}{C_0}\Delta U(t) = \frac{e}{C_0}\dot{U}(t)\Delta t \tag{4.10}$$

$$= \frac{e}{C_0}\dot{U}(t)\frac{L}{v_{ion}}. \tag{4.11}$$

The applied voltage is a cosine, $U(t) = U_0 \cos(2\pi\nu_{buncher}t)$ i. e. $\dot{U}(t)$ is

$$\dot{U}(t) = -2U_0\pi\nu_{buncher}\sin(2\pi\nu_{buncher}t), \tag{4.12}$$

and introducing the phase $\phi = 2\pi\nu_{buncher}t$ we can write

$$\dot{U}(\phi) = -2U_0\pi\nu_{buncher}\sin(\phi). \tag{4.13}$$

To derive the force on an ion, that has a velocity deviation Δv from the mean velocity v_{ion}, we observed that the phase deviation $\Delta\phi$ is connected with Δv by [Eis98]

$$\Delta\phi = 2\pi h\gamma^2\eta\frac{\Delta v}{v_{ion}}, \tag{4.14}$$

where γ is the relativistic dilation factor, $\eta = 0.895$ is the slip factor and h is the harmonic of $\nu_{buncher}$ with respect to the round trip frequency. Setting the reference phase to zero, ϕ is equal $\Delta\phi$. Bringing all together, the force can be given as a function of Δv

$$F_{buncher}(\Delta v) = -\frac{2\pi\nu_{buncher}U_0eL}{C_0v_{ion}}\sin\left(2\pi h\gamma^2\eta\frac{\Delta v}{v_{ion}}\right). \tag{4.15}$$

The spatial structure of a bunched ion beam reflects the harmonic h of the bunching frequency.

Chapter 5

Iodine spectroscopy

The frequencies of the lasers used for the lithium ion spectroscopy must known as precise as possible. This is realized by iodine spectroscopy. All laser frequencies are determined with respect to certain hyperfine transitions in the $^{127}I_2$-molecule, the absolute frequency of which are well known (relative uncertainty 10^{-10}). Iodine is a reliable tool for laser stabilization, because of its rich and strong spectrum in the visible range (500 nm - 650 nm). For more details see appendix B.

5.1 Optical devices

Before the setup for the iodine spectroscopy is explained, two optical devices are discussed, the acousto-optic modulator (AOM) and the electro-optic modulator (EOM).

5.1.1 The Acousto-Optic Modulator (AOM)

Many different kinds of explanation of the acousto-optic effect exist. Here the explanation by phonon-photon scattering is used.

An acousto-optic modulator is a crystal which is excited by an acoustic wave of the frequency ν_{AOM}, i. e. phonons are generated. If a light beam is sent through the crystal, one or more phonons can be absorbed or generated by the light beam (s. figure 5.1(a)). Because of energy and momentum conservation, the light is frequency shifted and deflected by an angle with respect to the incoming beam. The frequency ν_s and wave-vector $\vec{k_s}$ of the deflected beam are connected to those of the incoming beam ν, $\vec{k}$ by

$$\begin{aligned} \nu_s &= \nu \pm n\nu_{AOM} \text{ (n=Number of absorbed/generated phonons)} \\ \vec{k_s} &= \vec{k} + \vec{k}_{AOM} \end{aligned}$$

Because the frequency of a photon (10^{14} Hz) is much higher than that of a phonon (10^8 Hz), it is a good approximation to set $|\vec{k_s}| \approx |\vec{k}|$. From the vector diagrams of the momenta 5.1(b), the angle ϕ between the incident beam and the acoustic wavefront is

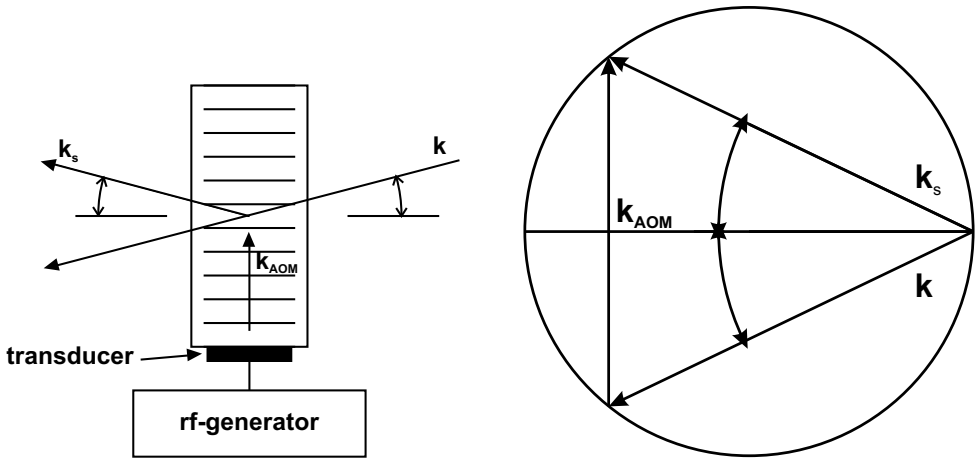

(a) Function of an AOM

(b) Vector diagram of the momenta

Figure 5.1: Principle of the AOM

found to be given by

$$\sin(\phi) = \frac{1}{2}\frac{k_{AOM}}{k}.$$

5.1.2 The Electro-Optic Modulator (EOM)

The electro optic effect describes the linear modification of the refraction index of a crystal by an electric field V. In our case the electric field is applied along an optical axis of the crystal and in the direction of the polarization vector of the laser beam(s. figure 5.2(a)). The change of the refraction index is proportional to the applied field

$$\begin{aligned} \Delta n &= m_c V \\ m_c &= \text{figure of merit} \end{aligned} \tag{5.1}$$

and introduces a corresponding optical phase shift

$$\begin{aligned} \Delta\phi &= \frac{2\pi\nu}{c}\frac{l}{d} m_c V \\ l &= \text{length of the crystal} \\ d &= \text{crystal thickness.} \end{aligned} \tag{5.2}$$

If a sinusoidal signal $V(t) = V_0 \sin(2\pi\Omega t)$ with a modulation frequency Ω is used for the electric field, the phase of the light wave at the end of the crystal is

$$\begin{aligned} \phi(t) &= 2\pi\nu t + \Delta\phi(t) = 2\pi\nu t + \frac{2\pi\nu}{c}\frac{l}{d} m_c V_0 \sin(2\pi\Omega t) \\ &= 2\pi\nu t + m\sin(2\pi\Omega t) \end{aligned}$$

with $m = \frac{2\pi\nu}{c}\frac{l}{d}m_c V_0$ being the modulation index. The frequency spectrum of the emitted light is

$$E(t) = E_0 e^{-i2\pi\nu t} e^{-im\sin(2\pi\Omega t)} \tag{5.3}$$

$$= E_0 e^{-i2\pi\nu t} \sum_{n=-\infty}^{\infty} J_n(m) e^{-i2\pi n\Omega t} \tag{5.4}$$

with the n-th Bessel functions[1] $J_n(m)$. The frequencies of the light field are ν (called carrier frequency) and $\nu \pm n\Omega$ (called n-th sideband)(s. figure 5.2(b)). In the present case $m \ll 1$, so only the first order sidebands are considered for further analysis. The electric field of the light beam is then given by

$$E(t) = E_0 e^{-i2\pi\nu t}\left(J_1(m)e^{-i2\pi\Omega t} + J_0(m) + J_{-1}(m)e^{i2\pi\Omega t}\right). \tag{5.5}$$

As long as the amplitude and the phase of the sidebands are not modified by an

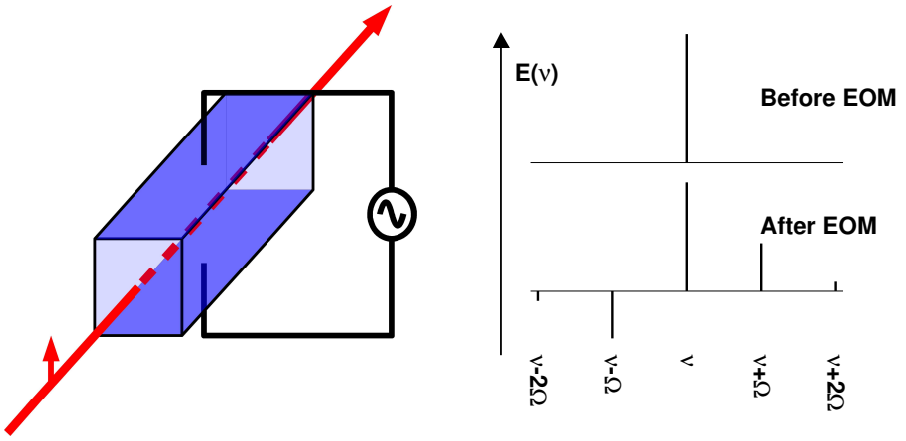

(a) Alignment of the EOM and the light beam.

(b) Frequency spectrum of the electric field of the light beam before and after the EOM.

Figure 5.2: Principle of the EOM

interaction, no signal with the modulation frequency is detectable with a photodiode, because the phase of the ± 1 sidebands is different by π. When the amplitude or phase of the sidebands are modified differently, then a signal with the modulation frequency can be detected. This is the basis of the frequency modulation saturation spectroscopy (FM-spectroscopy), which is explained in the next section.

An important point is that in case the polarization of the light is not exactly parallel to the optical axis (the electric field V), the modulator does not only induce a phase shift. It also acts like a retarder and so the polarization is changed, because the refraction index parallel and perpendicular to the electric field are not equal, if $|V_0| > 0$. If such a

[1] Properties: $J_{-n}(m) = (-1)^n J_n(m)$

light beam is later passed through polarization sensitive optics (this is principle true for all optics), also an amplitude modulation with the modulation frequency is produced. This amplitude modulation will be detected by the photodiode and produces unwanted background in spectroscopy as it will shown further-down.

5.2 Frequency modulation saturation spectroscopy

For laser stabilization a narrow signal with a odd-symmetry line shape and a good signal to noise ratio is desirable. There are several methods to obtain such a signal, which is often based on comparing the physical properties of iodine at different frequencies.

5.2.1 Basics of Doppler free saturation spectroscopy

In a gas cell with a temperature T the velocity distribution of the particles has a Gaussian shape. Due to the Doppler effect[2] particles with a resonance frequency ν_0 and velocity v can interact with a laser-beam of the frequency ν_l

$$\nu_l = \nu_0 \left(1 - \frac{v}{c}\right), \tag{5.6}$$

where v is the velocity component parallel to the laser beam. The laser-beam excites the particles from the ground level to the excited level (it burns a hole, called Bennett hole, in the population distribution of the ground state). So the number of particles in the ground level at velocity v decreases. If now a second laser-beam counter-propagating to the first one is applied, it interacts with particles with the velocity $-v$ (s. figure 5.3)

$$\nu_l = \nu_0 \left(1 + \frac{v}{c}\right). \tag{5.7}$$

Both lasers interact with the particles of the same velocity group, if the particles have zero velocity. The second laser beam, which is weaker than the first laser-beam and does not modify the population distribution compared to the first laser-beam, sees less particles in the ground level and thus the absorption is decreased. The absorption of the second laser-beam as a function of the laser-frequency shows a dip (called Lamb dip), if the laser frequency is equal to the resonance frequency of the particles. The shape of the dip is a Lorentzian function with a linewidth $\gamma_s = \gamma(1 + \sqrt{1+S})$, where γ is the Doppler-free linewidth without saturation and S is the saturation parameter. S can be given as ratio of the used laser power P to a reference laser power called saturation power P_0

$$S = \frac{P}{P_0}.$$

The absorption coefficient for $S < 1$ is given by [Let76]

$$\kappa(\nu) = \kappa_0(\nu) \left[1 - \left(1 - \frac{1}{\sqrt{1+S}}\right) \frac{\left(\frac{\gamma_s}{2}\right)^2}{\left(\frac{\gamma_s}{2}\right)^2 + (\nu - \nu_0)^2}\right]. \tag{5.8}$$

[2] In a gas cell the velocity is in the orders of hundreds m/s, so it is a good approximation to set $\gamma = 1$.

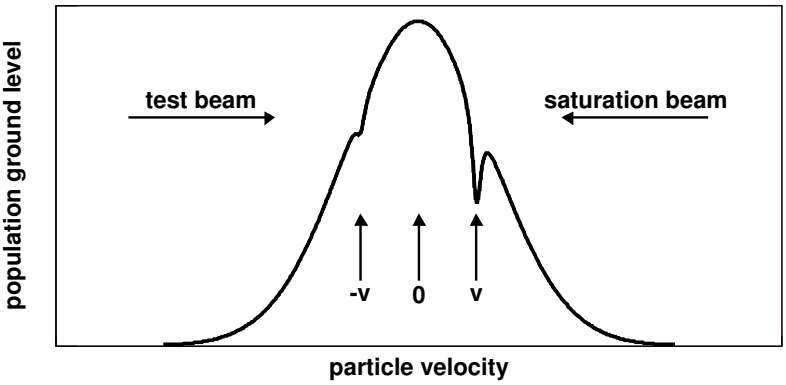

Figure 5.3: Hole burning in the population distribution of the ground level with a strong saturation beam and a weak counter-propagating test beam.

where $\kappa_0(\nu)$ is the absorption coefficient without saturation. The absorption signal of the second laser-beam is a Doppler broadened line with a dip that has a linewidth of the order of the natural linewidth. The Doppler width at room temperature is several hundred MHz and the natural linewidth is in the range of MHz for dipole allowed transitions in the optical frequency range.

5.2.2 Signal of frequency modulation saturation spectroscopy

Now the signal shape is investigated if the weak beam is modulated by an EOM so that sidebands of first order can be generated [BL83].
Because $m \ll 1$ is assumed, the Bessel functions can be written as $J_{\pm 1}(m) = \pm m/2$ and $J_0 = 1$. Putting this approximation in 5.5 one obtains

$$E(t) = E_0 e^{-i2\pi\nu t}\left(-\frac{m}{2}e^{-i2\pi\Omega t} + 1 + \frac{m}{2}e^{i2\pi\Omega t}\right). \tag{5.9}$$

This is the electric field of the light wave before entering a gas cell of the length L with absorption coefficient κ and refraction index n is introduced. The transmission of each frequency component can be written as

$$T_j = e^{-\delta_j - i\phi_j} \text{ with } j = -1, 0, 1 \tag{5.10}$$

$$\delta_j = \kappa_j \frac{L}{2} \tag{5.11}$$

$$\phi_j = 2\pi n_j L \frac{\nu + j\Omega}{c}. \tag{5.12}$$

Here δ_j describes the absorption and ϕ_j the dispersion for the different frequencies $\nu_j = \nu \pm j\Omega$. The electric field after the gas cell is thus formed to be

$$E_a(t) = E_0 e^{-i2\pi\nu t}\left(-T_{-1}\frac{m}{2}e^{-i2\pi\Omega t} + T_0 + T_1\frac{m}{2}e^{i2\pi\Omega t}\right). \tag{5.13}$$

The corresponding intensity detected by a photodiode is proportional to $|E_a(t)|^2$,

$$I_{Photodiode} \propto |E_a(t)|^2. \tag{5.14}$$

Neglecting terms of m^2, and assuming that $|\delta_0 - \delta_{\pm 1}|$ and $|\phi_0 - \phi_{\pm 1}|$ are much smaller than one, we obtain

$$I_{Photodiode} \propto (\delta_{-1} - \delta_1) m \cos(2\pi\Omega t) + (\phi_1 + \phi_{-1} - 2\phi_0) m \sin(2\pi\Omega t). \tag{5.15}$$

The last equation shows that, if the absorption or dispersion are different for the two sideband frequencies then the photodiode detects a signal at the frequency Ω. The absorption can be separated from the dispersion part of the signal by mixing the output of the photodiode with the modulation frequency of the correct phase. If the modulation frequency is small compared to the line width, the absorption part of $I_{Photodiode}$ looks like the first derivative of the absorption curve of the resonance and the dispersion part of $I_{Photodiode}$ looks like the second derivative of the dispersion signal of the resonance [BL83].

As mentioned before, the absorption shape of the saturation signal is a Lorentzian function

$$\delta(\nu) = \delta_{peak} \frac{\gamma_s^2/4}{(\nu - \nu_0)^2 + \gamma_s^2/4}, \tag{5.16}$$

and the corresponding dispersion is given by

$$\phi(\nu) = \delta_{peak} \frac{\gamma_s^2/4}{(\nu - \nu_0)^2 + \gamma_s^2/4} (\nu - \nu_0), \tag{5.17}$$

where δ_{peak} is the maximum of the absorption. In figure 5.4 examples for the absorption and the dispersion part of $I_{Photodiode}$ are shown for two different modulation frequencies. It follows from eq. 5.8 that the absorption coefficient also contains a broad background contribution due to the Doppler broadening. The used frequency modulation spectroscopy is therefore not a Doppler background free spectroscopy, because all of the explanations are valid for all absorption profiles. As mentioned before, if the modulation frequency is smaller than the line width, the measured signals are derivatives of the absorption profile, so the signal of the broad Doppler signal is less intense because the slope is smaller than that of the narrow saturation signal. The measured signals look like in figure 5.4 but with a small Doppler background.

5.2.3 Setup

The setup for iodine spectroscopy used in the present work is illustrated in figure 5.5 and is derived from other setups [HHBR81][AB93][CGS00]. The intensities of the weak test and strong saturation beam are controlled by a $\lambda/2$-retarder and a polarization beam splitter (PBS). The test beam power is usually by a factor of ten smaller as compared to the saturation beam power. An electro-optic modulator (EOM, Type Newfocus Model 4002 or a self-made device provided by K. Jungmann[Gab94]) creates sidebands

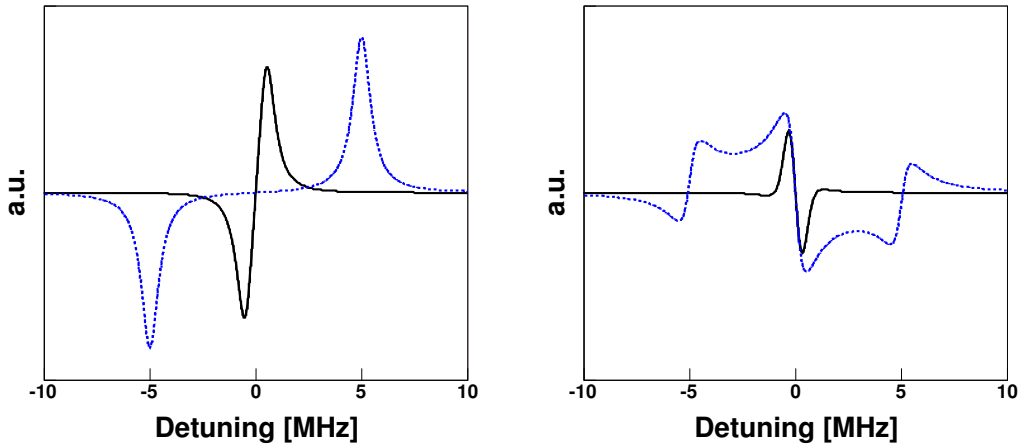

Figure 5.4: Signal examples of FM-spectroscopy neglecting the Doppler background. In the left panel the absorption and in the right panel the dispersion signal is shown (solid line $\Omega = 1$ MHz, dashed line $\Omega = 5$ MHz, $\gamma_s = 1$ MHz).

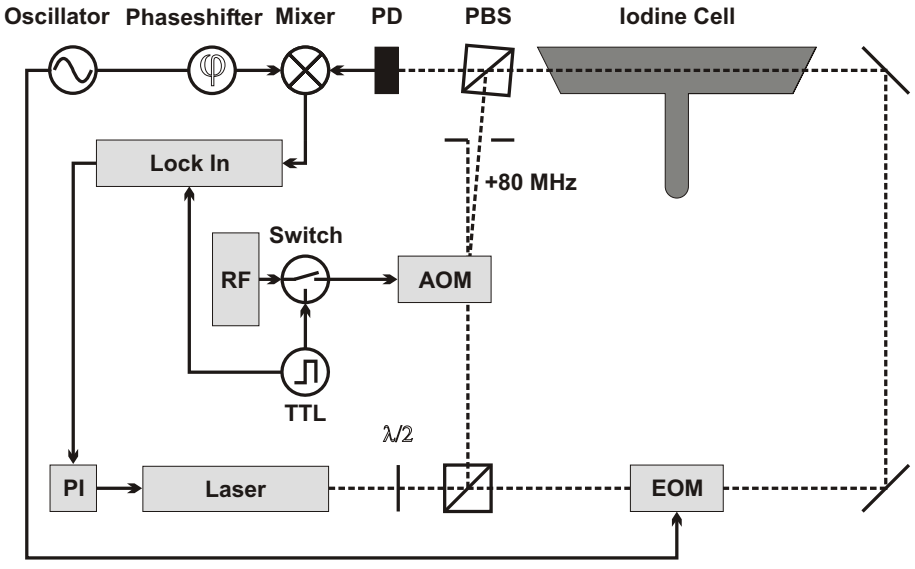

Figure 5.5: Overview of the used iodine spectroscopy

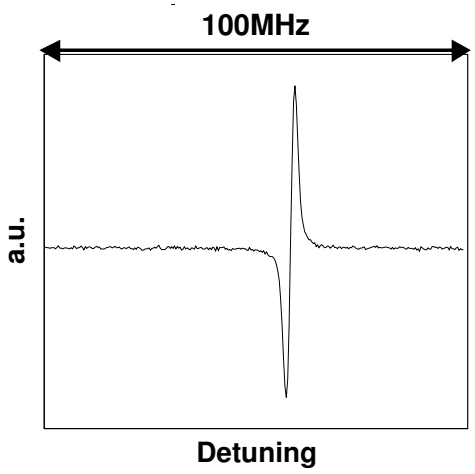

Figure 5.6: Signal of an iodine line obtained by FM-spectroscopy

with a modulation frequency of one to two MHz on the test beam. The saturation beam is frequency shifted by an acousto-optic modulator (AOM, Type 1205C-1 from ISOMET) to higher frequency. Normally the shift is 80 MHz. This is necessary to avoid interferometric noise [SRBD80]. The AOM is also used as a chopper with a chopping frequency of about 50 kHz by a rf-switcher (Type ZASWA-2-50DR from Minicircuits[3]). This is done for suppressing the Doppler background. Test- and saturation beams are overlapped in the gas cell and after the test beam is traveled through the iodine cell[4] it is extracted by a PBS and directed to a fast photodiode (Type PDA155-EC from Thorlabs).

If there is an amplitude or phase difference, the photodiode detect a heterodyne frequency at the modulation frequency of the EOM. The amplitude of the heterodyne frequency is measured by mixing the photodiode signal with the modulation frequency. With a phase shifter between the reference and the signal the absorption or the dispersion signal is selected as output signal of the mixer (s. equation 5.15). After the mixer a low pass suppresses frequencies that are higher than the chopper frequency. Because the signal now has a Doppler background, a further signal processing is necessary by a lock-in amplifier. The reference signal of the lock-in amplifier is the chopper frequency. With the lock-in amplifier the Doppler background is subtracted, because the test beam has a saturation signal, if the saturation beam is on, and a normal Doppler boarded signal, if the saturation beam is off. After the lock-in amplifier, an odd signal with no Doppler background and a good signal-to-noise ratio is obtained and serves as error signal for a PI-controller to hold the laser in the center of the line. An example for an background free FM-signal is shown in figure 5.6.

The advantage of this setup is a flat background and the good signal-to-noise ratio,

[3]In [Saa02] the same type is used and a rise time of about 7 μs is measured, which is to long for switching frequencies up to 100 kHz. By replacing this devices by new one switching frequencies up to 1 MHz are now possible with a rise time of lower than 50 ns.

[4]All used iodine cells are calibrated by the Physikalisch Technische Bundesanstalt. The calibration numbers are 1/99 and 15/98.

so the light power necessary for a sufficient signal is only in the order of a few mW at a laser beam diameter of one or two millimeters. The good signal-to-noise ratio is due to the high modulation frequency of the EOM, which is higher than the frequencies of the main noise sources of a laser (in particular of a dye laser).

Another advantage is that there is no danger of a residual amplitude modulation [GB85] like in the frequency modulation transfer spectroscopy[5] [JC98], which can produce an offset the signal if the EOM is not well aligned to the polarization axis of the saturation beam. When the saturation beam passes a polarization sensitive device, amplitude modulation at the frequency of the EOM is observed. The test beam sees not only a frequency modulated saturation beam it sees also an amplitude modulated saturation beam. The amplitude modulation contributes an additional signal to the signal of the frequency modulation after demodulation with the mixer, which is the final signal. This can not happen with the used setup, because the demodulated signal, that can contain contributions from the residual amplitude modulation of the test beam, is filtered by the lock-in amplifier and after this only signals generated by the saturation of the medium are visible.

In the present setup, the frequency of the test beam and the saturation beam is different by the constant frequency shift of the AOM. This leads to a frequency shift of the measured resonance frequency.

If two laser beams with different frequency ν_1 and ν_2 are used for saturation spectroscopy[6], there exists a velocity class where both beams are in resonance with particles with the transition frequency ν_0.

$$\begin{aligned} \nu_1 &= \nu_0(1 - v/c) && (5.18)\\ \nu_2 &= \nu_0(1 + v/c) && (5.19)\\ \Rightarrow \frac{\nu_1 + \nu_2}{2} &= \nu_0 && (5.20) \end{aligned}$$

The particle is in resonance with the laser-fields, if the mean value of ν_1 and ν_2 is equal to the transition frequency of the particle. If $\nu_1 = \nu_2$ then $\nu_1 = \nu_0$, so the transition frequency is equal the frequency of the laser. At a frequency difference of $\Delta\nu_{12} = \nu_1 - \nu_2$ produced by the AOM, the transition frequency is equal the frequency $\nu_1 + \Delta\nu_{12}/2$. So in the used setup, the frequency of the stabilized laser is equal to $\nu_0 - \Delta\nu_{12}/2$.

[5]The setup of frequency modulation transfer spectroscopy is similar to the used setup. The EOM is placed in the saturation beam after the AOM and the AOM is not chopped. In the test beam no optical device is placed.

[6]As long as the frequency difference is small compared to the Doppler width of the transition.

Chapter 6

Spectroscopy of the lithium ion

The spectroscopy of the stored lithium ions is in principle a normal saturation spectroscopy with amplitude modulation of the beams for background subtraction. Remarkable is the high velocity of the ions of three respectively six percent of the speed of light. This leads to several effects like the high detuning of the used laser frequencies of several ten nanometers away from the transition wavelength at rest. The large shifts mainly stem from the classical Doppler effect. Also a frequency shift due to the curvature of the laser phase fronts is not a usual problem in Doppler free saturation spectroscopy.

6.1 Setup

The experimental setup is separated in two parts, the laser system and the spectroscopy setup at the TSR, which are connected by an optical fiber. An overview is given in figure 6.1.

6.1.1 Laser system

The frequencies of the lasers must be known to a level of 10^{-10} to ensure the desired accuracy for the test of time dilation. These frequencies are determined relative to transition frequencies of hyperfine-structure components of molecular iodine as explained in chapter 5. The light parallel to the ions is generated by a fixed-frequency laser[1] of the desired wavelength. A frequency-doubled Nd:YAG laser at 532 nm (Type Diabolo from Innolight) is used for the measurement at $\beta = 0.03$. The control signal of the PI-controller from the iodine spectroscopy is applied to a piezo-mounted mirror in the laser cavity to compensate short time frequency variations and to the temperature controller of the laser crystal for long term variations. At $\beta = 0.064$ an argon ion laser at 514 nm (Type 85-1 from Lexel) is used. For short term frequency variations the laser is locked to an external cavity with a free spectral range of 300 MHz (Tec optics, SA300) employing a piezo-mounted mirror in the laser cavity. The external cavity length is stabilized

[1] The laser frequency can be controlled over several GHz, but during the experiment the laser operates at the same frequency.

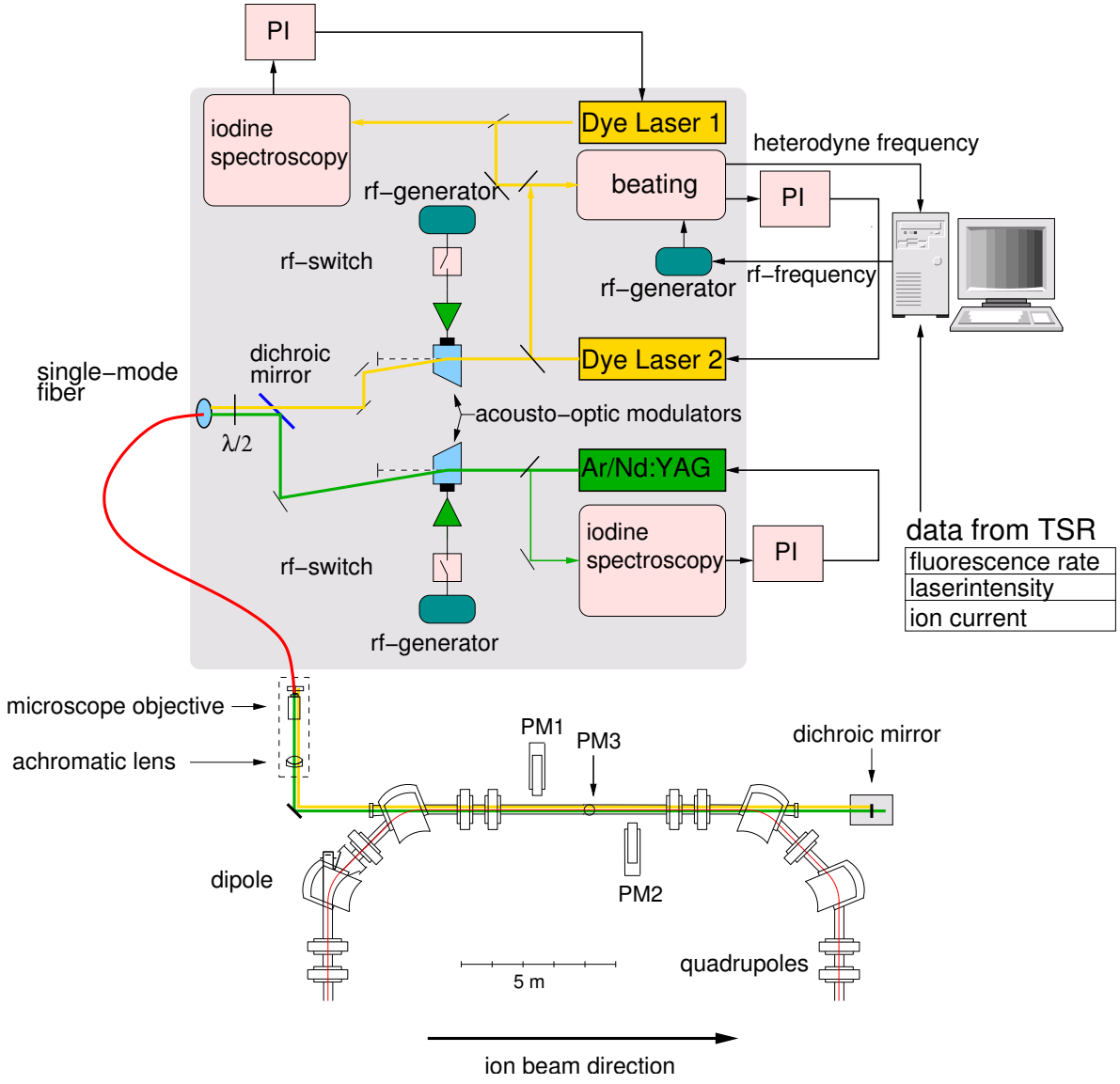

Figure 6.1: Overview of the setup for the lithium spectroscopy at the storage ring.

by the iodine spectroscopy using a piezo-mounted mirror of the external cavity (details [Saa02]). The second laser beam, which runs antiparallel to the ion beam must by tuned in frequency. For this a dye laser Dye2 (Type CR699-21 from Coherent) is used, which is locked to a second iodine stabilized dye laser Dye1 (Type CR599-21 from Coherent) by frequency offset locking. Both dye lasers use sapphire nozzles for a good dye jet quality. As dye, Rhodamin 6G is used at an operating pressure of 9 bar and a temperature of 16 °C. Both dye lasers are pumped by the same, frequency-doubled Nd:YAG-laser at 532 nm (Type Verdi-V10 from Coherent): the pump power for Dye2 is between 5 and 6 W and for Dye1 it is between 2 and 3 W. For controlling the frequency of the dye lasers the standard input is used, that tilts a glass plate in the reference resonator of the laser.

The principle of frequency offset locking [SEWZ99] is to compare the frequency difference ν_{beat} of the two lasers, measured with a fast photodiode (Type 6045 from Hamamatsu) with the frequency ν_{rf} of a signal generator. To tune the frequency of laser Dye2, the frequency difference between ν_{beat} and ν_{rf} is kept fixed. If ν_{rf} is changed, ν_{beat} is thus changed by the same value. The electronic setup used is shown in figure 6.2. The signal of the photodiode is filtered by a high pass filter and amplified[2] before

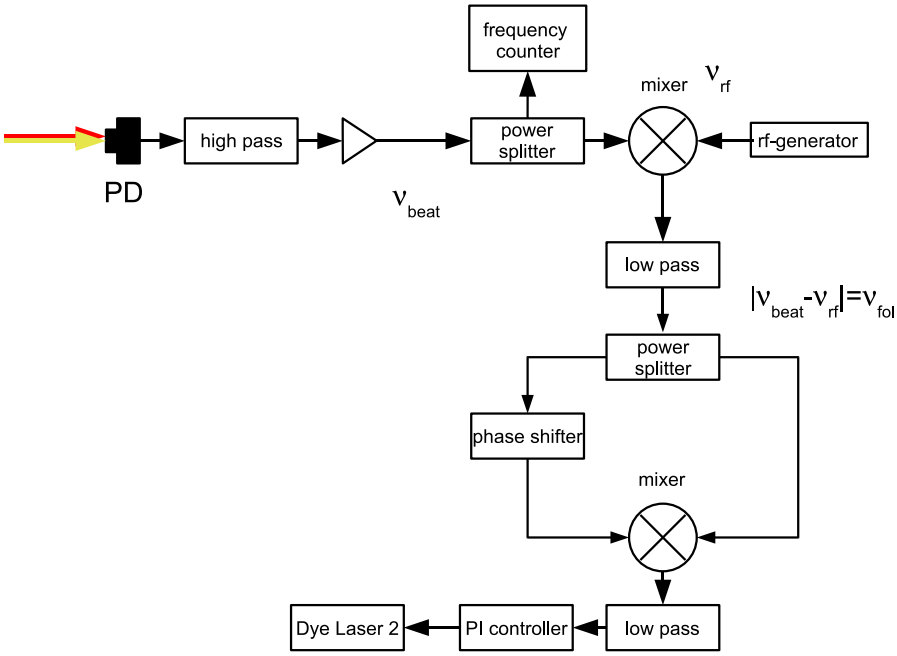

Figure 6.2: Schematic setup for frequency offset locking. The two laser beams with the same polarization direction are superimposed on a fast photodiode PD to measure and control the frequency difference. In figure 6.1 this setup is labeled as “beating”.

it is splitted into two parts, one for the frequency counter (Type 53181A-050/001 from AGILENT) and one for the frequency offset locking. The heterodyne signal ν_{beat} is mixed with the reference frequency ν_{rf}, generating the difference and the sum of the frequencies. A low pass cancels out the sum frequency so that only the frequency difference $\nu_{fol} = |\nu_{beat} - \nu_{RF}|$ is entering the power splitter. The splitted signals s_1 and

[2]The amplified signal is at least 30 dB stronger than the noise level.

s_2 go through two different cables of different length before they are mixed (indicated by the phase shifter in figure 6.2). Again, the sum frequency is suppressed by a low pass. The phase difference ϕ_{Phase} of the two signals is proportional to the length difference ΔL of the two cables.

$$\begin{aligned} \phi_{Phase} &= 2\pi\frac{\Delta L \nu_{fol}}{c_{wire}} \ (c_{wire}\text{=signal velocity in the wire}) \\ s_1 &= \cos(2\pi\nu_{fol}t + \phi_{Phase}) \\ s_2 &= \cos(2\pi\nu_{fol}t) \\ s1 \cdot s2 &= \frac{1}{2}(\cancel{\cos(4\pi\nu_{fol}t + \phi_{Phase})} + \cos(\phi_{Phase})) \end{aligned}$$

After the low pass, a signal is available which is proportional to the cosine of the phase difference ϕ_{Phase} and this phase is a function of ν_{fol}. If ν_{fol} is changed then ϕ_{Phase} is changed and this can be detected and used as an error signal for a PI-controller, that locks the laser on one of the zero crossings of the cosine. In figure 6.3, a theoretical signal and a measured signal is compared. Two successive zero crossings with the same

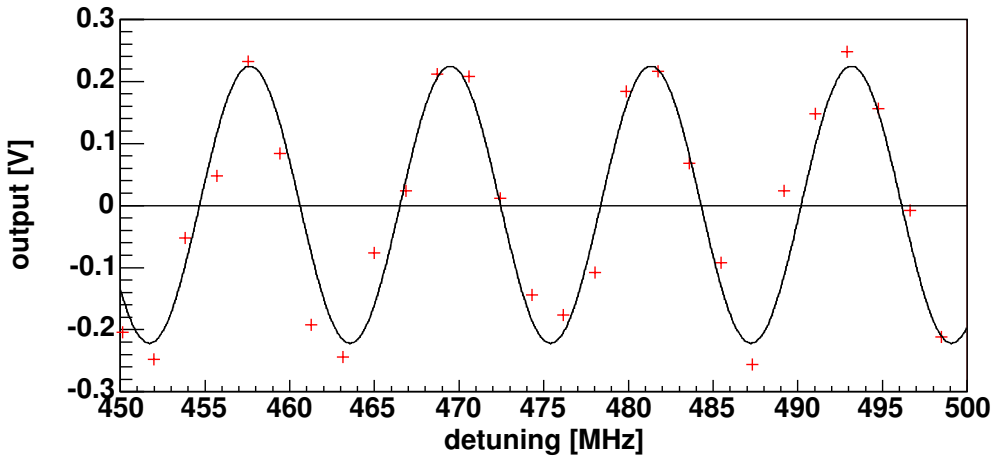

Figure 6.3: The output signal of the electronic setup for the frequency offset locking scheme compared to a cosine. In order to observe several oscillations in this measurement the delay line for the phase difference was much longer (≈10 m) compared to the delay line used in the experiment.

slope are separated by $\Delta\nu_{fol} = c_{wire}/\Delta L$, if ΔL is fixed. In the experiment, the scan width of Dye2 is usually 200 MHz or below, so the length difference of the two paths are chosen such that the laser can not jump to the next zero crossing of the cosine; in the experiment, the path difference was approximately 0.5 m to have a $\Delta\nu_{fol}$ of clearly higher than 200 MHz. A setup with only one zero crossing using filter technique does not have this problem [RCGW04]. In figure 6.4 the linearity and stability of frequency offset locking is shown. The reproducibility of the lock varies slightly over the frequency range shown, but the frequency difference of Dye1 and Dye2 can be controlled on a level of 100 kHz and is always measured with the frequency counter for frequency determination. If

now Dye1 is stabilized to a iodine line with a known frequency, the absolute frequency of Dye2 can be determinated by adding (Dye2 is higher in frequency than Dye1) or subtracting (Dye2 is lower in frequency than Dye1) the measured heterodyne frequency from this frequency. With this method the frequency of Dye2 can be changed in any conceivable way (like linear or randomly) and at every point the frequency is known.

The amplitude modulation the light of the fixed frequency laser and of the laser Dye2 is performed by guiding the laser beams through AOMs with a center frequency of 200 MHz (Type 3200-121 from Crystal Technology). The rf-power of these AOMs can be individually switched on and off like the pump beam in the iodine spectroscopy, i. e. the scattered light can be switched on and off. After this the light is combined by a dichroic mirror and is coupled in a single mode polarization maintaining optical fiber (Type HB450 with one skew end from Fibercore). An achromatic $\lambda/2$-retarder (Type RAC 3.2.15 from B. Halle) is placed in front of the fiber to adjust the polarization. The linear polarization of both laser beams must be parallel to the optical axis of the fiber to ensure stable linearly polarized light beam at the end of the fiber.

6.1.2 Setup at the TSR

The setup at the TSR consists of the opto-mechanical part for overlapping the laser beams with the ion beam and a detector part to observe the fluorescence light of the ions. The setup is nearly identical used by G. Saathoff [Saa02].

To overlap the laser beams with the ion-beam, one has to be able to translate and to tilt the laser beams. This is achieved by two mirrors which are mounted on translation stages with stepper motors. One of these mirrors can also be tilt vertically and horizontally. The accuracy of the translation and rotation are 1.2 μm and 12.3 μrad, respectively. In figure 6.5 is shown how this realized at the TSR. For adjusting the laser beam profile, a microscope objective (10×) directly after the fiber and an achromatic lens (f=600 mm) before the first mirror is used. The polarization of the out-coming beam is rotated by a achromatic $\lambda/2$-retarder (Type RAC 3.2.15 from B. Halle) and a polarization beam splitter ensures, that over 98% of the laser power is linearly polarized. After the two mirrors, an achromatic $\lambda/4$-retarder (Type RAC 3.4.15 from B. Halle) can be placed for changing the polarization from linear to elliptical. Because both laser beams are transported by the same fiber, they go the same way through the TSR. To minimize the background through scattered light, the laser beam, which interacts at the first pass through the TSR, is coupled out by a dichroic mirror on the other side of the TSR. The other laser beam is reflected by this mirror. To reflect the laser beam back the same way, the mirror is mounted on rotating stages with stepper motors to tilt the beam in vertical and horizontal direction. The entrance windows of the ring are adjusted such that the reflections of the lasers from the window surfaces leave the ring on the opposite side to reduce signals due to scattered light at the detector, but they are not overlapped with the laser beams to avoid a variation of the laser intensity due to an etalon effect.

Three photomultipliers are used for the detection of the fluorescence light from the ions. Two photomultipliers (called PM2 and PM3, both type R2256P from Hamamatsu) are equipped with an imaging system and are used for measuring the saturation signal.

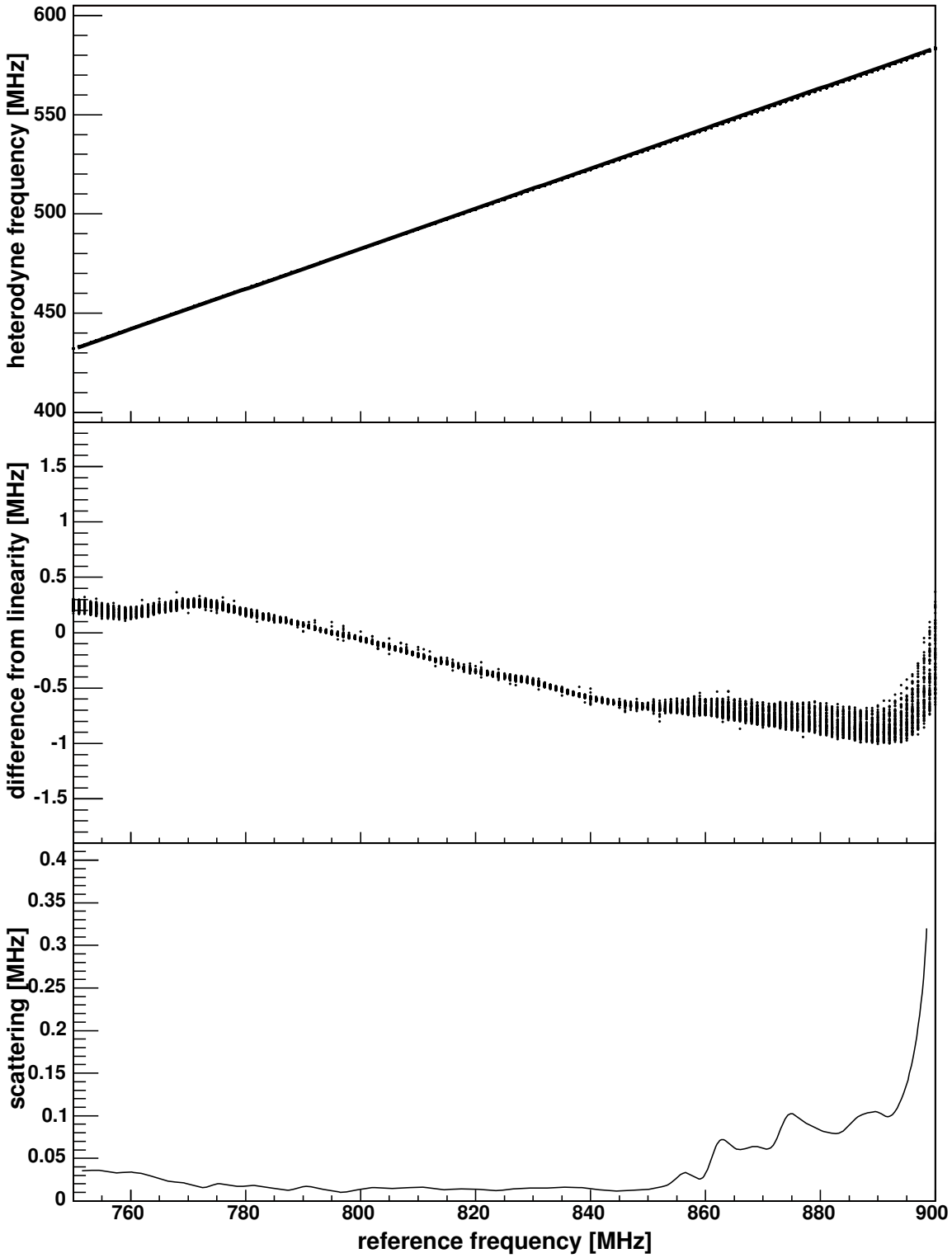

Figure 6.4: The upper picture shows how good the linearity of a frequency scan with frequency offset locking is. The middle picture is the subtraction of the measured beat frequency and a linear fit from the upper picture. The lower picture shows the width of the scattering of the measured beat frequency and illustrates the reproducibility. The data consist of 64 subsequent frequency scans.

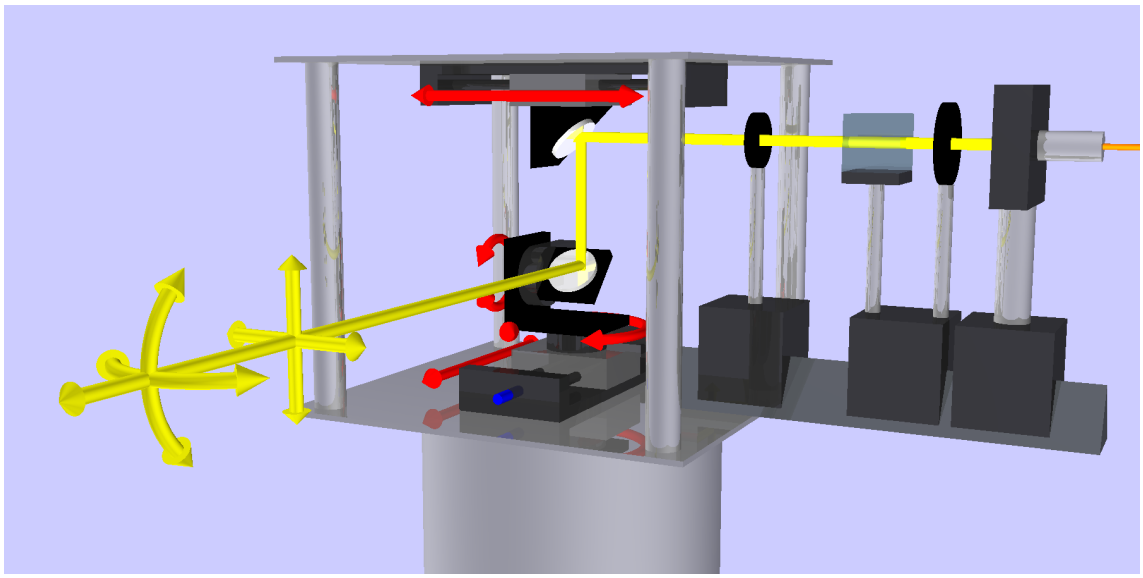

Figure 6.5: Construction (called tower) to translate and tilt the laser beams for a parallel overlap with the ion beam.

The third one (PM1, type 9635QB from Thorn EMI) is only used for optimizing the overlap between the laser beams and the ion beam. The imaging system of PM3, explained in [Mer00], is imaging a point of the ion beam to a point on the detector. A polished metal, that acts as mirror, is placed on the opposite side in the beam tube to enhance the signal; its shape is a concave cylinder, which in the ideal case reflects a photon from the ion beam that is in the middle of the beam tube, the same way back to PM3. The imaging system of PM2 was newly designed and is shown in figure 6.6 and 6.7 and imaging a line to a point.

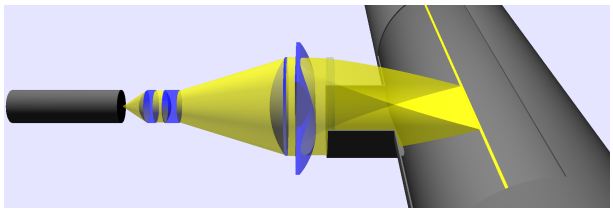

Figure 6.6: Illustration of the imaging properties of PM2.

For applying a magnetic field with defined strength and direction for test purposes, a coil with a length of 20 cm and a diameter of 28.5 cm is placed around the beam tube of the TSR close in front of photomultiplier PM3. The magnetic field normalized to one ampere current of the coil is shown in figure 6.8. The magnetic field is positive if the magnetic field is parallel to the ion beam.

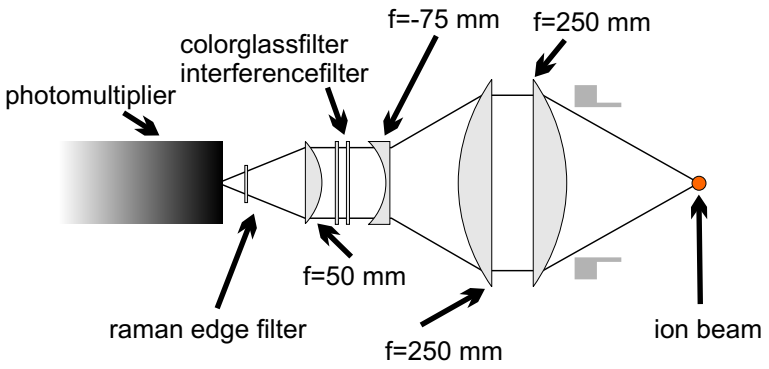

Figure 6.7: Schematic of the optical system of PM2. The light from the ion beam is first focused in one dimension by a cylindric lens (custom-made with 150 mm edge length from Berliner Glas). After this the light is imaged to a parallel beam with a diameter below 5 cm so that in a range, where the light has a small divergence, colorglassfilters (OG515, OG530) and an interferencefilter (transmission 548 nm, half-width 10 nm (s. [Mer00])) are placed. Shortly in front of the photomultiplier, a Raman edge filter (1 inch diameter, type SEM-LP01-532RS-25 from Semrock) is placed, that blocks light of 532 nm and below (the position is not optimal due to the high divergence of the light). All lenses are anti-reflection coated.

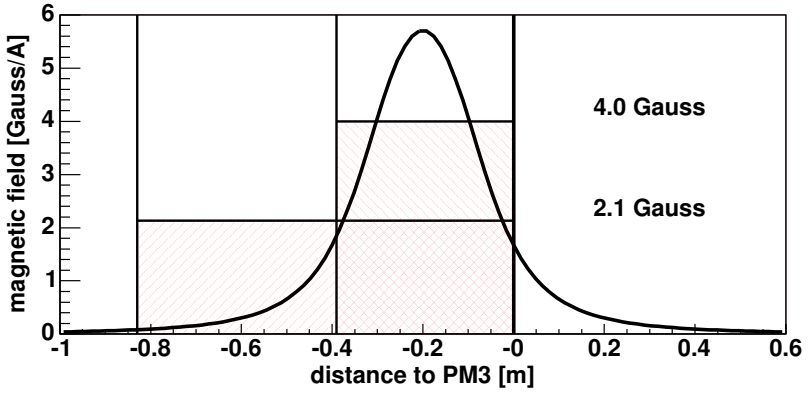

Figure 6.8: Field strength of the magnetic field normalized to one ampere. Also given are the mean magnetic field seen by the $^7Li^+$ ions within the lifetime of the excited state of the ion of 43 ns. At $\beta = 0.03$ the mean field is 4 Gauss/A and 2.1 Gauss/A for $\beta = 0.064$.

6.1.3 Data-acquisition

The signals of the photons detected by the photomultipliers are discriminated and converted such that they can be counted by scalers. For the subtraction of the Doppler background it is necessary to detect the fluorescence signal in different scalers depending on which laser beams are on or off. The following states of the laser beams are used (s. figure 6.9): Both laser beams are on (3), only one laser is on (2), only the other laser is on (1) and no laser beam is in the TSR (0). For each of these states, the fluorescence is counted in separate scalers. The lasers are continuously switched between these four states and every state has a duration of $\Delta t = 1/f$ (f called switching frequency) for signal integration. In state (3) the saturation signal is detected. In state (1) or (2) the Doppler broadened signal from each laser beam is counted. State (0) contains the dark rate of the photomultipliers. If now the sum of states (1) and (2) is subtracted from the signal from state (3), a Doppler- and background-free saturation signal is obtained. To make sure that signals from particular states are not counted into a wrong scaler, the signal of the photomultiplier is blocked for the first 1 μs after the state is changed and for the last 1 μs before the state ends.

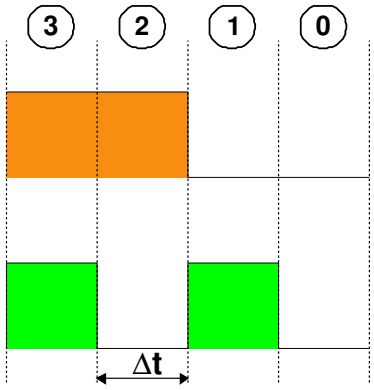

0. scaler: Dark counts

1. scaler: Fluorescence counts, if one laser in the TSR

2. scaler: Fluorescence counts, if the other laser in the TSR

3. scaler: Fluorescence counts, if both lasers in the TSR (saturation signal)

Figure 6.9: Different states of the laser beams used in the measurements. Typical values for Δt are 10 to 200 μs.

In addition to the fluorescence signal, a signal proportional to the number of stored ions is recorded. It is generated by the BPM which is explained in section 4.2.2 and is used for normalization purposes.

6.2 Measurement procedure

To measure the transition frequency of the lithium ion, three steps are necessary. All these measurements are carried out after the ion beam is cooled by the electron cooler. The first step is to adjust the velocity of the ions such that the peak of the velocity distribution is coincident with the velocity of the ions the fixed frequency laser is talking to. This step is coarsely done by tuning the velocity of the electrons of the electron

cooler. For a fine tuning the ion beam is bunched which allows to make small correction of the position of the velocity distribution. The buncher also compensates small drifts caused by the electron cooler. The bunching frequency is the ninth harmonic of the ion revolution frequency. The applied voltage amplitude is 30 V peak to peak. To verify the proper alignment, a 5 to 6 GHz frequency scan is carried out with Dye2 to observer the whole velocity distribution.

The second step is to optimize the geometrical overlap between the ion beam and the laser beams. This is done by an overlap scan accomplished by horizontally and vertically moving the laser beam with the mirrors. Only the fixed frequency laser, which is only traveling one time through to the TSR is used for this optimization. During the scan the fluorescence of the photomultipliers is recorded as a function of the mirror position. If an angle exists between the ion-beam and the laser beam, the maxima of the fluorescence signal observed at the three photomultipliers appear at different mirror positions as explained in figure 6.10. After having corrected any misalignments, a further scan is done to monitor the overlap.

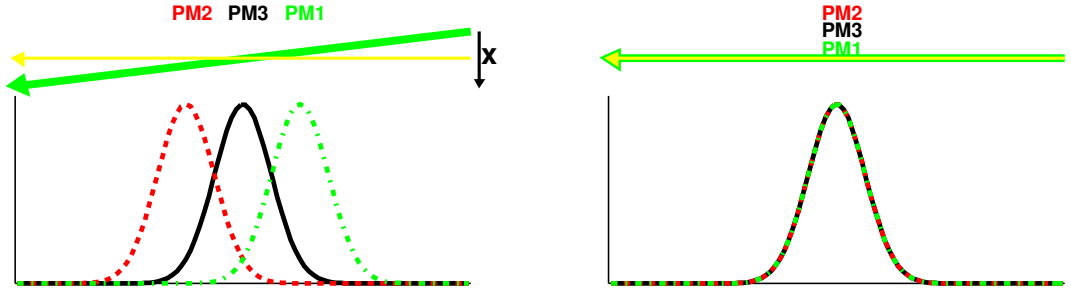

Figure 6.10: Optimization of the overlap between ion-beam and laser beam. The procedure is the same for both transversal directions.

The third step is the frequency measurement of transition frequency of the fast lithium ions. The frequency of Dye2 is scanned using the frequency offset locking setup. The range of a frequency scan is 60 MHz to 200 MHz depending on the power of the laser beams and the corresponding saturation broadening. A frequency scan consist of about 200 data points with a dwell time of 0.1 s for each data point. For each data point the laser beams are switched for background subtraction as mentioned before. Because of the decay of the metastable state and of the ion beam the frequency scan is subdivided into partial scans of $t_m \sim 5 - 8$ s, after which a new beam is injected into the TSR. After each injection the ion beam is cooled for $t_e \approx 10$ s (s. figure 6.11). The time for a full frequency scan is 20 s to 40 s, so one frequency scan is carried out over several injections. The number of data points for a full frequency scan and the number of data points per injection is chosen such, that they are not multiplies of each other. The laser beams are switched off while the tuneable laser changes its frequency between two data points. After several frequency scans the variation of the ion beam properties averages out at each data point.

The whole control and data acquisition of the experiment is done by a program developed with LabVIEW^{TM}.

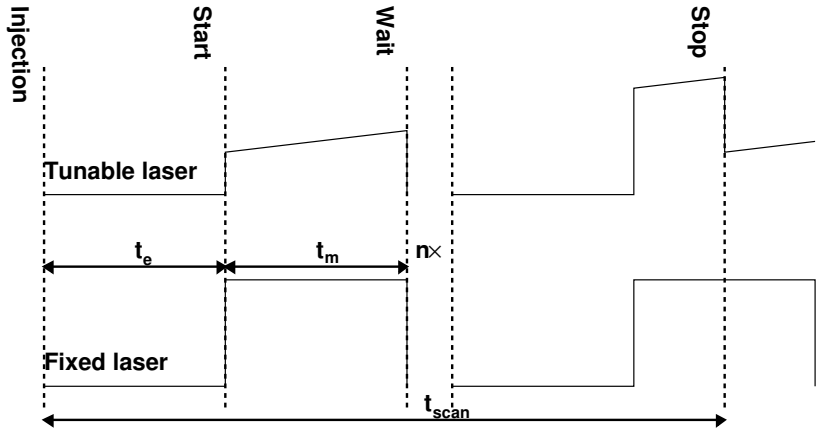

Figure 6.11: Time scheme of a frequency measurement. The electron cooler and buncher are always on. The lasers are in the TSR after the cooling time t_e and the tunable laser changes its frequency by the desired value. After the time t_e+t_m a part of the frequency scan is finished and the tunable laser waits for the next injections to continue the frequency scan. This is repeated n times until the tunable laser reaches its final frequency. The frequency scan is stopped and the laser jumps to the start frequency for the next scan. The time for one complete frequency scan is t_{scan}. A measurement consist of several frequency scans until the statistic is good enough for an analysis.

6.3 Line shape and position

The line shape of the Doppler free saturation spectroscopy with fast $^7Li^+$ ions differs from the line shape of the iodine spectroscopy due to the different detection mechanisms and properties, but the basic principles are the same. Due to the high velocity of the $^7Li^+$ ions however special attention has to be paid to the alignment of the laser beams with the ion beam, and to the fact that the laser beams are not plane waves as assumed so far but rather Gaussian beams.

6.3.1 Basic line shape

The line shape after the Doppler background subtraction is a Lorentz function as at the iodine spectroscopy with a small modification due to the fact that both beams have comparable power. The absorption coefficient is ($S < 1$)[Dem03]

$$\kappa(\nu) = \kappa_0(\nu)\left[1 - \frac{S}{2}\left(1 + \frac{\left(\frac{\gamma_s}{2}\right)^2}{\left(\frac{\gamma_s}{2}\right)^2 + (\nu - \nu_0)^2}\right)\right]. \quad (6.1)$$

The linewidth in this case is $\gamma_s = \gamma\sqrt{1+S}$. Another way to obtain a background free spectroscopy by subtraction is to divide the signal by the Doppler background $\kappa_0(\nu)$. Then, from the amplitude of the Lorentz function, the saturation parameter can be obtained. But this only works if the measured signals are free from offsets and this is not the case mainly because of the background produced by scattered laser light. One of the differences between the lithium ion spectroscopy and the iodine spectroscopy is

due to the large velocity of the ions. The mean iodine velocity is 135 m/s at 6 °C ($\hat{=}\beta = 4.5 \cdot 10^{-7}$) so the iodine molecule stays in principle at the same place and sees the same environmental conditions all the time. The lithium ion flies a distance of 0.4 m ($\beta = 0.03$) and 0.8 m ($\beta = 0.064$) during the lifetime $\tau = 43$ ns of the excited state. Over this distance the environmental conditions (e.g. magnetic stay fields, laser intensity) can change and can modify the detected fluorescence line shape and position. The detected fluorescence signal $N_{signal}(\nu)$ is

$$N_{signal}(\nu) = \int_0^\infty \kappa(t,\nu)\frac{e^{-\frac{t}{\tau}}}{\tau}dt. \tag{6.2}$$

$\kappa(t,\nu)$ is the line shape at the time t and includes all effects which can affect the spectroscopy. The zero point is the time, when the ions reach the photomultiplier and t is the time that has elapsed since the ion interacted with the light field. ν is the frequency of the light field. With the known ion velocity, the time can be translated in a length by $l = vt$. If there is no external influence, $\kappa(t,\nu) = \kappa(\nu)$ is equal to 6.1. 95% of the measured signal is produced by ions which interact with light within three lifetimes $t = 3\tau$ before they reach the photomultiplier. The flight length for this time is 1.2 m ($\beta = 0.03$) and 2.5 m ($\beta = 0.064$). For perfect spectroscopic conditions this length should be free from any electromagnetic field, which can shift the transition frequency. The time to produce 50 percent of the signal is $\tau \ln 2 = 30$ ns. For the two ion velocities this is equal to 27 cm ($\beta = 0.03$) and 58 cm ($\beta = 0.064$) before the ions reach the position of the photomultiplier.

6.3.2 Saturation spectroscopy with bichromatic laser beams

If one laser is fixed in frequency and the other one is tuned over a frequency range the ions see a frequency scan that is unequal to the frequency change of the laser. This is already indicated in the classical treatment of saturation spectroscopy illustrated in section 5.2.3 and is now discussed for the relativistic case. If we want to measure a transition with the transition frequency ν_0 and a full linewidth $\Delta\nu$ and one laser is parallel to the direction of motion of the ions and has a fixed frequency ν_p, the frequency ν_a of the laser, which is antiparallel to the particle, must be tuned by $\Delta\nu_a$:

$$\nu_{a1}\nu_p = (\nu_0 + \Delta\nu/2)^2 \tag{6.3}$$

$$\nu_{a2}\nu_p = (\nu_0 - \Delta\nu/2)^2 \tag{6.4}$$

$$\Delta\nu_a = \nu_{a1} - \nu_{a2} = \frac{2\nu_0\Delta\nu}{\nu_p} \tag{6.5}$$

$$= \frac{2\nu_a\Delta\nu}{\nu_0} \text{ with } \nu_a\nu_p = \nu_0^2 \tag{6.6}$$

$$\Rightarrow \Delta\nu = \frac{\nu_0}{2\nu_a}\Delta\nu_a \tag{6.7}$$

The laser must be tuned twice the linewidth multiplied by the ratio of the laser frequency to the transition frequency. If the ratio is smaller than 0.5, $\Delta\nu_a$ is smaller than the

linewidth $\Delta\nu$. If now the roles of the lasers are exchanged, $\Delta\nu_p$ is at least by a factor of two bigger than $\Delta\nu$. Therefore in order to scan over the linewidth $\Delta\nu$, it is necessary to tune the laser by more than $2\Delta\nu$. This aspect was always neglected in earlier works of the time dilation experiments at the TSR, so in all the works the linewidth is roughly by a factor of 2 too large.

6.3.3 Line width

Two line broadening mechanisms beyond the natural line width will be discussed, which mainly influence the line width. The first one is due to the saturation of the medium, called saturation broadening, and the second one is caused by the finite interaction time between the ion beam and the laser field.

Saturation broadening The linewidth of the measured line is a function of the applied laser power due to the saturation of the transition. The linewidth is

$$\gamma_s = \gamma\sqrt{1+S}. \tag{6.8}$$

The saturation parameter S can be given as ratio of the applied laser powers P to a reference power P_0.

Transit-time broadening The interaction time between the ion beam and the light field is different for the different photomultipliers. Until to the position of PM1 the ions have interacted with the laser for the time T, which is not exactly known, as the overlap of the laser beams with the bent ion beam within the dipole and quadrupole magnets in front of the experimental section is not known. This time increases at PM3 by 42 ns and at PM2 by 125 ns ($\beta = 0.064$). For the ions the laser field $E(t) = E_0\cos(2\pi\nu_0 t)$ is switched on and stays until the ions reach the position of a photomultiplier. This can be seen as a rectangular function and the Fourier transform is [Dem03]

$$A(2\pi\nu) \;=\; \frac{1}{\sqrt{2\pi}}\int_0^T E(t)e^{-i2\pi\nu t}dt. \tag{6.9}$$

The spectral intensity profile is

$$I(2\pi\nu) \;=\; A^*A \propto \frac{\sin^2(2\pi(\nu-\nu_0)T/2)}{4\pi^2(\nu-\nu_0)^2}. \tag{6.10}$$

The ions see the laser field with a frequency width of $\Delta\nu_{laser} = 0.9/T$. To get the line profile of the transition the convolution of $I(2\pi\nu)$ with the Lorentz function must be calculated

$$L(\Omega') \;=\; \int_{-\infty}^{\infty}\frac{\sin(\Omega T/2)^2}{\Omega^2}\frac{2\pi\Delta\nu}{(\Omega-\Omega')^2+(2\pi\Delta\nu/2)^2}d\Omega. \tag{6.11}$$

$\Omega = 2\pi(\nu-\nu_0)$ is the detuning and $\Omega' = 2\pi\nu'$ is the point, where the line profile is calculated.

6.3.4 Line position

Influence of the ion beam divergence If there is an angle θ between the two perfectly overlapped counter-propagating laser beams and an ion beam, the measured frequency is shifted due to the Doppler effect. Starting with the Doppler formula

$$\nu_0 = \nu_a'\gamma(1+\beta\cos(\theta)) \tag{6.12}$$
$$\nu_0 = \nu_p'\gamma(1-\beta\cos(\theta)) \tag{6.13}$$

and using $\nu_0^2 = \nu_a\nu_p$, $\Delta\nu_a = \nu_a' - \nu_a$, $\nu_p' = \nu_p$, because it is fixed, the relation

$$\frac{\Delta\nu_a}{\nu_a} = \frac{1-\beta^2}{1-\beta^2\cos^2\theta} - 1 \tag{6.14}$$

is obtained. As approximation for small angles θ and velocity β, this equation can be simplified to [Saa02]

$$\frac{\Delta\nu_a}{\nu_a} \approx -\theta^2\beta^2. \tag{6.15}$$

Because the ions have a small divergence, the line shape is modified even if the mean ion-laser angle is zero. The modified shape can be expressed by

$$f(\nu_a) = 2\int_0^{\pi/2} \frac{1}{\sigma_\theta\sqrt{2\pi}} e^{-\frac{\theta^2}{2\sigma_\theta^2}} \frac{\frac{\gamma_s^2}{4}}{\left(\nu_0^a - \nu_a\frac{1-\beta^2}{1-\beta^2\cos^2\theta}\right)^2 + \frac{\gamma_s^2}{4}} d\theta, \tag{6.16}$$

if the distribution of the angle follows a Gaussian distribution of the width σ_θ around $\theta = 0$. γ_s is the linewidth of the transition, $\nu_0^a = \nu_0^2/\nu_p$ is the resonance frequency of the antiparallel laser without ion beam divergence and ν_a the frequency of the counter-propagating laser beam. The center of the line is always red-shifted so that the measured transition frequency is smaller. Later in the data analysis this is estimated and corrected.

An ion beam that is not electron cooled has a divergence of 2.5 mrad. The line shape will be strongly distorted (s. figure 6.12) and a data analysis with a Lorentzian function would produce a transition frequency being wrong by several MHz. For a successful measurement the ion beam divergence must be small and this is provided by the TSR with its electron cooler. The ion beam divergence of a cooled ion beam is approximately 200 μrad. Using this divergence, the line profile change is so small that a Lorentzian function can be used to describe the line shape (s. figure 6.13). The frequency difference between the real transition frequency and the measured transition frequency is below 50 kHz for $\beta = 0.03$ and below 100 kHz for $\beta = 0.064$.

Gaussian beam All effects discussed so far make the assumption the laser beam is a plane wave, but in reality there exists no plane wave because the power of a plane wave is infinite. In a good approximation the laser beams used in the experiment are Gaussian beams (s. [ST91][Mes99]). The phase ϕ of a Gaussian beam with the frequency ν_l is given by [Mes99]

$$\phi = 2\pi\nu_l t - \frac{2\pi\nu_l}{c}z + \arctan\left(\frac{z}{z_R}\right) - \frac{2\pi\nu_l(x^2+y^2)}{2c}\frac{z}{z^2+z_R^2}, \tag{6.17}$$

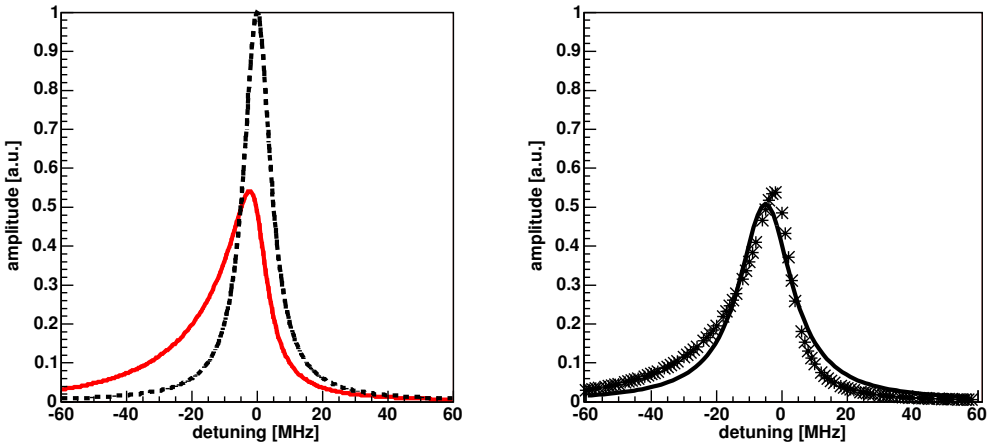

Figure 6.12: Left: The difference between a normal Lorentzian function with a width of 10 MHz (dashed line) is compared with the distorted line shape (solid line), if the ion beam has a divergence of 2.5 mrad. Right: If a Lorentzian function is fitted to this distorted line shape, the peak of the Lorentzian would differ by several MHz from the real transition frequency.

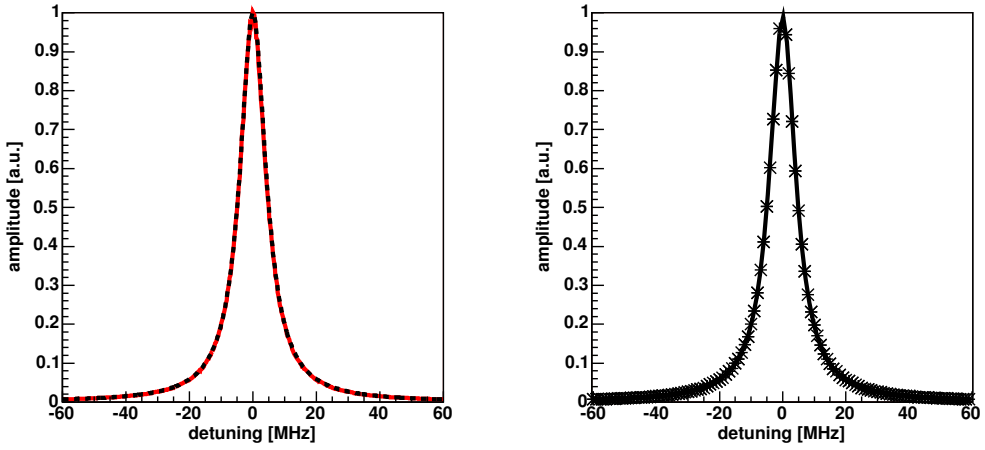

Figure 6.13: Left: The difference between a normal Lorentzian function with a width of 10 MHz (dashed line) is compared with the distorted line shape (solid line), if the ion beam has a divergence of 200 μrad. Right: If a Lorentzian function is fitted on this distorted line shape, the peak of the Lorentzian differs only by few 10th of kHz from the real transition frequency.

where z_R is the so-called Rayleigh range and the focus of the beam is assumed to be at $z = 0$. The difference between a beam of plane waves compared to a Gaussian beam is shown in figure 6.14. The lithium ions with a velocity $\vec{v}$ see the frequency

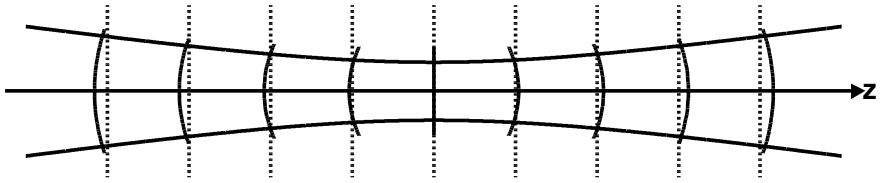

Figure 6.14: Difference between a plane wave (dashed lines) and a Gaussian beam (solid lines).

$\nu' = 1/(2\pi) \cdot d\phi/dt'$ (s. section 2). In the following we describe the direction of the moving ion in the coordinate system described by the laser by two angles Φ_x and Φ_y (s. figure 6.15). Φ_x should be π for the antiparallel or 0 for the parallel laser beam and Φ_y

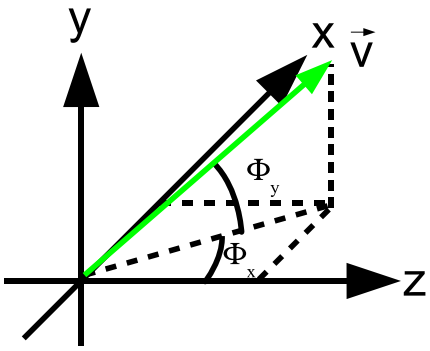

Figure 6.15: The used coordinate system is defined by the direction of the laser beam in z and the angles Φ_x for the horizontal part and Φ_y for the vertical part of the ion velocity.

should be 0. The trajectory of the ion in the laser beam system is

$$\vec{x} = \begin{pmatrix} v_x t + x_0 \\ v_y t + y_0 \\ v_z t + z_0 \end{pmatrix} \quad \text{and } \vec{v} = v \begin{pmatrix} \sin(\Phi_x)\cos(\Phi_y) \\ \sin(\Phi_y) \\ \cos(\Phi_x)\cos(\Phi_y) \end{pmatrix}. \tag{6.18}$$

The total derivative is

$$\nu' = \frac{1}{2\pi}\frac{d\phi}{dt'} = \frac{1}{2\pi}\left(\frac{\partial\phi}{\partial t} + \frac{\partial\phi}{\partial z}\frac{\partial z}{\partial t} + \frac{\partial\phi}{\partial x}\frac{\partial x}{\partial t} + \frac{\partial\phi}{\partial y}\frac{\partial y}{\partial t}\right)\frac{\partial t}{\partial t'}. \tag{6.19}$$

Putting eqs. 6.17 and 6.18 in 6.19 the ions see a frequency

$$\nu' = \underbrace{\gamma\nu_l(1 - \beta\cos(\Phi_x)\cos(\Phi_y))}_{1} + \underbrace{\left(w_0^2 - (x^2+y^2)\frac{z_R^2 - z^2}{z^2 + z_R^2}\right)\frac{\gamma\nu_l\beta}{2(z^2+z_R^2)}\cos(\Phi_x)\cos(\Phi_y)}_{2}$$
$$- \underbrace{\frac{z\gamma\nu_l\beta}{z^2+z_R^2}(x\sin(\Phi_x)\cos(\Phi_y) + y\sin(\Phi_y))}_{3}. \tag{6.20}$$

where w_0 is the beam waist[3] defined by

$$w_0 = \sqrt{\frac{\lambda z_R}{\pi}}.$$

The term number one is the normal frequency shift of the Doppler effect assumes plane waves. The second term is the deviation of the Gaussian beam compared to a plane wave for the part of the motion along z. Because Φ_x is zero or π and Φ_y close to zero in our setup, small uncertainties relative to this angles do not change the sign of the term but it can change the sign if z is smaller or bigger than z_R. The third comes from the change in the distance of the ion to the optical axis. This term has different signs if the ions interact before $(-z)$ or after $(+z)$ the focus of the laser beam. Also the direction of motion regarding to the axis changes the sign of the frequency corrections. In classical saturation spectroscopy this term leads to the phase front broadening (not shift), because in a thermic cloud of gas the same number of particles fly towards the optical axis as well as away. For the typical condition of the present experiment, the second and the third term can reach significant values of several hundred kilohertz. The on-axis terms ($x = y = 0$) can be corrected if the laser beam profile is known, while the off-axis terms ($x \neq 0$, $y \neq 0$) have to be considered in the uncertainty of ν'.

Now the modifications due to the Gaussian beam of the relationship between ν_0 and the laser frequencies ν_a and ν_p are calculated. For the antiparallel laser beam, we find $\cos(\Phi_x) = \cos(180° + \theta_{ax}) = -\cos(\theta_{ax})$ and $\sin(\Phi_x) = \sin(180° + \theta_{ax}) = -\sin(\theta_{ax})$. For the parallel beam we have $\cos(\Phi_x) = \cos(\theta_{px})$ and $\sin(\Phi_x) = \sin(\theta_{px})$. Φ_y is θ_{py} for the parallel beam and θ_{ay} for the antiparallel beam. Because we want to describe the position of the laser beams in a coordinate system defined by the ring and the direction of the ion beam these new angles are introduced here. The z-axis of this coordinate system points along the ion beam, the x-axis is horizontal and the y-axis is vertical orientated with the origin at the position of PM3. The z-axis of the laser based system should coincide with the z-axis of the ion beam based system if all angles are zero and no displacement exist. So, with these definitions, $x_a = -x$, $y_a = y$ and $z_a = z_{a0} - z$ with z_{a0} as laser focus position for the antiparallel beam. $x_p = x$, $y_p = y$ and $z_p = z_{p0} + z$ with z_{p0} as laser focus position for the parallel beam. Now ν' is the transition frequency ν_0 in the rest frame of the ions and ν_l is ν_a for the antiparallel beam and ν_p for the parallel beam in the lab frame. With this modifications eq. 6.20 becomes equal to

$$\begin{aligned}\nu_0 &= \gamma\nu_p(1 - \beta\cos(\theta_{px})\cos(\theta_{py})) + \left(w_0^2 - (x_p^2 + y_p^2)\frac{z_R^2 - (z_p - z_{p0})^2}{(z_p - z_{p0})^2 + z_R^2}\right)\frac{\nu_p\gamma\beta\cos(\theta_{px})\cos(\theta_{py})}{2((z_p - z_{p0})^2 + z_R^2)} \\ &- \frac{(z_p - z_{p0})\nu_p\gamma\beta}{(z_p - z_{p0})^2 + z_R^2}(x_p\sin(\theta_{px})\cos(\theta_{py}) + y_p\sin(\theta_{py})). \qquad (6.21)\end{aligned}$$

[3]The beam waist is the distance to the optical axis if the intensity is reduced by $1/e^2$ compared to the intensity on the optical axis.

for the parallel laser beam and

$$\begin{aligned}\nu_0 &= \gamma\nu_a(1+\beta\cos(\theta_{ax})\cos(\theta_{ay})) - \left(w_0^2 - (x_a^2+y_a^2)\frac{z_R^2-(z_{a0}-z_a)^2}{(z_{a0}-z_a)^2+z_R^2}\right)\frac{\nu_a\gamma\beta\cos(\theta_{ax})\cos(\theta_{ay})}{2((z_{a0}-z_a)^2+z_R^2)} \\ &- \frac{(z_{a0}-z_a)\nu_a\gamma\beta}{(z_{a0}-z_a)^2+z_R^2}(x_a\sin(\theta_{ax})\cos(\theta_{ay}) + y_a\sin(\theta_{ay})) \qquad (6.22)\end{aligned}$$

for the antiparallel laser beam. Because θ_a and θ_p are much smaller than one, the trigonometric functions are expanded to the first non-vanishing order

$$\begin{aligned}\cos(\theta_{ix})\cos(\theta_{iy}) &\approx 1 - \frac{\theta_{ix}^2}{2} - \frac{\theta_{iy}^2}{2} \\ \sin(\theta_{iy}) &\approx \theta_{iy} \\ \sin(\theta_{ix})\cos(\theta_{iy}) &\approx \theta_{ix}\ (i=a,p).\end{aligned}$$

Introducing this approximation in eq. 6.21 and eq. 6.22 and neglecting terms, which are multiplied by the square of the angles except for the angle dependence of the Doppler shift, the result is

$$\begin{aligned}\nu_0 &= \gamma\nu_p(1-\beta) + \underbrace{w_0^2\frac{\nu_p\gamma\beta}{2((z_p-z_{p0})^2+z_R^2)}}_{\phi_{corr,p}} \qquad (6.23) \\ &+ \underbrace{\gamma\left(\nu_p\beta\frac{\theta_{px}^2+\theta_{py}^2}{2} - \frac{(x_p^2+y_p^2)(z_R^2-(z_p-z_{p0})^2)\nu_p\beta}{2((z_p-z_{p0})^2+z_R^2)^2} - \frac{(z_p-z_{p0})\nu_p\beta}{(z_p-z_{p0})^2+z_R^2}(x_p\theta_{px}+y_p\theta_{py})\right)}_{\phi_{uncorr,p}}.\end{aligned}$$

and

$$\begin{aligned}\nu_0 &= \gamma\nu_a(1+\beta) - \underbrace{w_0^2\frac{\nu_a\gamma\beta}{2((z_{a0}-z_a)^2+z_R^2)}}_{\phi_{corr,a}} \qquad (6.24) \\ &- \underbrace{\gamma\left(\nu_a\beta\frac{\theta_{ax}^2+\theta_{ay}^2}{2} - \frac{(x_a^2+y_a^2)(z_R^2-(z_{a0}-z_a)^2)\nu_a\beta}{2((z_{a0}-z_a)^2+z_R^2)^2} + \frac{(z_{a0}-z_a)\nu_a\beta}{(z_{a0}-z_a)^2+z_R^2}(x_a\theta_{ax}+y_a\theta_{ay})\right)}_{\phi_{uncorr,a}}.\end{aligned}$$

$\phi_{corr,i}$ is the on-axis term, that describes the modifications, which can be corrected, if the Gaussian beam profile is known. $\phi_{uncorr,i}$ includes terms due to uncertainties of the alignment of the angles and the displacement from the axes. Multiplying both equations the result is very close to the formula obtained by using plane waves

$$(\nu_0 + \phi_{corr,a} + \phi_{uncorr,a})(\nu_0 - \phi_{corr,p} - \phi_{uncorr,p}) = \nu_a\nu_p. \qquad (6.25)$$

Dropping all terms that merely consist of corrections, this is simplified to

$$\nu_0^2 + \nu_0(\underbrace{\phi_{corr,a} - \phi_{corr,p}}_{b_{corr}} + \underbrace{\phi_{uncorr,a} - \phi_{uncorr,p}}_{b_{uncorr}}) = \nu_a\nu_p. \qquad (6.26)$$

By neglecting terms quadratic in b_{corr} and b_{uncorr}, ν_0 can be calculated as

$$\nu_0 = -\frac{b_{corr}+b_{uncorr}}{2} + \sqrt{\nu_a\nu_p}. \qquad (6.27)$$

Chapter 7

Results

The first part of this chapter gives an overview over the quality of the alignment between the laser and ion beams, geometrically as well as energetically. A detailed investigation of the corresponding uncertainties is already given in [Saa02]. The next subsection shows how well the correction of the phase-front corrections works. The effects of laser power and magnetic fields on the lithium-ion spectroscopy are discussed. After this the results of the frequency measurements at $\beta = 0.03$ and $\beta = 0.064$ are presented followed by the determination of $\hat{\alpha}$ and ν_0.

7.1 Properties of the ion beam

$\beta = 0.03$: In the data analysis of the frequency measurements only data are considered, that are taken after the electron cooled ion beam has reached its equilibrium. Figure 7.1 shows the shape of the electron cooled ion beam for $\beta = 0.03$ in horizontal and vertical direction as measured with the beam profile monitor. The fit function is a sum of two Gaussian functions, one describes the shape of the cooled beam and the other describes the residual hot ions. The intensity of this hot contribution is $< 10\%$ of the total beam intensity. The fitted values σ_{mx} and σ_{my} must be corrected by the limited resolution of the BPM (s. section 4.2.2). The real ion beam size of the cooled ions in horizontal direction is $\sigma_x = \sqrt{\sigma_{mx}^2 - \sigma_{resx}^2} = 0.62$ mm and in vertical direction is $\sigma_y = \sqrt{\sigma_{my}^2 - \sigma_{resy}^2} = 0.40$ mm. The cooled beam has an emittance of $\epsilon_x = 8.30 \cdot 10^{-8}$ m·rad for the horizontal axis and $\epsilon_x = 5.06 \cdot 10^{-8}$ m·rad for the vertical axis. Now the beam envelope and beam divergence is calculated using eq. 4.5 and eq. 4.6. In figure 7.2 the values of the beam envelope and beam divergence are given. At the three photomultiplier positions the beam size are (the uncertainty for all ion beam size measurements is 50 μm)

	PM1	PM2	PM3
horizontal σ_x [mm]	0.69	0.70	0.68
vertical σ_y [mm]	0.35	0.39	0.33

The ion beam divergence is 120 μrad in the horizontal axis and 160 μrad in the vertical axis, so a total divergence of 200 μrad is obtained. The redshift of the line due to the ion beam divergence is in the range of (25 ± 25) kHz.

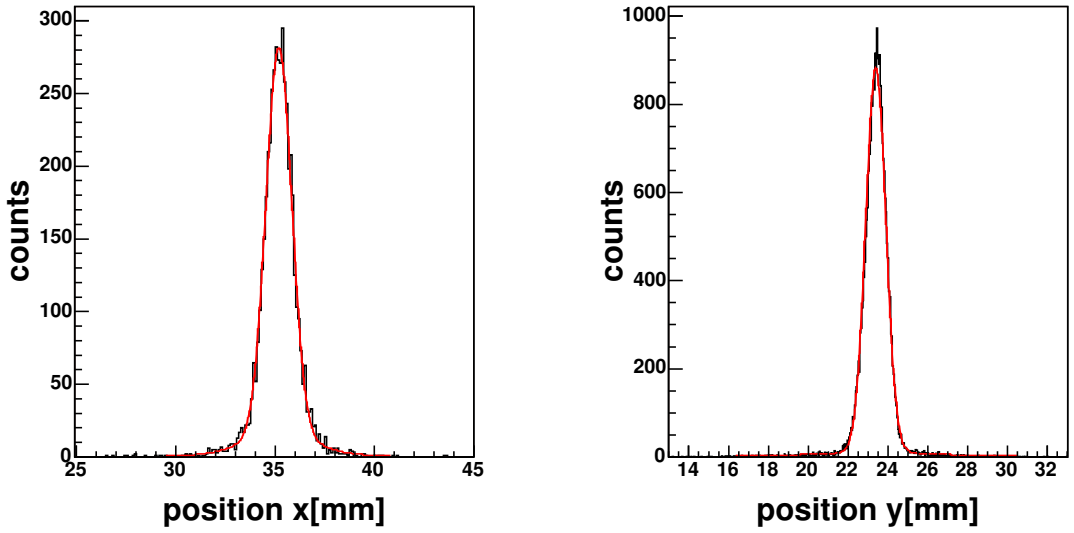

Figure 7.1: The ion beam after 10 s electron cooling at $\beta = 0.03$. The widths are $\sigma_{mx} = 0.65$ mm for the horizontal component and $\sigma_{my} = 0.50$ mm for the vertical part as deduced from a fit of a Gaussian to the measured profile.

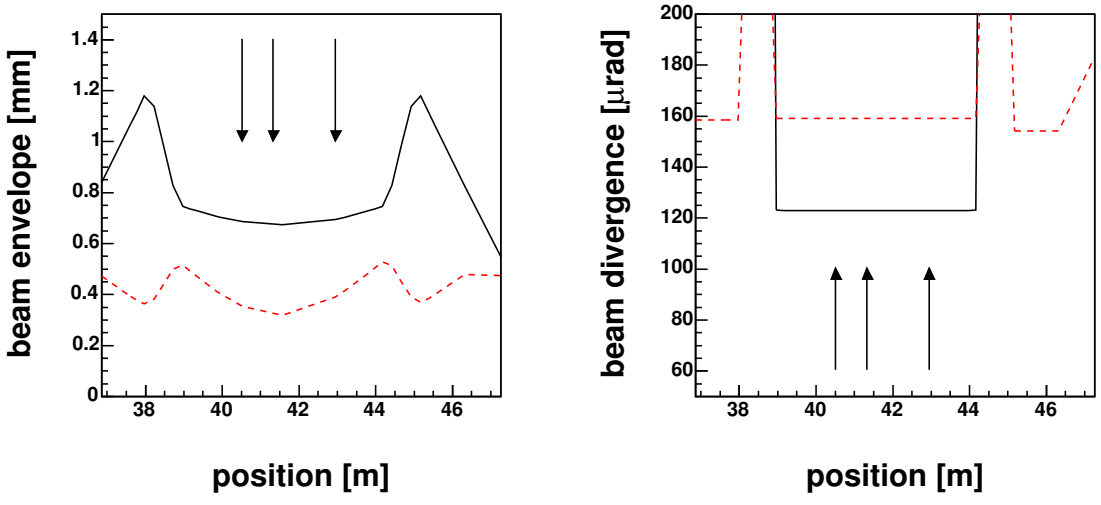

Figure 7.2: The ion beam in the experimental section after 10 s of electron cooling at $\beta = 0.03$. The solid line is the horizontal axis and the dashed line is the vertical axis. The arrows indicate the positions of PM1, PM3 and PM2 (from left to right).

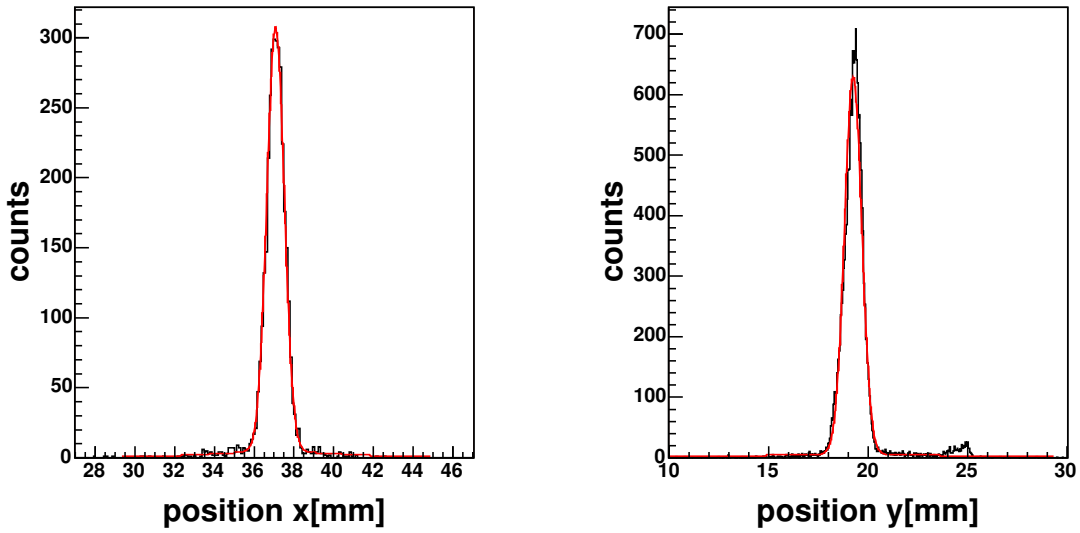

Figure 7.3: The ion beam after 10 s of electron cooling at $\beta = 0.064$. The width $\sigma_{mx} = 0.44$ mm for the horizontal component and $\sigma_{my} = 0.43$ mm for the vertical part. The secondary peak in the vertical measurement is an electronic artefact [Gri].

$\beta = 0.064$**:** The resolution corrected beam size at the BPM is $\sigma_x = 0.39$ mm in horizontal direction and $\sigma_y = 0.30$ mm in vertical direction (s. figure 7.3). The corresponding emittances are $\epsilon_x = 3.33 \cdot 10^{-8}$ m·rad and $\epsilon_y = 3.00 \cdot 10^{-8}$ m·rad. In figure 7.4, the values of the beam envelope and beam divergence are given. At the photomultipliers the beam sizes are

	PM1	PM2	PM3
horizontal σ_x [mm]	0.43	0.44	0.43
vertical σ_y [mm]	0.27	0.30	0.25

The ion beam divergence is 80 μrad in the horizontal axis and 120 μrad in the vertical axis, so a total divergence of 150 μrad is obtained. The frequency redshift due to the ion beam divergence is in the range of (50 ± 50) kHz. At both velocities the ion beam diameter is smaller than the laser beam sizes used for the lithium ion spectroscopy.

7.2 Geometrical and energetic alignment

7.2.1 Geometrical alignment

The geometrical alignment is carried out as mentioned in section 6.2. In figure 7.5 an overlap-scan is shown after optimization. With this method, a maximum uncertainty of the angle between the parallel laser- and ion-beam of 50 μrad per axis is obtained. The total angular uncertainty is thus 73 μrad. The alignment between the antiparallel and parallel laser-beam is optimized by overlapping the reflected beam with the incoming beam with the help of an aperture placed close to the tower. The overall uncertainty of this alignment is 0.5 mm over a distance of 14 m, which gives an angular uncertainty of

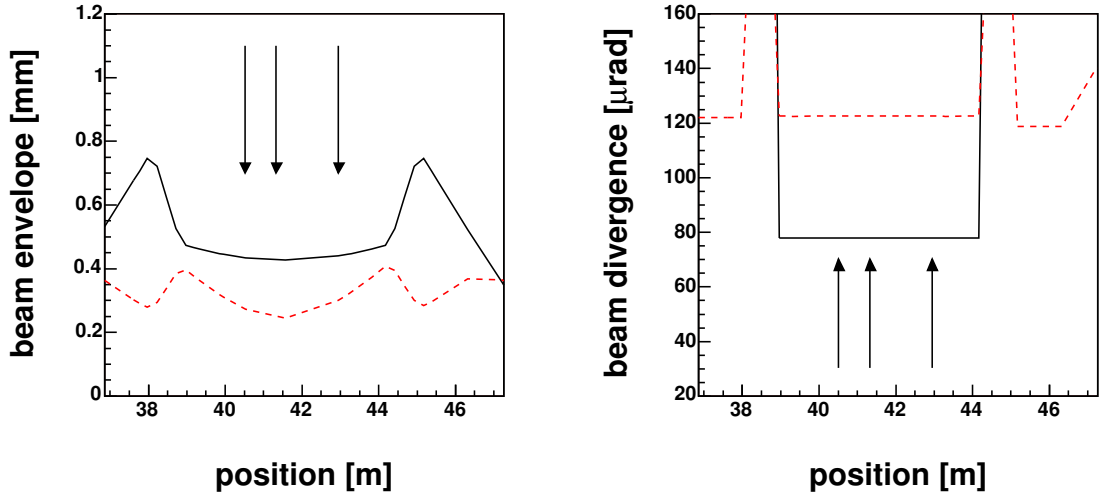

Figure 7.4: The ion beam after 10 s of electron cooling at $\beta = 0.064$. The solid line is the horizontal axis and the dashed line is the vertical axis. The arrows indicates the positions of PM1, PM3 and PM2.

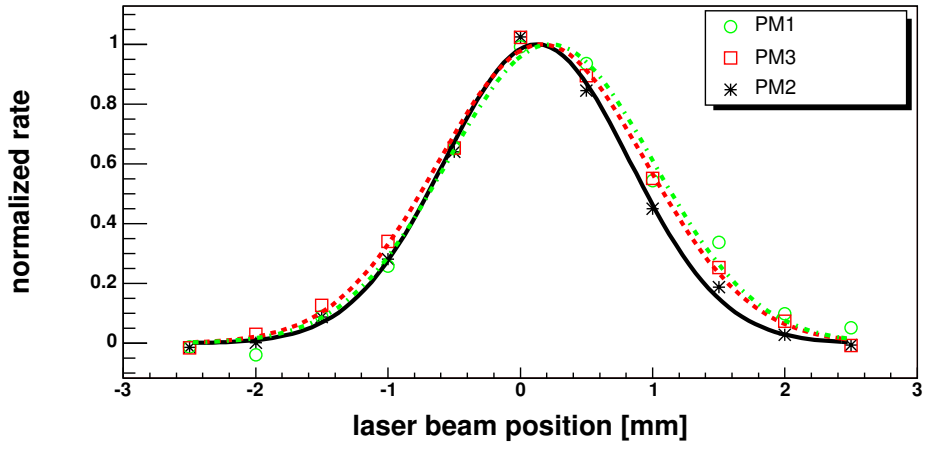

Figure 7.5: Optimized overlap between parallel laser- and ion-beam ($\beta = 0.03$)

36 μrad per axis and overall of 51 μrad. The alignment is sufficient to send the reflected laser-beam back to the laser setup through the optical fiber as shown in 7.6. The reflected

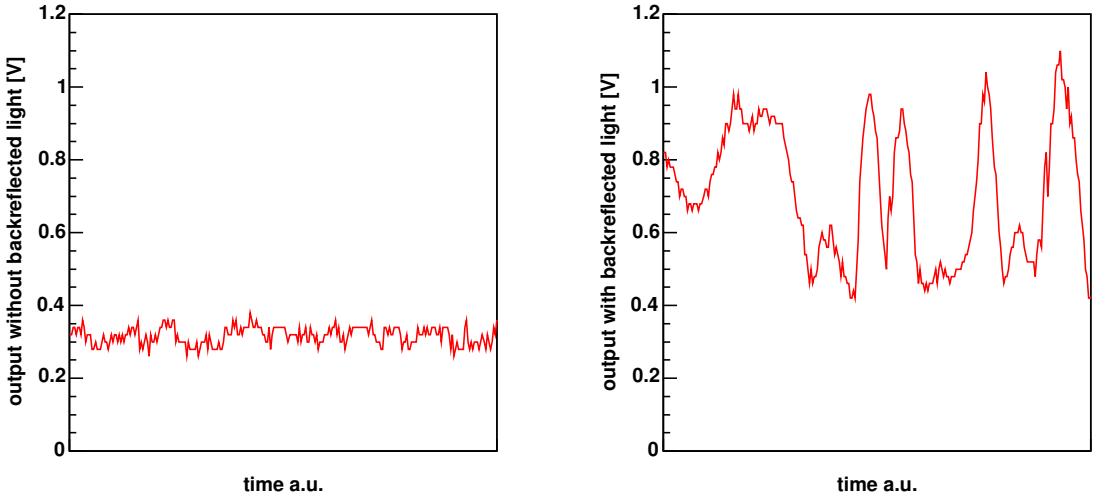

Figure 7.6: A beam-splitter is placed in front of the fiber holder on the optical table and the reflected light is detected by a photodiode. In the left picture the photodiode signal is shown if the laser-beam is blocked at the TSR. Only the stable reflected light from the surface of the fiber is detected, because the fiber has no anti-reflection coating. The right picture shows the signal, if the light is reflected back into the fiber. The reflected beam now interferes with the back-reflected light.

beam has thus a angular uncertainty to the ion-beam, due to error propagation, of 89 μrad.

The radial displacement uncertainty between the laser beam and the ion beam is estimated to be 150 μm per axis in total 212 μm for the parallel laser. Because the distance between the back-reflecting mirror and PM3[1] is 8 m, the radial displacement of the reflected beam due to the angle uncertainty of 51 μrad between the laser beams increases by 408 μm. The radial displacement for the back-reflected beam has an uncertainty of $\sqrt{212^2 + 408^2}$ μm = 460 μm. This angular and radial uncertainties lead to frequency shifts of the measured transition. These shifts are taken into account in the discussion of the phase-structure of the laser beam and are treated in detail in section 7.4.

7.2.2 Energetic alignment

The energetic alignment is checked by a frequency scan over the whole velocity distribution of the ions, which is done by the antiparallel dye laser. An example of such a measurement is shown in figure 7.7. The peak of the velocity distribution is placed at

[1]For the estimation of the uncertainties the position of PM3 is used, because this photomultiplier is used mainly for the lithium spectroscopy.

the frequency, where the saturation signal occurs. The measured linewidth is (2584±61) MHz which is equal to a standard deviation[2] of (1097 ± 26) MHz. With equation 4.8 a momentum spread of about $6.7 \cdot 10^{-5}$ at $\beta = 0.03$ can be given. At $\beta = 0.064$ the frequency width is from the same size. The measured Doppler width is equal to a (longitudinal) temperature of 324 K for the stored lithium ion.

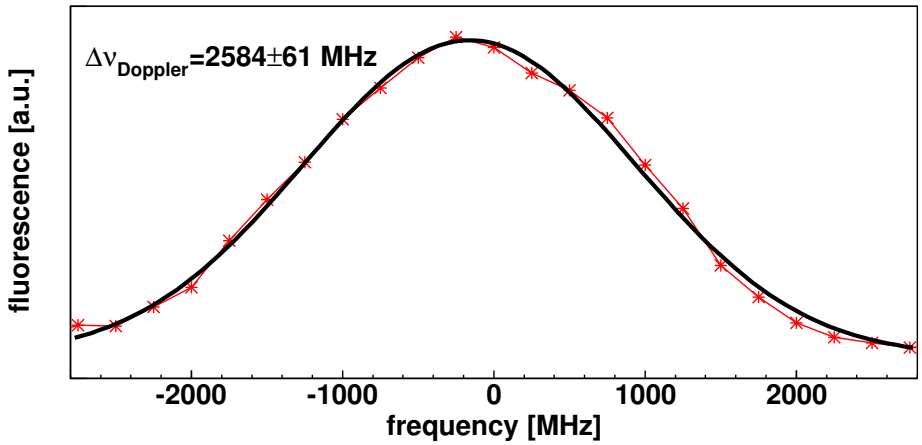

Figure 7.7: The Doppler broadened fluorescence spectrum of an electron cooled $^7Li^+$ beam. The solid line is a Gaussian fit, which gives a FWHM width of 2584 ± 61 MHz ($\beta = 0.03$).

The influence of an AC-Stark shift, which originates from the interaction between the ion and the electric field of the light, was investigated by G. Saathoff [Saa02]. Based on the theoretical work of [BL75] the frequency dependence of the AC-Stark shift on laser intensity in the rest frame of the ion beam is

$$\Delta\nu_{AC} \propto I_0 \frac{\nu_0 - \nu_L}{(\nu_0 - \nu_L)^2 + \left(\frac{\gamma}{2\pi}\right)^2}. \tag{7.1}$$

I_0 is the laser intensity, ν_0 the transition frequency and ν_L is the laser frequency in the rest frame of the ion beam. The AC-Stark shift should vanish, if the laser talks to the ions at the maximum of the velocity distribution, because then the number of ions at lower and higher velocity are equal and the AC-Stark shift would produce a line broadening and not a shift. The bunching of the ion beam stabilizes the ion beam velocity to avoid shifts of the velocity distribution away from this configuration. The energetic alignment is done on the same way as in [Saa02]. The frequency uncertainty due to the AC-Stark shift is rather small and by extrapolation to zero laser intensity any residual AC-Stark shift should vanishes.

In [Saa02] there is a discussion about instabilities of the unbunched ion beam with a frequency of 2 Hz caused by the electron cooler. These instabilities are observed until

[2]The linewidth is given as FWHM. To obtain the standard deviation of a Gaussian distribution this is multiplied by $1/(2\sqrt{2\ln 2})$.

the measurements of March 2004. Investigations show that the instabilities are related to the time of injection. In the measurements of 2005 these instabilities have vanished. Their cause remains unclear [Gri].

7.3 Line profile of the lithium ion transition

The line profile can be very complex in detail but only two effects are considered in this experiment. The first one is a possible time of flight broadening and the second one is the saturation broadening.

7.3.1 Fundamental line analysis

To obtain the Lorentzian shaped saturation signal the measured signals are analyzed as follows. The measured data points of the several frequency scans of one measurement are binned according to the measured heterodyne frequency and averaged. The bin width is the frequency step-width of the frequency scan. The center of a bin is the mean value of the related heterodyne frequencies. As explained in the section 6.3.3, the signals recorded when only one laser interacts with the ions alone are added and this sum is subtracted from the signal when both lasers interact with the ions simultaneously. This difference is a Doppler free saturation signal without background. Examples for both velocities are shown in figure 7.8 for $\beta = 0.03$ and 7.9 for $\beta = 0.064$ as function of the measured heterodyne frequency between the two dye lasers. As shown in section 6.3.2 the change of the frequency of the antiparallel laser $\Delta\nu_a$ indicated by the change of the heterodyne frequency between the two dye lasers is connected to the frequency change $\Delta\nu$ for the lithium ion spectroscopy via $\Delta\nu = \frac{\nu_0}{2\nu_a}\Delta\nu_a$.

7.3.2 Time of flight broadening

In section 6.3.3 the theory is given that is used for the data analysis. Experimentally, the time of flight effect is investigated by comparing the linewidths measured at the different positions of the photomultipliers at the same intensity. A few measurements at $\beta = 0.064$ were done, where the setup, that is normally placed at PM3, was placed at the position of PM1 for the measurement of the saturation signal. The results are given in figure 7.10. The linewidth measured with PM2 shows the expected behavior for saturation broadening that is discussed in the next section. The given saturation intensity is not compared to the value given in chapter 3, because the fluorescence signal is generated over several meters as discussed in section 6.3.1 and the laser intensity is not constant over this distance. At the position of PM1 and PM3 however the linewidths are approximately independent of the intensity below 20 mW/cm^2. The lines in figure 7.10 represents the mean value of all data points within this region.

This behavior was already observed for PM3 in the work of G. Saathoff [Saa02][3] with the same limit of approximately 9.6 MHz. Because the present setup does not employ

[3]Here the linewidth $\Delta\nu_a$ is given in frequency of the scanning dye laser that is related to the real linewidth $\Delta\nu_0$ used here by $\Delta\nu_0 = \Delta\nu_a\nu_0/(2\nu_a)$.

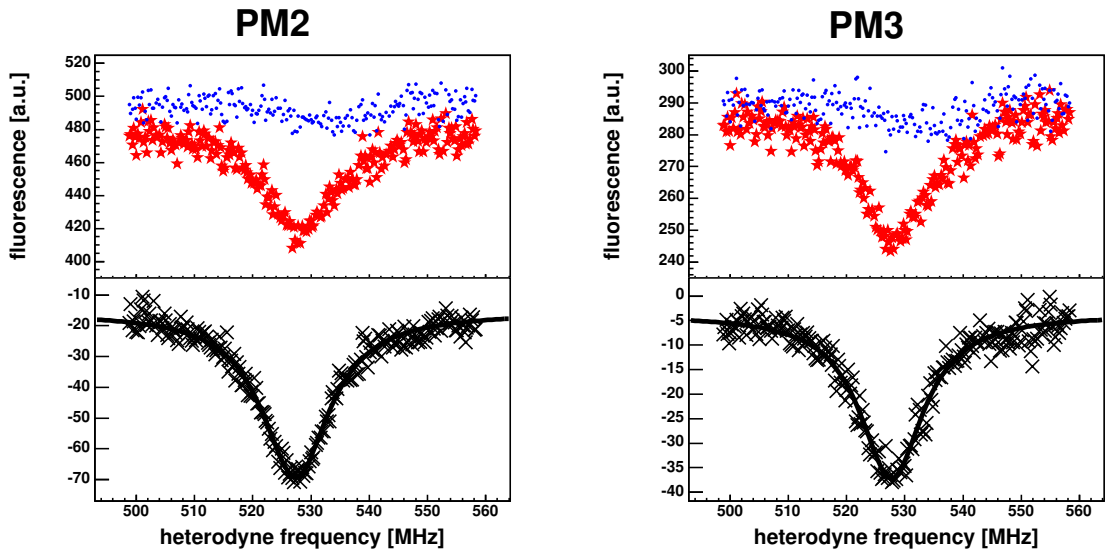

Figure 7.8: The fluorescence signals obtained at $\beta = 0.03$ as a function of the heterodyne frequency of the two dye lasers. The upper trace is the sum of the signals that are measured, if only one laser interacts with the ions. The middle trace is the saturation signal. And the lower graph shows the difference of the two others.

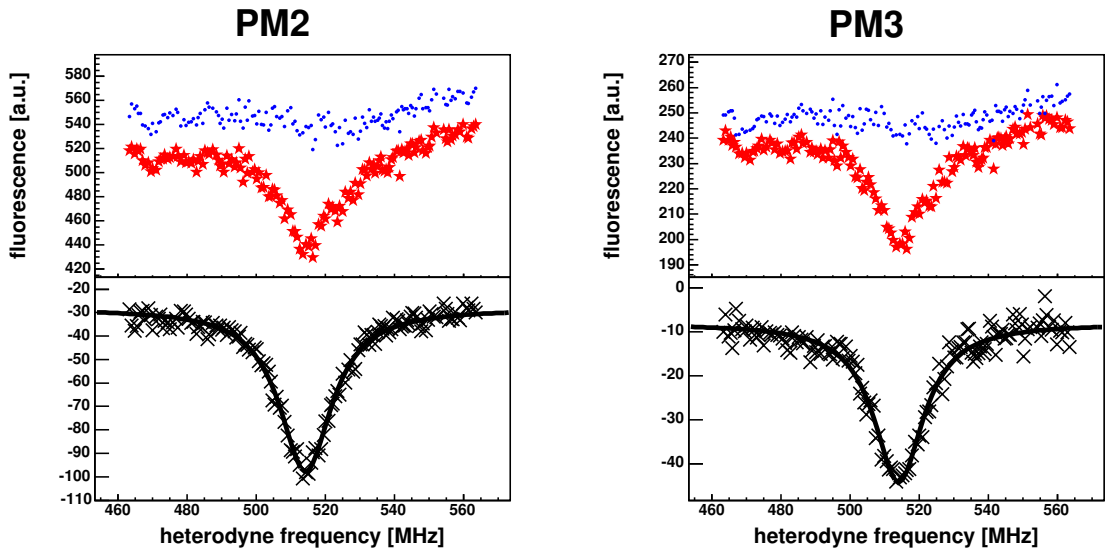

Figure 7.9: The signals obtained at $\beta = 0.064$.

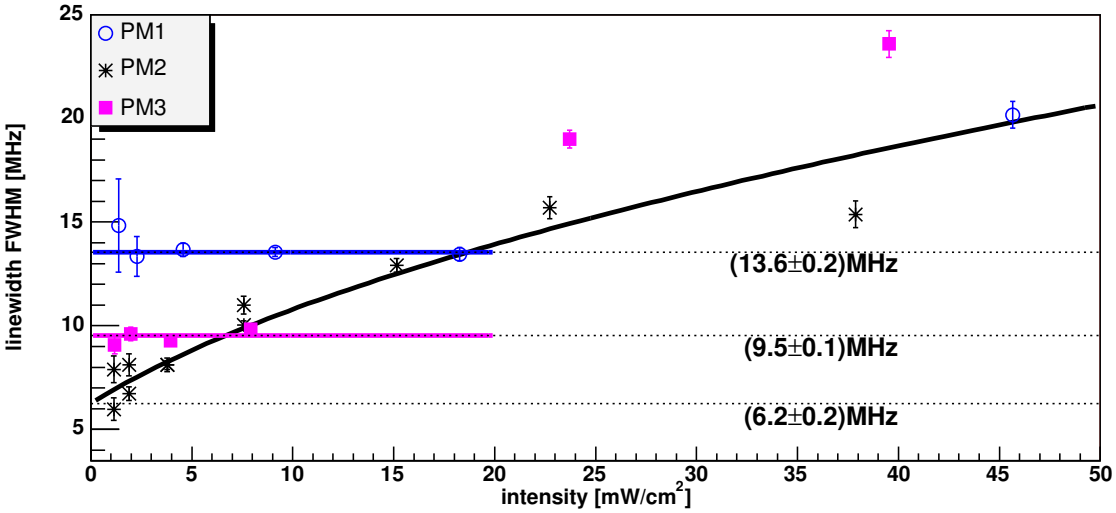

Figure 7.10: Measured linewidth of the transition as function of laser intensity for the three positions of the photomultipliers at $\beta = 0.064$. From the width of PM2 a saturation intensity of (5.0 ± 0.6) mW/cm^2 is obtained.

the direct wavelength modulation of the lasers which broadens the laser linewidth, the linewidths are expected to be smaller as in [Saa02]. The linewidth must therefore be affected by an effect that is independent of the intensity. One effect can be the limited transition time of the ion through the laser field. Taking the values at zero intensity, where the influence of saturation broadening should be negligible, a possible influence of transition time can be investigated. In figure 7.11, this is done as a function of the flight time. Two functions are fitted to the data: The first functions represents the linewidth evaluated by a numerical calculation using equation 6.11. The second function takes a formula, that describes the linewidth by a Voigt profile [Dra66], that is a convolution of a Gauss and Lorentz profile. The width of the Gaussian contribution of the Voigt profile is given by the laser-width due to the time of flight effect modified by a factor $n\ 5.6n/(2\pi(t - t_{entry}))$, that describes possible deviation between the Voigt profile and the measurement. The general form of the function is

$$\Delta\nu_{Voigt} = \sqrt{\left(\frac{5.6n}{2\pi(t - t_{entry})}\right)^2 + \frac{\Delta\nu_{Lorentz}^2}{4}} + \frac{\Delta\nu_{Lorentz}}{2}, \tag{7.2}$$

where t_{entry} is the time the ion sees the laser field before it reaches the Position of PM1. $\Delta\nu_{Lorentz}$ is the FWHM of the homogenous linewidth, that should be observed, if no time of flight effect is present. n is a scale factor and should be 1, if the observed linewidth can be described by a Voigt profile. The parameters for the solid line are (s. figure 7.11)

$$\begin{aligned} t_{entry} &= (0.074 \pm 0.001)\mu\text{s} \\ \Delta\nu_{Lorentz} &= (3.5 \pm 0.2)\text{MHz}. \end{aligned}$$

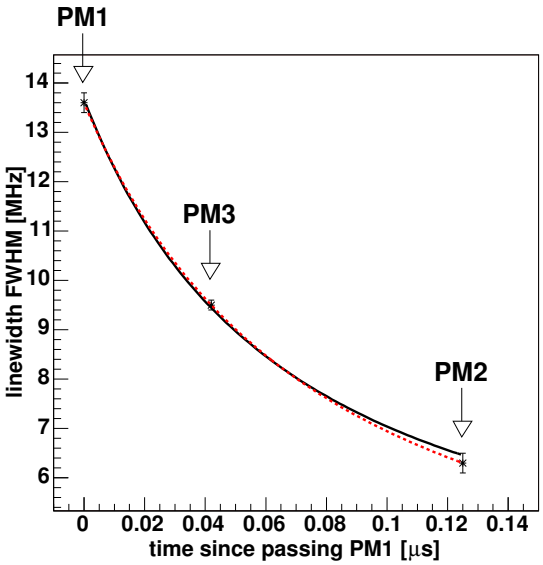

Figure 7.11: Measured linewidth limits (s. figure 7.10) of the transition for the three positions of the photomultipliers. The solid line is obtained, when equation 6.11 is fitted, and the dashed line is obtained for a Voigt-like profile.

$\Delta\nu_{Lorentz}$ is in the range of the uncertainty equal to the natural linewidth of 3.7 MHz. The time t_{entry} corresponds to a flight length of 1.4 m which means that the ions start to see the light field, when they are at the end of the last quadrupole magnets in front of the experimental section. The dashed line in figure 7.11 is obtained, if a Voigt like linewidth is used. The parameters are

$$\begin{aligned} n &= 1.3 \pm 0.2 \\ t_{entry} &= (0.09 \pm 0.01)\mu\text{s} \\ \Delta\nu_{Lorentz} &= (3.1 \pm 1.1)\text{MHz}. \end{aligned}$$

The flight path of the ions before PM1 is now found to be slightly larger but still consistent with the former value. The Lorentzian linewidth of (3.1 ± 1.1) MHz is in agreement with the natural linewidth. n is not so far away from one, so the linewidth can be calculated like the linewidth of a Voigt profile. The description by a time of flight effect can explain the limits in the measured linewidths. For low velocity $\beta = 0.03$ the time of flight effect plays only a small role and no further investigation is done.

The behavior of the linewidth for different laser intensities and photomultiplier positions shown in figure 7.10 is not fully understood, because it is not possible to describe the laser intensity insensitivity of the linewidth at PM3 or PM1 up to moderate laser intensities with the given models.

7.3.3 Saturation broadening

As mentioned in the theoretical part of the lithium ion spectroscopy in section 6.3.3, the linewidth should show a power dependence[4], that follows the law

$$\Delta\nu_{Lorentz}(P) \quad = \quad \gamma_0\sqrt{1+\frac{P}{P_0}}. \tag{7.3}$$

γ_0 is the FWHM without saturation broadening and P_0 is the saturation power.

$\beta = 0.03$**:** The widths observed in the measurements, that are also used for the transition frequency determination are plotted in figure 7.12. The time of flight effect is not included in the data analysis, because it is not fully understood and, for the low ion velocity, no detailed measurements on this topic are done. The measured FWHM show

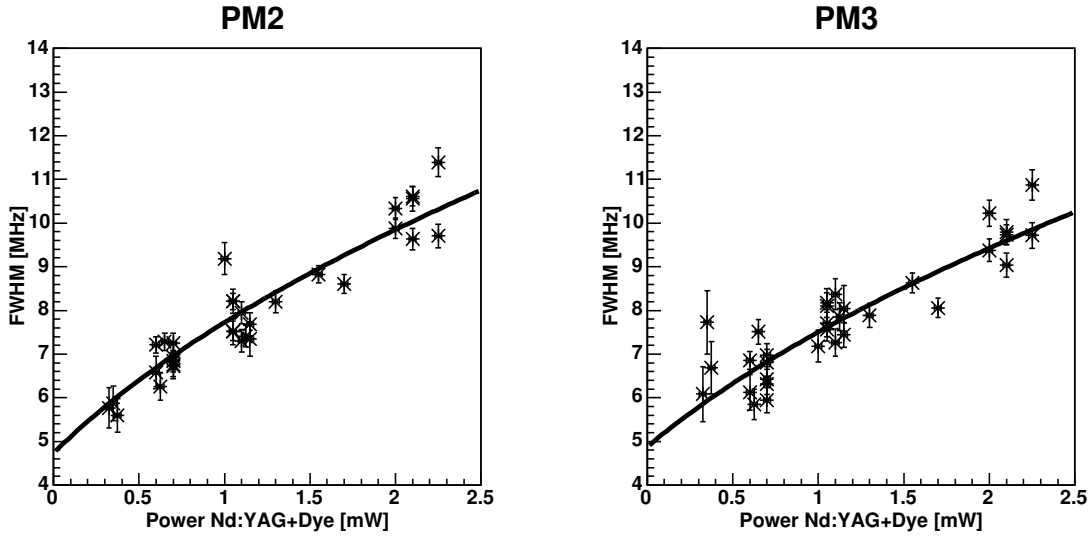

Figure 7.12: The FWHM as a function of the total laser power ($\beta = 0.03$).

the expected behavior. The values obtained from a fit to the data are

	PM2	PM3
γ_0 [MHz]	4.7 ± 0.2	4.9 ± 0.2
P_0 [mW]	0.60 ± 0.07	0.73 ± 0.09

Compared to the natural linewidth of 3.7 MHz the measured values are about 1 MHz broader, but this may be due to the other line broadening mechanisms like residual time of flight effects and frequency widths of the lasers.

[4]All given laser powers a related to laser powers in the laboratory frame and are not transformed into the ion frame[McK79]. Normally the total laser power is given as sum $P_f + aP_t$ of the laser power from the fixed frequency laser P_f and from the tuned laser P_t that is scaled to the laser power of the fixed frequency laser. The scaling factor a is obtained by comparing the single laser powers if each single laser produces the same fluorescence rate.

$\beta = 0.064$**:** The same procedure is also carried out for the high velocity measurements (s. figure 7.13). For the points measured with PM2, the expected saturation behavior

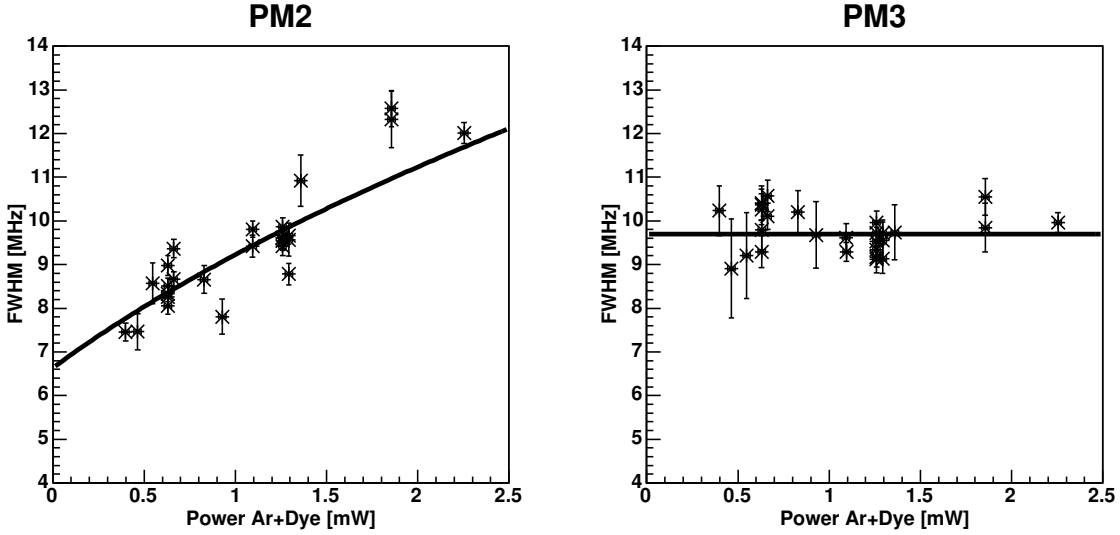

Figure 7.13: The FWHM as a function of the total laser power ($\beta = 0.064$).

is observed. For the PM3 measurements the values are all equal, because the power is not large enough to dominate the line broadening. The FWHM of γ_0 at PM2 has a value of 6.6 ± 0.2 MHz. The saturation power is 1.1 ± 0.1 mW. No values can be derived for PM3. At high velocity the broadening of the line due to saturation is not so good described by 7.3 as at low velocity, perhaps the variation of the laser power over the flight length of three lifetimes is too big and the time of flight effect is also significant.

7.4 Phasefront correction

As discussed in section 6.3.4, the Gaussian phase structure of the laser beams can lead to a frequency shift for moving ions. In order to estimate and correct this effect, the laser beam profile needs to be known. It is measured by three different methods. A commercial beam profile measurement device (Type Omega meter WM100 from Thorlabs) is used outside the ring that measures the beam radius in one dimension. The beam radius measured with this device has a small uncertainty of 0.05 mm to 0.1 mm. Also with a CCD-camera, the beam profile can be recorded and analyzed. This method is used only a few times. The advantage is that with one recorded beam profile several informations are available like the beam shape and beam power. The third method uses the signal obtained from the overlap scans between laser beam and ion beam, because, if the ion beam radius σ_{ion} is known, the laser radius ω_l[5] can be calculated from the

[5]The laser beam radius is the distance to the optical axis if the intensity is reduced by $1/e^2$ compared to the intensity on the optical axis.

fitted width σ_{ms} of the Gaussian shape of the overlap-scan

$$\omega_l = 2\sqrt{\sigma_{ms}^2 - \sigma_{ion}^2}. \tag{7.4}$$

7.4.1 Phasefront correction at $\beta = 0.03$

Measurement 1. (date: 21.02.2005-28.02.2005) Figure 7.14 shows the laser beam radius at different positions along the beam. The lines are the fitted functions that describe the expected evolution of the laser beam radius ω as a function of the distance to the focus of the laser beam

$$\omega = \omega_0\sqrt{1 + \frac{z}{z_R}}. \tag{7.5}$$

ω_0 is the beam radius at the focus. For the profile measurement of the dye laser no overlap-scan is used, because the background is too unstable due to the scattering light from the dye laser, which travels two times through the ring. The problems comes from the fact, that the laser frequencies (532 nm and 565 nm) and the transition frequency (548 nm) are relative close in wavelength. The values of $\phi_{corr,a}$ and $\phi_{corr,p}$ (s. section 6.3.4) obtained by a Monte Carlo simulation (already used and explained in [Saa02]) for the different positions of PM2 and PM3 are given in the following table.

	PM2 [kHz]	PM3 [kHz]
$\phi_{corr,a}$	77 ± 50	59 ± 50
$\phi_{corr,p}$	137 ± 50	98 ± 50
b_{corr}	-60 ± 71	-39 ± 71

The simulation takes an ensemble of ions, that travels collinear to the laser beam so only term 2 in equation 6.20 is respected. The frequency shift due to the ion beam divergence is calculated by the approximation eq. 6.15. The angles between the ion beam and the laser beam have a Gaussian distribution. It takes also into account the dynamic feature of the spectroscopy (s. section 6.3.1). Also the values for b_{uncorr} can be estimated[6]. To estimate the uncertainty for a single measurement, b_{uncorr} is calculated in the range of the geometrical uncertainties for a given axis (s. figure 7.15). ϕ_p is the angle between the parallel beam and the ions. ϕ_{rel} is the angle between the two laser beams, which is connected to ϕ_a by $\phi_a = \phi_p + \phi_{rel}$ for each axis. The radial displacement of the antiparallel beam is connected to the radial displacement of the parallel beam by $x_a = x_p - \phi_{rel} z$, where z is the distance between the back-reflecting mirror to the desired place in the ring[7]. For every possible combination the value of b_{uncorr} is calculated. The lines show the limits given by the alignment uncertainty. The extreme values within the limits are used for b_{uncorr}. For the possible angle and radial displacement uncertainties, the uncertainty for a single measurement is between -40 and 120 kHz for each axis. The total uncertainty is -60 kHz and 170 kHz. A mean value of b_{uncorr}[8] is estimated to be

[6] As mentioned earlier, a simulation is not possible, because b_{uncorr} describes frequency shifts due to the uncertainty of the geometrical alignment and this can change from measurement to measurement.

[7] In this experiment the distance between the back-reflecting mirror and the position of PM3 is 8 m.

[8] In this uncertainty all angle uncertainties like the angle between lasers and ions are included.

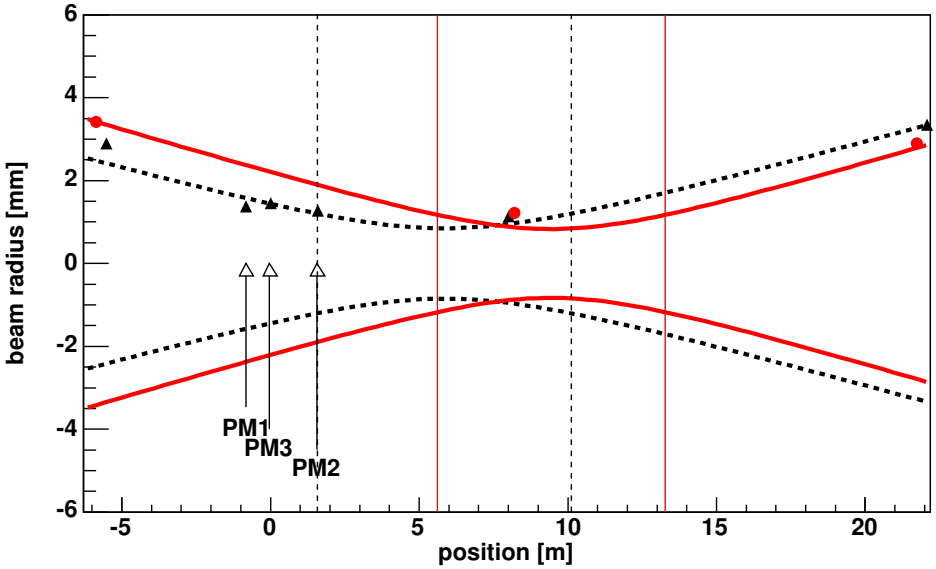

Figure 7.14: Position and profile of the Gaussian laser beams during the measurement 1 at $\beta = 0.03$. The solid line is the profile for the counter-propagating dye laser ($\omega_0^{dye} = (0.81 \pm 0.02)$ mm is the laser radius of the focus, $z_0^{dye} = (9.4 \pm 0.4)$ m is the position of the focus, $z_R^{dye} = (3.8 \pm 0.2)$ m is the Rayleigh range) and the dashed line is the profile for the co-propagating Nd:YAG laser ($\omega_0^{Nd} = (0.85 \pm 0.03)$ mm, $z_0^{Nd} = (5.8 \pm 0.4)$ m, $z_R^{Nd} = (4.3 \pm 0.3)$ m). The vertical lines indicate the Rayleigh range.

smaller than 50 kHz by calculating a mean value of all possible b_{uncorr} values given in figure 7.14.

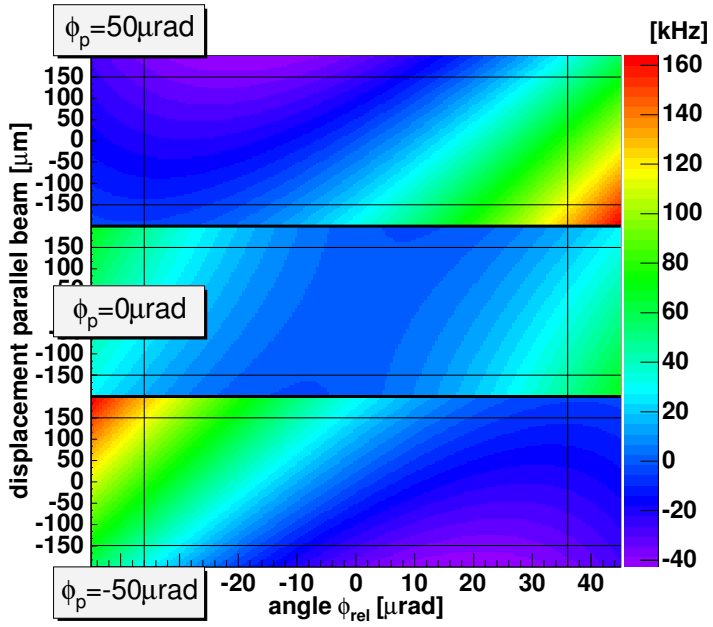

Figure 7.15: Estimation of the frequency uncertainty b_{uncorr} introduced by the Gaussian phase contribution at PM3. Three cases of the geometrical alignment are considered. $\phi_{uncorr,p}$ is calculated at the position z_{50} (50 percent of the signal for PM3 is produced between z_{50} and $z = 0$) for three different angles ϕ_p between the parallel laser beam and ion beam. For these three angles the radial displacement of the parallel beam is changed as well as the possible values for the angle of the antiparallel beam and $\phi_{uncorr,a}$ is calculated at the position z_{50} ($\beta = 0.03$).

Measurement 2. (date: 07.02.2005-14.02.2005) A second beamtime with less statistics is also available. The beam profile of the laser is illustrated in figure 7.16. The values for b_{uncorr} are equal to the values for the first measurement. The values for $\phi_{corr,a}$ and $\phi_{corr,p}$ are given in the next table.

	PM2 [kHz]	PM3 [kHz]
$\phi_{corr,a}$	56 ± 50	45 ± 50
$\phi_{corr,p}$	204 ± 50	121 ± 50
b_{corr}	-148 ± 71	-76 ± 71

7.4.2 Phasefront correction at $\beta = 0.064$

Here all three photomultiplier signals are used for the co- as for the counter-propagating beam. Because β is higher, the sensitivity to frequency shifts due to curved phasefronts is higher. The values for the co-propagating beam and for the counter-propagating beam are given in the following table.

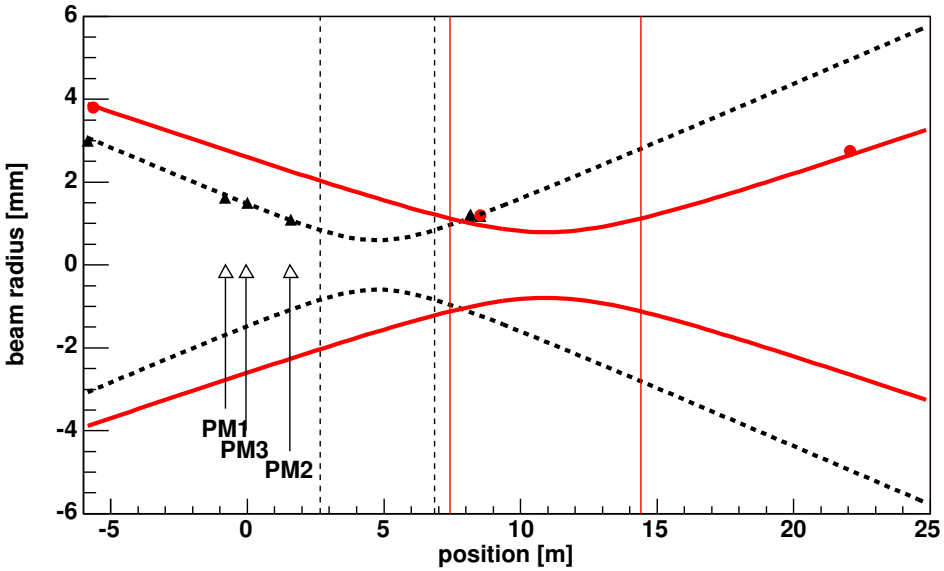

Figure 7.16: Position of the Gaussian laser beams during the measurement 2 at $\beta = 0.03$. The solid line is the profile for the counter-propagating dye laser ($\omega_0^{dye} = (0.77 \pm 0.02)$ mm, $z_0^{dye} = (10.9 \pm 0.3)$ m, $z_R^{dye} = (3.5 \pm 0.2)$ m) and the dashed line is the profile for the co-propagating Nd:YAG laser ($\omega_0^{Nd} = (0.60 \pm 0.02)$ mm, $z_0^{Nd} = (4.8 \pm 0.1)$ m, $z_R^{Nd} = (2.1 \pm 0.2)$ m).

	PM2 [kHz]	PM3 [kHz]
$\phi_{corr,a}$	302 ± 100	240 ± 100
$\phi_{corr,p}$	488 ± 100	302 ± 100
b_{corr}	-186 ± 141	-62 ± 141

Again, the uncertainties caused by b_{uncorr} are estimated (s. figure 7.18). For the possible angles and radial displacement uncertainties, the uncertainty for a single measurement is between -100 kHz and 200 kHz for each axis. The total uncertainty is -150 kHz and 300 kHz. The mean deviation of b_{uncorr} is estimated to be smaller than 100 kHz.

7.4.3 Verification of the phasefront correction ($\beta = 0.064$)

To test the method used for the correction caused by the on-axis phase structure of the Gaussian beam, considerably mismatched beam profiles are chosen such that the focus of the parallel laser beam is roughly at the position of PM3 and the focus of the antiparallel laser far outside the ring. In figure 7.19 the beam profiles are plotted. The values for the phasefront corrections are determined and given in the following table. The reason for the high uncertainty for the correction of the parallel beam is the sensitivity on small variations of the beam parameters. The frequency measurements with this laser beam profile are shown later (s. section 7.7.3).

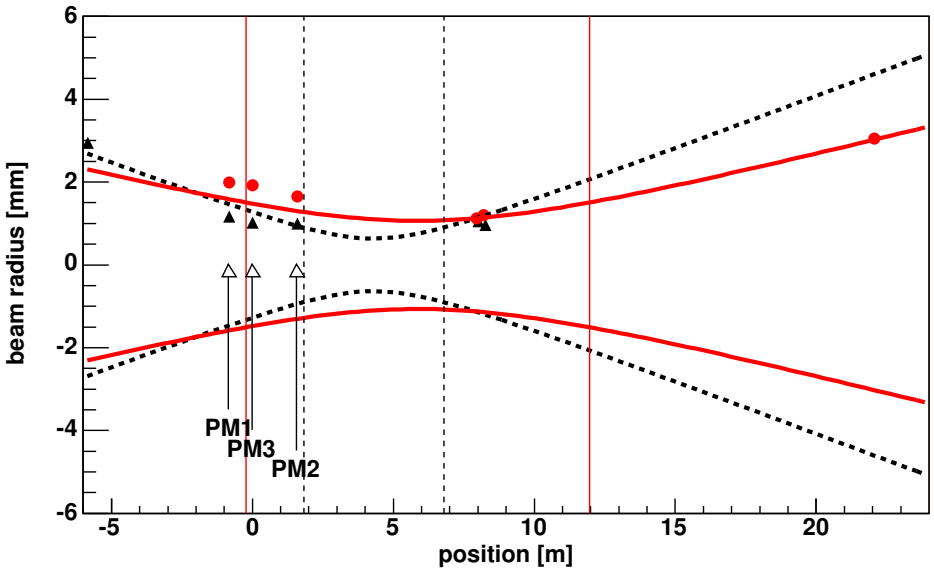

Figure 7.17: Position of the Gaussian laser beams during the measurements at $\beta = 0.064$. The solid line is the profile for the counter-propagating dye laser ($\omega_0^{dye} = (1.07 \pm 0.05)$ mm, $z_0^{dye} = (5.9 \pm 0.7)$ m, $z_R^{dye} = (6.1 \pm 0.6)$ m) and the dashed line is the profile for the co-propagating Ar^+ laser ($\omega_0^{Ar} = (0.64 \pm 0.03)$ mm, $z_0^{Ar} = (4.3 \pm 0.2)$ m, $z_R^{Ar} = (2.5 \pm 0.2)$ m).

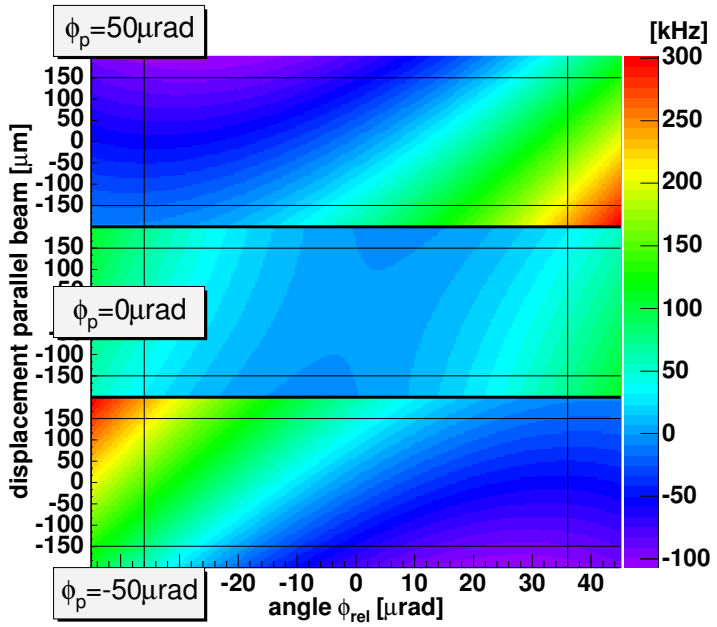

Figure 7.18: Values of b_{uncorr} for $\beta = 0.064$. For explanation see figure 7.15.

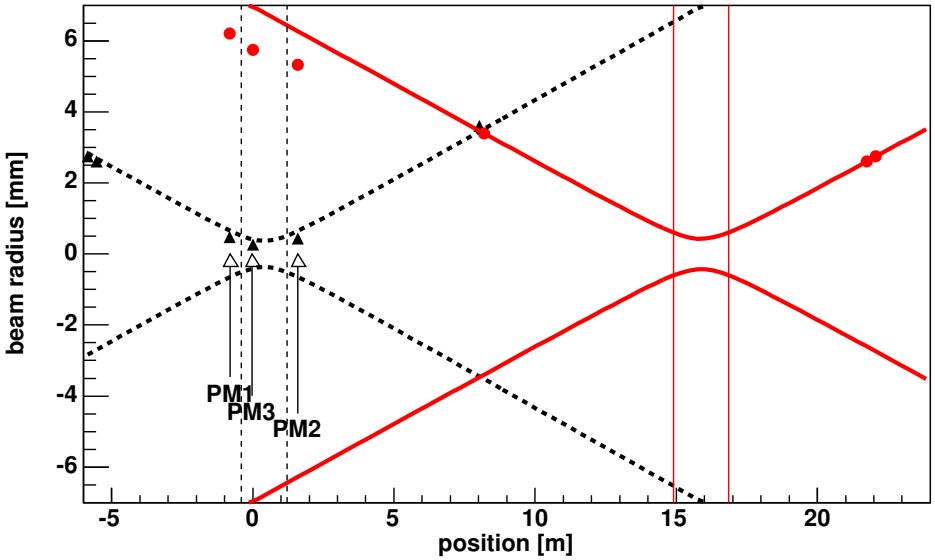

Figure 7.19: Laser beam profile used to produce an extreme frequency shift due to phasefronts ($\beta = 0.064$). The parameters for the parallel laser beam (dashed line) are $\omega_0^{Ar} = (0.36 \pm 0.01)$ mm, $z_0^{Ar} = (0.40 \pm 0.08)$ m and $z_R^{Ar} = (0.81 \pm 0.03)$ m. For the antiparallel beam (solid line) the parameters are $\omega_0^{dye} = (0.43 \pm 0.01)$ mm, $z_0^{dye} = (15.9 \pm 0.14)$ m and $z_R^{dye} = (0.97 \pm 0.04)$ m.

	PM2 [kHz]	PM3 [kHz]
$\phi_{corr,a}$	100 ± 50	100 ± 50
$\phi_{corr,p}$	1400 ± 300	1900 ± 400
b_{corr}	-1300 ± 300	-1800 ± 400

The total uncertainty of b_{uncorr} for a single measurement is obtained with the same methode as for the other laser beam profiles. The value is ± 350 kHz. The mean deviation of b_{uncorr} is estimated to be smaller than 150 kHz.

7.5 Laser intensity dependence of the line position

In the work of G. Saathoff, a large laser intensity dependence of the measured transition frequency of the lithium ion is observed. Because the exact physical relation between frequency and laser intensity was not known, a general fit of the form $a \cdot I^b + c$, where I is the laser intensity, was used to extrapolate to intensity zero (s. figure 7.20 from [SKE+03]). The uncertainty of the extrapolation with this general function is approximately three times larger than with a linear function. This is, together with the uncertainty of the rest-frequency of the lithium ion[9], the largest uncertainty in [SKE+03]. As it is mentioned in [SKE+03] the reason for this are perturbations

[9]The absolute uncertainty of ν_0 was 400 kHz but $\nu_a = \nu_0^2/\nu_p$ and due to the square of ν_0 the relative uncertainty contained in the uncertainty of ν_a is multiplied by two.

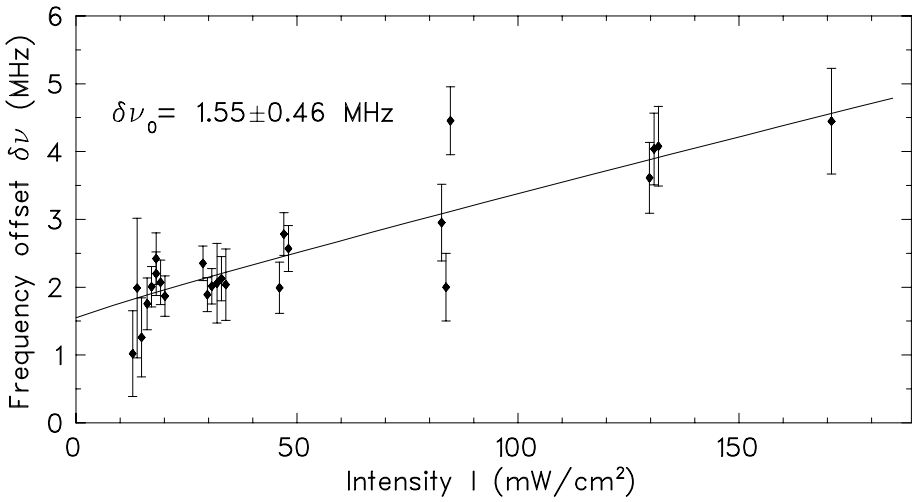

Figure 7.20: Results of the measurements carried out by G. Saathoff et al. from [SKE+03]. The abscissa shows the total laser intensity and the ordinate the frequency of the scanning dye laser, when the transition is observed, relative to an iodine line. It seems that the transition frequency is a linear function of the laser intensity

.

of the saturation signal, that are not fully canceled out by the background subtraction, because the perturbations are on the same time scale. There exist several papers [GM89b][GM89a][GM90][CS02][ACM00][MACI99], where the interaction between the laser and the particle influences the velocity distribution of the sample. This also influences the line shape and the position of the minimum of the Lamb dip. The results given in these papers do not fit the conditions of the present experiments completely. At first only a qualitative explanation is thus given based on these papers.

The momentum of a photon is h/λ. This momentum is transfered to the absorber. If the absorber emits a photon, it loses the momentum of the photon (exact treatment s. [Dem03]). It is well known that it is possible to decelerate or accelerate an atom by momentum transfer of photons, if the photons come from the same direction. In the present experiment the resonance frequency of the laser changes by $h\nu_0^2/(2c^2 m_{^7Li}) = 95$ kHz due the velocity change, if one photon is absorbed. The natural linewidth is 3.7 MHz, so after 39 absorption-emission[10] processes the ion can have changed its velocity so much, that it is not resonant with the laser anymore. The other forces applied to the ions are the cooling force of the electron cooler and the buncher. In figure 7.21 the ring averaged force of the electron cooler[11], buncher and the force of a laser at resonance is given. The force produced by the laser is described by [Mes99]

$$F_{laser} = \hbar k \frac{\gamma_0}{2} \frac{S}{1 + S + (2\Delta/\gamma)^2}. \tag{7.6}$$

γ_0 is the linewidth, Δ is the detuning from resonance and S is the saturation parameter.

[10]Only spontaneous emission is considered, because here the emission has no preferred direction and thus there is no net momentum transfer of the emission to the ion.

[11]Based on the D^+-data given in [Beu00].

To obtain the ring averaged force, F_{laser} is multiplied by 10/55.4, because 10 m is roughly the range where the lasers and the ions are overlapped. The forces of the buncher and the electron cooler are much smaller or equal to the light force in the range of interest, that is given by the energetical alignment precision. So the modifications due to the laser force can survive a round trip in the ring and a memory effect is possible.

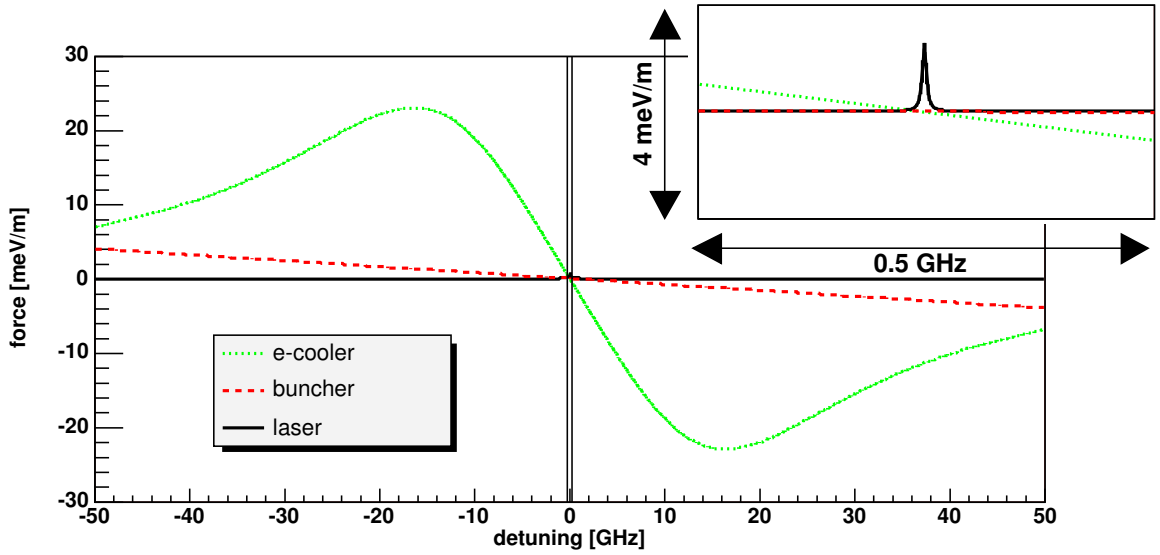

Figure 7.21: The three different forces as a function of detuning from the desired frequency. Only the effect of the parallel laser is plotted with an intensity equal the saturation intensity. The range of interest is enlarged.

The upper state has a lifetime of $\tau = 43$ ns. In the work of G. Saathoff the time window Δt (s. section 6.1.3) in the laser switching scheme was 200 μs. An ion sees this single switching state approximately for $T = 200\mu\text{s}10\text{m}/55.4\text{m} = 36\mu\text{s}$. Because no inversion is possible in an ensemble of a two-level system, the mean maximum number of absorption-spontaneous emission processes in the ensemble of ions is, using the rate equation approximation [Dem03], $T/\tau \cdot (S/(2S+2)) \approx 830 \cdot (S/(2S+2))$ (S is the saturation parameter). The factor $S/(2S+2)$ is the fraction of ions in the upper state. Thus it is not so unlikely that part of the ions are pushed out of resonance during this time even for S in the range of 0.5 to 5. The range of the distortion is in the order of the saturated linewidth. The forces of the electron cooler and the buncher[12], that can modify the longitudinal velocity, are not stronger than the laser forces as it is shown in figure 7.21. These forces do not have the possibility to smoothen out the influence of the laser on the velocity distribution. This is in contrast to spectroscopy in a gas cell where collisions between the particles and the cell walls determine the shape of the velocity distribution.

If, for example, the ions interact only with the co-propagating laser, the ions that absorb photons get faster. The velocity distribution changes from the symmetric Gaus-

[12]Heating effects like intra-beam scattering should also act on the velocity distribution. Some discussion and measurements on this point can be found in [Kle91] and [Mer00].

sian profile to an asymmetric profile (s. figure 7.22) with a peak and a dip. If one laser is modifying the velocity distribution so strongly, that a number of ions are pushed out of resonance, the other laser can not interact with them anymore, if it interacts with the same velocity group. As soon as the switching time Δt is long enough such that enough absorption-emission processes takes place to modify the velocity distribution strongly every switching state would see a different velocity distribution and the method of background subtraction used in the present experiment would not work properly anymore and the derived Lamb dip would show deviations from a Lorentzian shape.

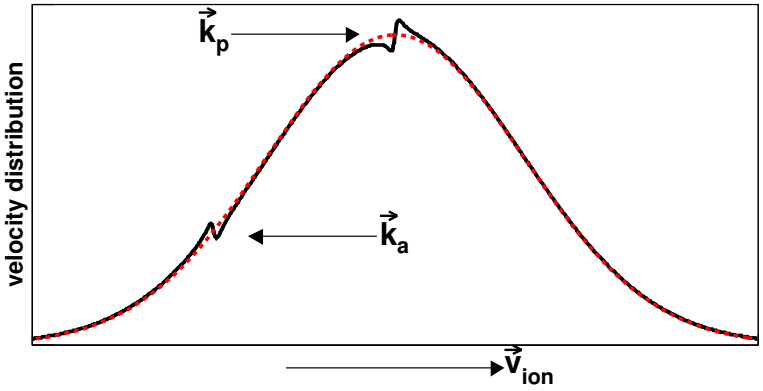

[thp]

Figure 7.22: The velocity distribution of the ions $\vec{v}_{ion}$ is modified by the laser force (solid line). For the co-propagating laser beam $\vec{k}_p$ the ions get faster. A hole (not the Benett hole) is formed in the velocity distribution at the resonance velocity and a hill is formed at higher velocity. For the counter-propagating beam $\vec{k}_a$ the ions get decelerated. For comparison a normal Gaussian is also drawn (dashed line).

To prevent this strong modification of the velocity distribution for the different switching states, the time of a single switching state is decreased. If, for example, the switching time is decreased from 200 μs to 20 μs, the number of absorption-emission processes goes down to $83(S/(2S+2))$ (for $S = 1$: 21 processes are possible), which is smaller than the minimum number of absorption-emission processes to bring an ion out of resonance. The influence on the velocity distribution should be smaller and the background subtraction better. A corresponding measurement was made at $\beta = 0.064$ and is shown in figure 7.23. The linear extrapolated values for 5 kHz and for 50 kHz agree within the given uncertainties. The shown range goes up to a saturation parameter of about 8 obtained by comparing the linewidths of the used measurements with the linewidths given in figure 7.10. For the frequency measurements in the present work a switching frequency of 100 kHz was chosen.

It is not possible to solve the problem of modifications of the velocity distribution due to the light forces completely by faster switching, because in the switching state, where the saturation signal is obtained, both lasers interact with the ions and in the other switching states only one or no laser interact with the ions. The influence on the velocity distribution is not equal for all switching states and so a residual influence on the spectroscopy is expected. In the paper of M. Artoni et al. [ACM00] that fits to some

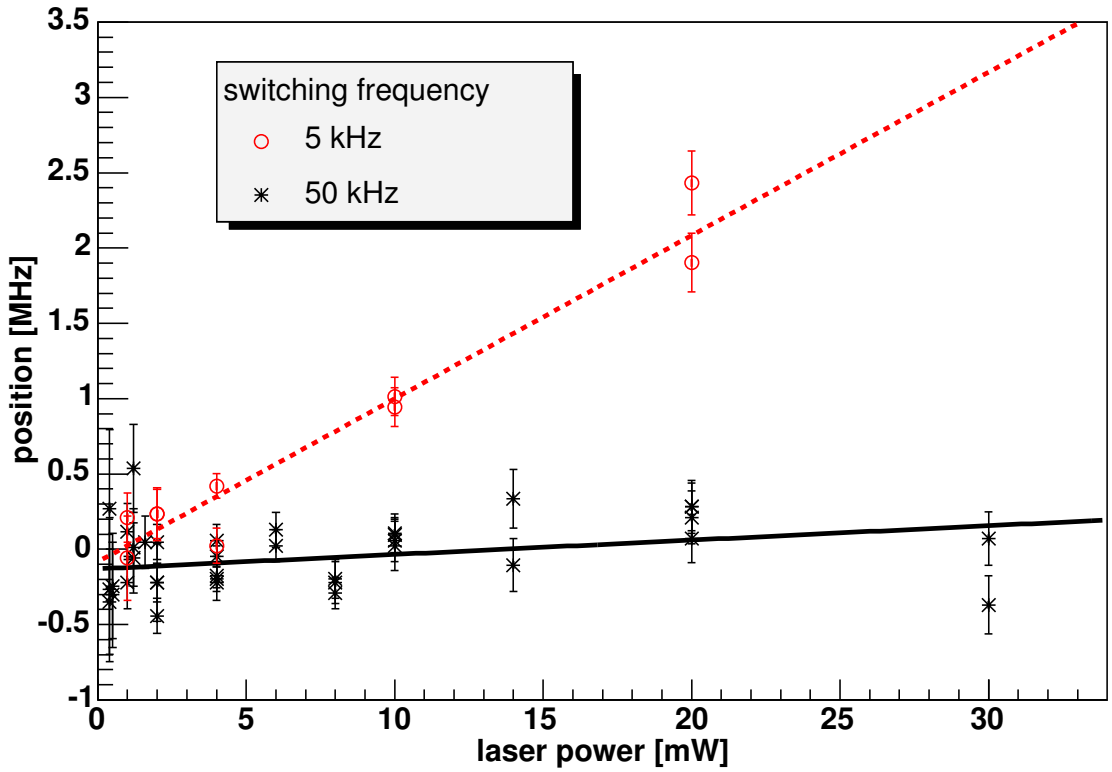

Figure 7.23: The dependence of the transition frequency given relative to an arbitrary zero point on the power decreases strongly if the switching frequency is increased. The data points are fitted by a linear function. The intercepts of both fits are within the uncertainty of the fit (5 kHz: (-0.08 ± 0.07) MHz; 50 kHz: (-0.13 ± 0.03) MHz). The slope at 50 kHz is ten times smaller than for 5 kHz (5 kHz: (0.11 ± 0.08) MHz/mW; 50 kHz: (0.010 ± 0.004) MHz/mW). Data measured with PM3 ($\beta = 0.064$).

extent to the condition of this experiment (the antiparallel laser beams have the same power and the total power is in the order of the saturation power but the frequencies of the laser beams are equal), the influence of the light forces on the saturation spectroscopy is discussed. The line profile is described by

$$N(2\pi\nu) \approx L(2\pi\nu) - \epsilon\tau_0 M(2\pi\nu), \tag{7.7}$$

where $L(2\pi\nu)$ is a symmetric function and has a Lorentzian-like shape. This function gives the line shape without modifications due to light forces. $M(2\pi\nu)$ is an odd function and gives the contribution of the light force. $\epsilon = \hbar k_L^2/(2m)$ is the single-photon recoil angular frequency and τ_0 is the interaction time. The limits of the model are that the laser power is below $S = 2$ and $\tau < \tau_0 \leq \epsilon^{-1}$ (τ is the lifetime of the excited state). From this model a blue shift of the Lamb dip center is expected which increases with τ_0. An extreme example is given in figure 7.24. The shift is a nonlinear function of the

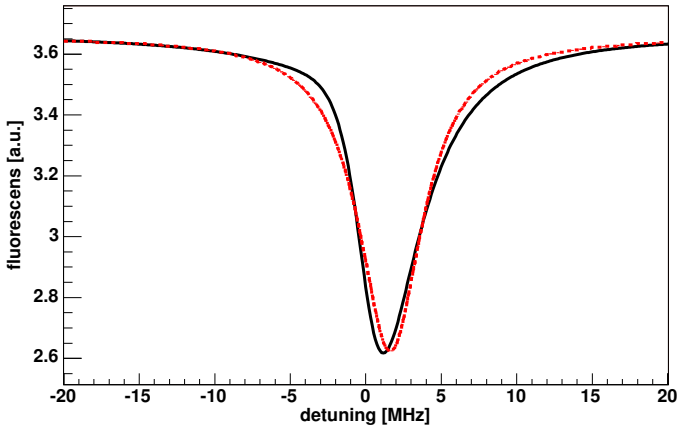

Figure 7.24: Line shape modification due to changes of the velocity distribution. The solid line is the distorted line shape and the dashed line is a fit by a Lorentzian. The centers of both lines are shifted to higher frequencies.

laser power. For a laser power that is bigger than 0.5 times the saturation power at fixed τ_0, the shift increases very slowly with the laser power and is not detectable within the accuracy of the experiment. Below 0.5 times saturation power the shift drops very fast to zero. The explanation for the blue shift of the line is that, if the laser beams are red detuned from the transition frequency, the particles are cooled by the light force; thus the number of particles is increased for the low frequency part of the signal and the fluorescence is increased. For the case that the laser beams are blue detuned, the particles are heated and the number of particles is decreased and the height of the signal is decreased. One problem is to determine τ_0. The shortest time is the time in the laser fields per round-trip. This time is higher at low ion velocities. An indicator for the smallest τ_0 is the time obtained by the time of flight analysis. For $\beta = 0.03$ the saturation free linewidth and equation 7.2 is used to estimate the flight time of the ion. The result is about 0.4 μs for PM3 and, by adding the known flight time between

PM3 and PM2, 0.6 μs for PM2. ϵ equals 596 kHz. The product $\epsilon\tau_0$ is 0.24/0.36 for PM3/PM2 and this would lead to a shift of 110 kHz/164 kHz for the fitted Lorentzian at a saturation parameter of 0.5. At $\beta = 0.064$ the values obtained in the time of flight analysis are used. The value for τ_0 at PM3 is 0.13 μs and this leads to a $\epsilon\tau_0$ of 0.08. For PM2 τ_0 is 0.21 μs and $\epsilon\tau_0$ is 0.13. The shift here is 35 kHz/ 59 kHz for PM3/PM2. The measured frequency at low velocity would be more or less 75 kHz to 100 kHz higher in frequency compared to the high velocity measurement.

To demonstrate, that there are some aspects that are not understood in detail, some measurements are shown that are much higher in intensity than the measurements used later for the frequency measurements. One example shows the line shape at low switching frequency and high laser power (s. figure 7.25). The line shape is similar to the distorted line shape plotted in figure 7.24. So this is an indicator that the reasons for the distortion might be based on the same effect as described in [ACM00]. This distortion is not detectable at lower laser power. At higher switching frequencies this effect is strongly suppressed which explains perhaps the much smaller laser power dependence of the line position.

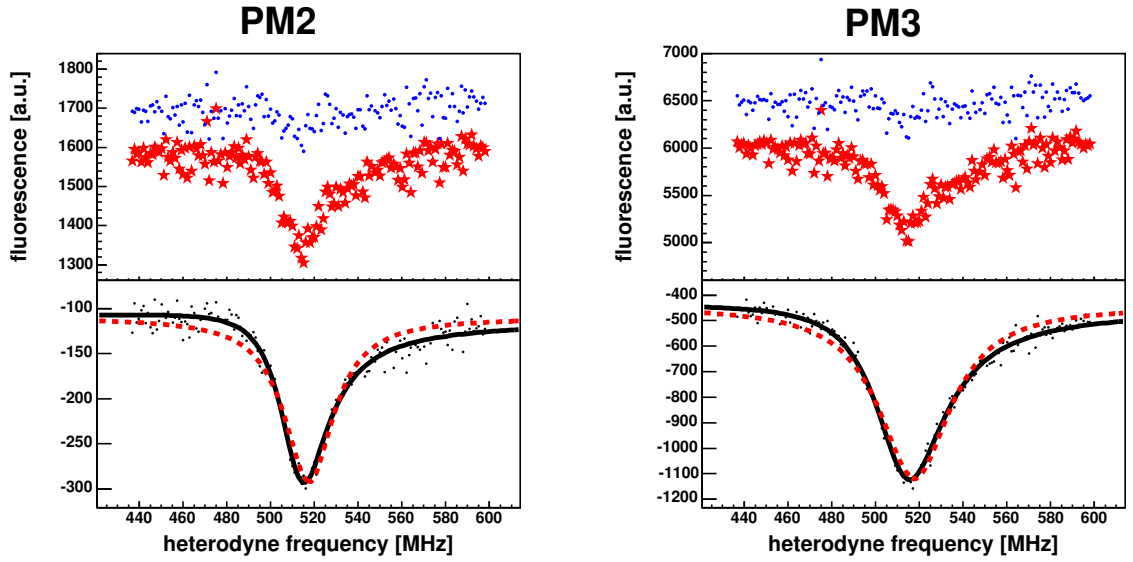

Figure 7.25: Line shape at low switching frequency (7 kHz) and high laser intensity (S$\approx$ 8). The solid line (fit-function: Lorentzian+$a\delta/(\delta^2 + \gamma^2/4)$, δ is the detuning and a is strength of the modification) is the distorted line shape similar to the line shape in figure 7.24 and the dashed line is a fit of a Lorentzian. The minima of the two fits are not equal ($\beta = 0.064$).

As mentioned earlier it is not so easy to determine τ_0 due to a possible memory effect of the ions and it is perhaps different for different laser powers, because at higher laser powers the range of modification is increased by the broadening due to saturation and will survive for a longer time in the storage ring. The width of the Bennett hole in the population distribution increases with the laser intensity by $\gamma_0\sqrt{1+S}$ (γ_0 is the

linewidth without saturation) and this is the same range for modification of the velocity distribution. Is now a heating effect[13] with a heating rate H present in the ion beam, it can be estimated how much time $\hat{\Delta}t$ is needed to cancel out the influence of the laser. The change of the kinetic energy of the ion (in the rest frame of the ion) should be equal to the temperature change $m\Delta v^2/2 = k_B\Delta T = k_B H\hat{\Delta}t$ with m being the ion mass and k_B the Boltzmann constant. The velocity change can be translated to a frequency change by the Doppler formula $mc^2\Delta\nu^2/(2\nu_0^2 k_B) = H\hat{\Delta}t$ with ν_0 as transition frequency. Now $\Delta\nu$ is replaced by the width of the Bennett hole $mc^2\gamma_0^2(1+S)/(2\nu_0^2 k_B) = H\hat{\Delta}t$. As final result the time scale is obtained that is necessary for washing out the influence of the laser on the velocity distribution

$$\hat{\Delta}t = mc^2\gamma_0^2(1+S)/(2\nu_0^2 H k_B). \tag{7.8}$$

In the reference [ACM00] the line-shift is, approximately, proportional to the interaction time τ_0. $\hat{\Delta}t$ can be interpreted as the maximum interaction time, because after the time $\hat{\Delta}t$ modifications due to the laser field are eliminated. The maximum interaction time is proportional to the laser power and thus also the line-shift is proportional to the laser power. This behavior can be observed in figure 7.23 at low switching frequencies, because the duration of one switching state is longer than the maximum interaction time. So τ_0 can be bigger than the lower limits given earlier. Is the duration Δt of one switching state much longer than $\hat{\Delta}t$, then the background subtraction would not include the modifications of the velocity distribution produced by the switching state for the saturation signal. If now the duration for a switching state is in the order of $\hat{\Delta}t$ the states for the background subtraction also includes these modifications and after the background subtraction the influence of the odd term in eq. 7.7 would be reduced. At very high switching frequencies the duration of one switching state can be shorter than $\hat{\Delta}t$ and for the velocity distribution of the ions it seems that both lasers interact with ions simultaneously even when applied separately for the background subtraction. Now the background subtraction overcompensates the odd term, because the state for the saturation signal is first in the switching scheme (s. figure 6.9) and the interaction time for this state is determined by the switching frequency. For the states measuring the background signal the interaction time is longer and thus τ_0 bigger than for the saturation signal and the odd term in eq. 7.7 would be bigger than the saturation signal. This overcompensation leads to a red-shift instead of a blue-shift of the background subtracted saturation signal. In figure 7.26 and 7.27 measurements are plotted for different switching frequencies $1/\Delta t$ and laser powers. At 5 kHz switching frequency the position of the line depends strongly on the laser power. For higher switching frequencies this is strongly reduced. The effect is not so big for the high velocity measurements compared to the low velocity measurements due to a possible shorter interaction range[14] and/or a possible higher heating rate H. The measurements at low ion velocity show an overcompensation for the higher switching frequencies that

[13] Every effect that influences the velocity distribution, like electron cooling and intra beam scattering.

[14] The duration t for the possible interaction between light and ions depends only on the ratio of the overlap length L between ion beam and laser beams and the ring circumference U and the switching frequency f by $t = L/(fU)$. In principle L should be equal for the different velocities but from the time of fight analysis it seems that for low velocity L is bigger than for high velocity.

can be a indicator for a lower heating rate compared to the measurements at high velocity. The line position at low laser power shows no dependence on the switching frequency that can be explained by the fact that the maximum interaction time is shorter than the shortest time of a single switching state. At low velocity the round trip frequency is 162 kHz which is lower than the highest switching frequency. So the minimal interaction time given earlier can be used as a estimation of the real interaction time for low laser power. The same behavior for low laser power is observed at high ion velocity and thus also the minimal interaction time as estimation is used even if no measurement with a switching frequency higher than the round trip frequency is available. At high laser powers (S≈6) the memory effect (the modification of the velocity distribution) is visible as step in the sum signal of the switching states where only one laser is on (s. figure 7.28). In the given measurement the direction of laser tuning is towards higher frequency and the intensity of the antiparallel laser is approximately by a factor 1.5 bigger than the intensity of the parallel beam.

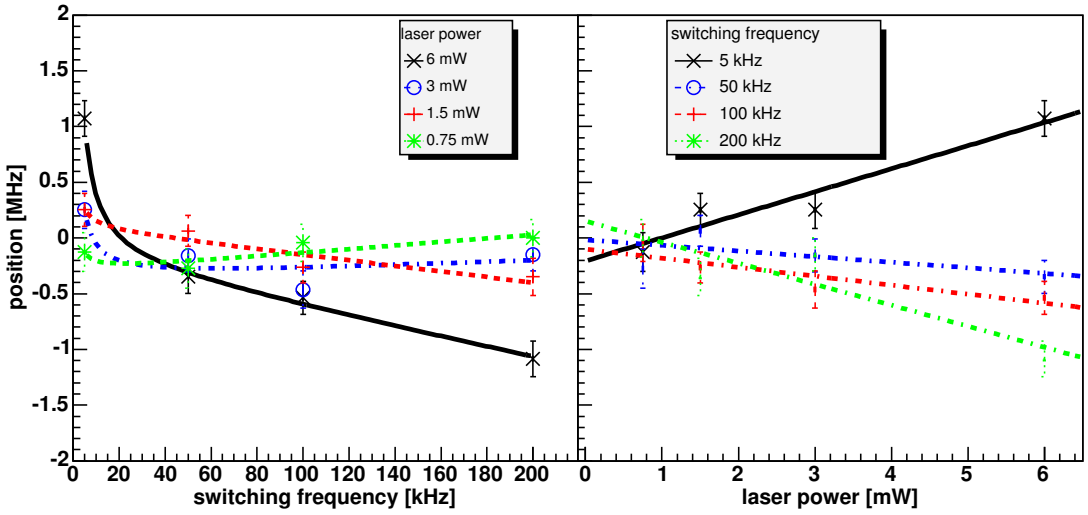

Figure 7.26: Left: Change of the measured transition frequency relative to an arbitrary reference as a function of the switching frequency at different laser power. The lines are described by the function $a/f + bf + c$ with f as switching frequency. Right: Change of the measured transition frequency as a function of the laser power at different switching frequencies. The data curves are fitted by linear functions. Data collected with PM3. ($\beta = 0.03$)

The conclusions from all these observations are that at high laser powers a strongly distorted line shape is observed that leads to a shift of the line center. The position of the line at low laser power is independent of the switching frequency, which means that even the switching time at 200 kHz is longer than the lifetime of the laser induced distortion on the velocity distribution. Thus, as motivated before, the frequency shifts obtained by the smallest possible interaction times are used. By comparing figures 7.26 and 7.27 it seems that the low velocity measurements are more sensitive than the high velocity measurements. These observations show that laser-induced frequency

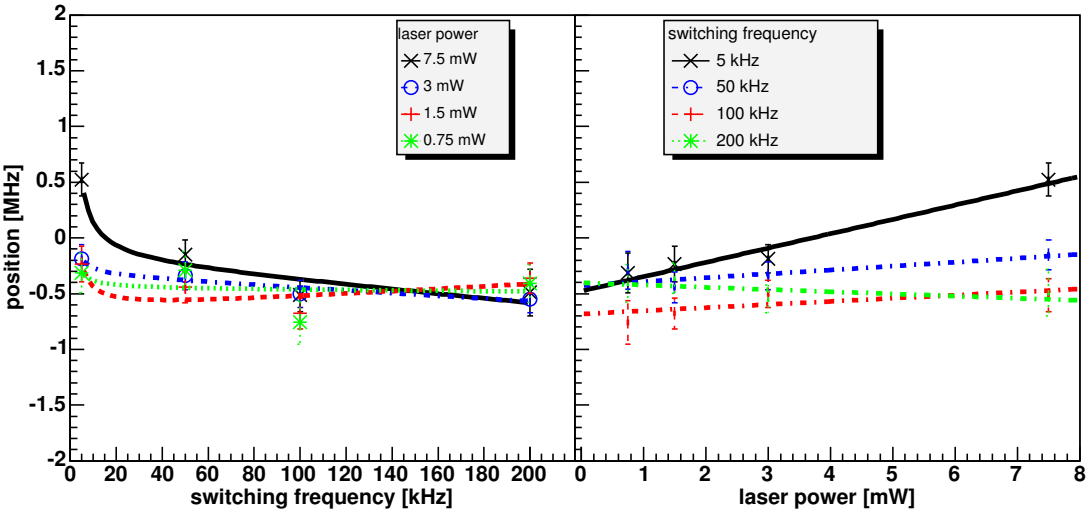

Figure 7.27: Left: Change of the measured transition frequency relative to an arbitrary reference as a function of the switching frequency at different laser power (details in figure 7.26). Right: Change of the measured transition frequency as a function of the laser power at different switching frequencies. The data curves are fitted by linear functions. Data collected with PM3. ($\beta = 0.064$)

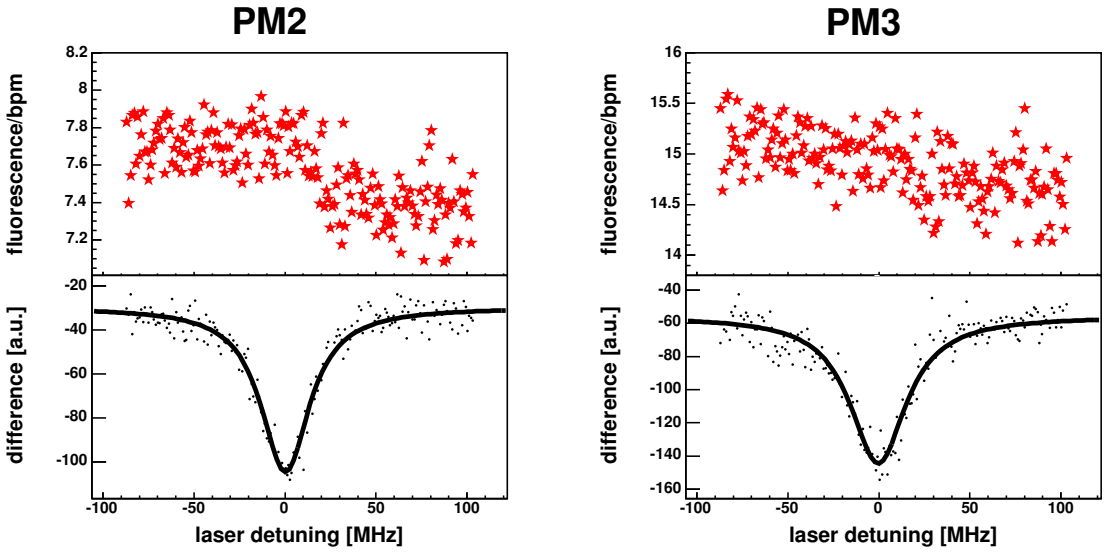

Figure 7.28: The upper half of the picture shows the sum of the switching states when only one laser is on, normalized to the measured BPM signal to obtain a signal free from fluctuations of the ion current. A step is observable in the signal. In the lower half the background free saturation signal is plotted with a Lorentzian as fit function. The switching frequency is 100 kHz.($\beta = 0.03$)

shifts should be taken into account despite of the background subtraction and the linear extrapolation to zero laser power carried out for the frequency measurements in section 7.7. To reduce the uncertainty from this error source, a more detailed line shape model is needed that describes the observations for the different experimental conditions (laser power, only one laser is tuned, switching frequency, influence of buncher, electron cooler, background subtraction and heating effects). A 100% uncertainty of this correction is chosen, because the model from [ACM00] does not fit completely to the experiment and the effect can be weakened by heating effects. The measured absolute frequencies will be corrected to lower frequencies by a value of (110 ± 110) kHz/(164 ± 164) kHz for PM3/PM2 at $\beta = 0.03$ and (35 ± 35) kHz/(59 ± 59) kHz for PM3/PM2 at $\beta = 0.064$, because the measured frequencies are shifted to higher frequencies due to the influence of the light on the velocity distribution.

7.6 Magnetic effects

7.6.1 Testing the sensitivity to magnetic fields

As mentioned in section 6.1.2 a small coil, which produces a solenoid field, is placed near the position of PM3 to test the sensitivities of the spectroscopic signal to magnetic fields. This measurement is carried out at $\beta = 0.03$, because the interaction time/rotation between the ions and the magnetic field is longer and thus a bigger influence is expected. The setup at PM3 with the influence on the spectroscopy at different velocities is illustrated in figure 7.29. To get a clear signal the light is circularly polarized to maximize the sensitivity to magnetic fields (s. chapter 3). The linearly polarized light after the fiber passes an achromatic quarter wave-plate before it enters the TSR to get circularly polarized light. The measured frequency as a function of the magnetic field[15] is given in figure 7.30. As expected, the position shows a linear dependence of the coil-current. The sign of the slope changes if the polarization is changed from left to right circular and if the magnetic field changes its direction. The absolute value of the slope is roughly (1.07 ± 0.03) MHz/Gauss. Also the linewidth increases with the magnetic field strength, because the magnetic field is not homogeneous over the whole interaction length and the different Zeeman splittings of the levels also increase the linewidth[16].

7.6.2 Magnetic fields and linear polarization

As shown in appendix A, a linearly polarized light beam can be interpreted as a superposition of a left- and right-circular light beam. Also the magnetic field is vertical to the polarization and so no $\Delta m = 0$ transition is possible. Only transitions with $\Delta m = \pm 1$ are possible. So the expected observation is a splitting of the line in two lines, that are separated roughly by ± 1.2 MHz/Gauss with respect to the undisturbed

[15] The mean magnetic field of 4 Gauss/A is used (s. figure 6.8).

[16] It is assumed that no memory effect exist here due to the high magnetic fields in the dipoles, because in the dipoles of the ring the magnetic field is several 1000 Gauss which leads to Zeeman shifts that are equal to the hyperfine structure splitting.

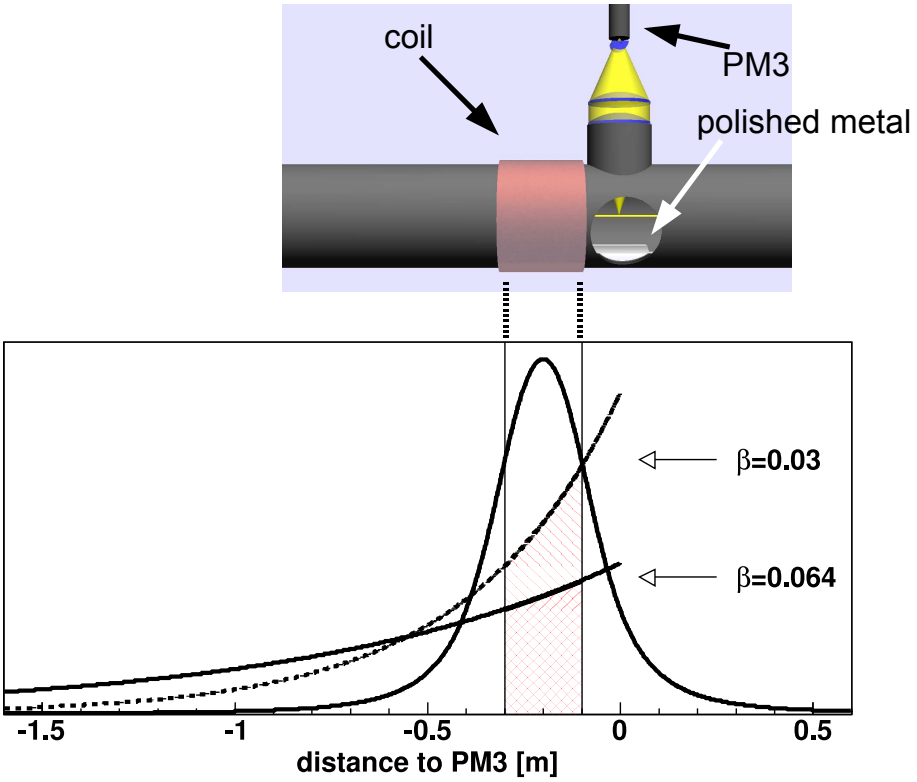

Figure 7.29: The profile of the magnetic field of the external coil is plotted (s. figure 6.8). The dashed line gives the contribution to the detected signal (s. section 6.3.1) for $\beta = 0.03$ and the solid line gives the contribution to the detected signal for $\beta = 0.064$ for the same signal strength. The vertical lines give the extension of the coil. In the range of the coil the area under the curve for $\beta = 0.03$ is bigger compared to the area for $\beta = 0.064$.

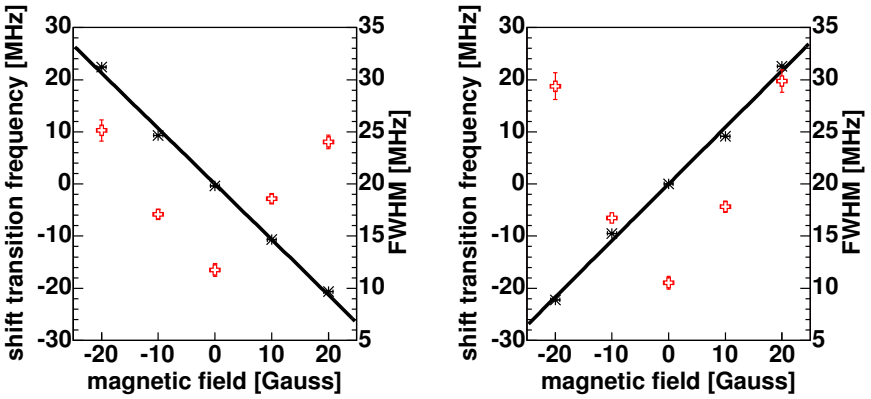

Figure 7.30: Position (star) and width (cross) of the lithium-ion transition as a function of the magnetic field produced by the external coil. On the left side the light polarization is left circular and on the right side the light is right circular ($\beta = 0.03$).

transition frequency. In figure 7.31, measurements at different strengths of the magnetic field with linearly polarized light are shown. A splitting is observable but it can also be seen, that the lines smear out because the magnetic field is not homogenous over the whole interaction length. At the highest magnetic field, the splitting is strong enough to see the unshifted signal of the ions that interacts with the light field before entering the magnetic field. The line splitting should be symmetric in the line strength, but it seems that the part shifted to higher frequency is a little bit weaker than the part shifted to lower frequency. This can be an indicator that the light is not perfectly linearly polarized but the effect seems to be to large given to the measured degree of linear polarization of 98%. Another reason could be that the population of the Zeeman levels in the ground state are not symmetrical. To make this point more clear, an extreme example is given. If all ions are in the $m_F = 5/2$ ground state then the shift for the left circular component is -1 MHz/Gauss. The shift for the right circular component is 1.4 MHz/Gauss. Because the magnetic field is shorter than the decay length of the upper state, also an unshifted signal without magnetic field contributes to the whole signal. The left circular component is closer to the unshifted line so the dip of the left circular component is deeper than for the right circular component due to the greater overlap with the unshifted signal. If this is the explanation for the observed line shape then the population of the Zeeman levels with positive m_F values is higher than with levels with negatives m_F values. A mechanismen to obtain an asymmetric population due to optical pumping is explained in [SS04], where a magnetic gradient and a velocity gradient exist so that the ions interact more with one circular component of the linear polarized light. This situation can be possible in the quadrupole before the experimental section.

7.6.3 Measured frequency depending on the polarization

To test the influence of magnetic fields on the line position, the polarization is gradually changed from linear to circular by changing the angle between the fast axis of the quarter wave-plate and the incoming linearly polarized light. In all plots this angle is used to describe the polarization of the light. First the results at low velocity are shown. As is depicted in figure 7.32 a large effect of the polarization on the line position at PM2 is observed also when the external solenoidal magnetic field is switched off. The line position at PM3 is less sensitive to the polarization. By fitting a sine function with the periodicity of twice the angle between the $\lambda/4$-retarder axis and the polarization direction with an arbitrary additional phase[17] to maximize the amplitude to describe the frequency change (compare appendix A) in the worst case, an amplitude of (0.65 ± 0.05) MHz for PM2 and (0.17 ± 0.06) MHz for PM3 is estimated. Taking the factor of (1.07 ± 0.03) MHz/Gauss obtained from figure 7.30, a mean magnetic field of 0.6 Gauss for PM2 and 0.2 Gauss for PM3 can be inferred. Close to the photomultipliers, ion-getter pumps are installed with permanent magnets. In the region of PM2 two pumps are placed and in the region of PM3 only one pump is placed. So this can be the reason for the different strength of the magnetic fields. To make sure that the observed behavior

[17]The phase should be zero, because with linearly polarized light no shift but only a broadening is expected if a magnetic field is present.

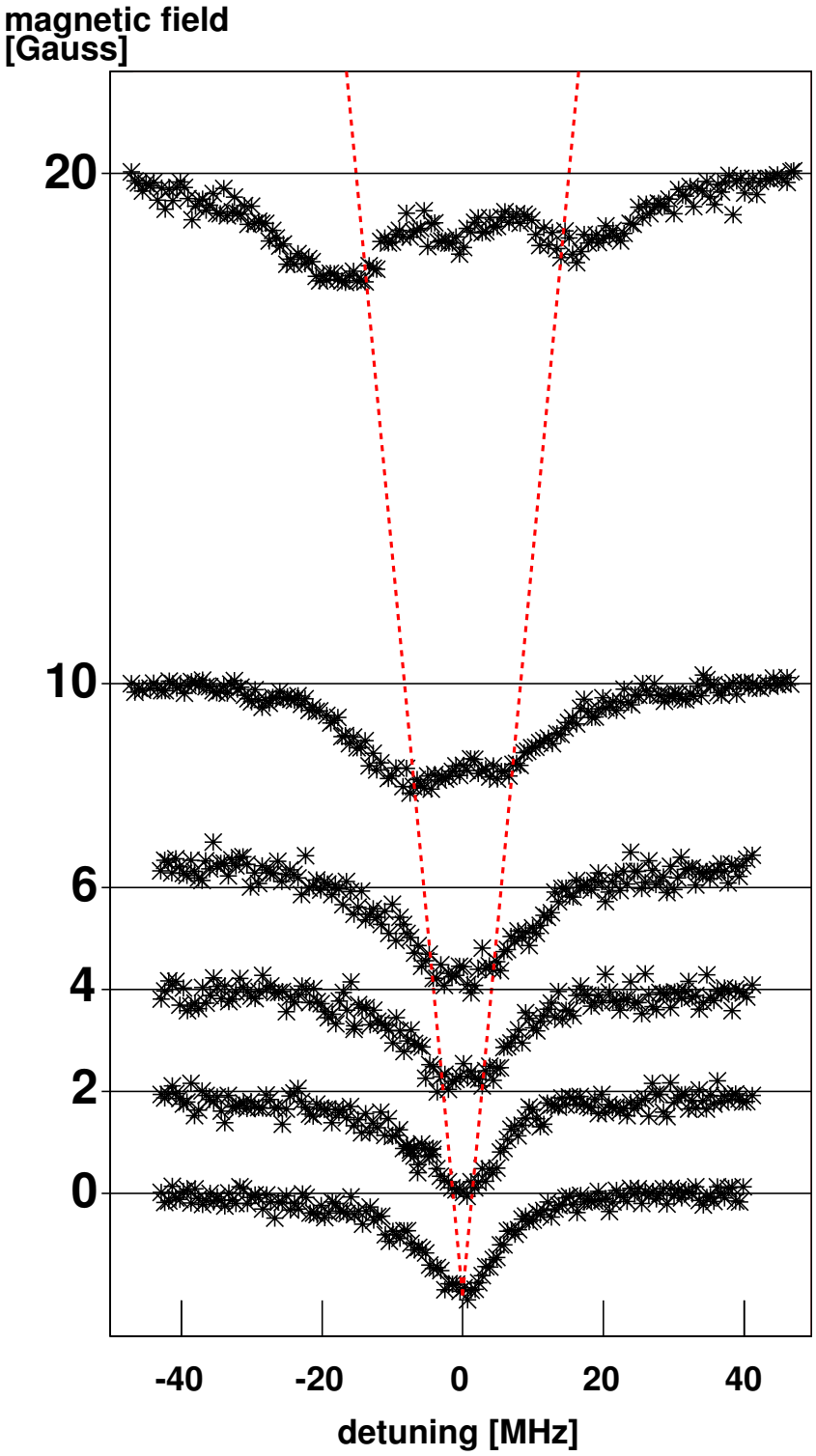

Figure 7.31: The change of the observed line shape at different magnetic field strengths.

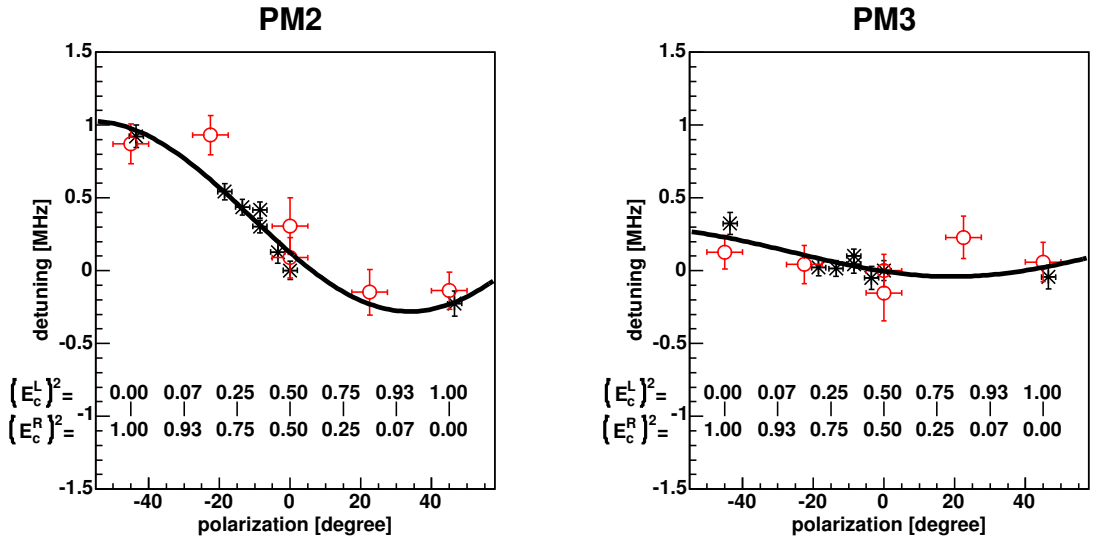

Figure 7.32: Measured dependence of the line position on polarization ($\beta = 0.03$, external magnetic field is off). The power fraction of the left-circular light $(E_c^L)^2$ as well of the right-circular light $(E_c^R)^2$ is given for the different angles. Measurements of two different beamtimes are used, that are indicated by the different symbols.

is caused by a magnetic field, an external magnetic field of 2 Gauss is applied using the coil at PM3, and the measurement is repeated. As it can be seen in figure 7.33, now the same behavior can be observed at the position of PM3. The amplitude of the sine is now (1.11 ± 0.07) MHz for PM2 and (3.09 ± 0.07) MHz for PM3. The magnetic field, that is recognized by PM2, must have a component in the same direction as the external magnetic field, because the direction of the frequency change is equal for measurements with equal polarization. The amplitude at PM2 is now a factor of two bigger. This can be explained by additional pumping effects, in the coil that populate the states with higher frequency shift.

The same measurements are carried out at high velocity (s. figure 7.34, without external magnetic field). The effect of polarization is smaller than the sensitivity of the experiment. Here also a sine function is fitted to the data but this does not give such a nice result as the low velocity measurements. The amplitude is (0.14 ± 0.06) MHz for PM2 and (0.16 ± 0.07) MHz for PM3. The two possible reasons for the different behavior are

1. the magnetic field of the environment, that is seen by the ions until they reach the position of the photomultipliers, has changed between a beamtime at low velocity and a beamtime at high velocity or

2. the ions are so fast, that the area with the magnetic field contribute only a smaller part to the measurement signal.

A direct measurement of the magnetic field in the experimental section during the running experiment is not possible so these measurements are the only indicators of a

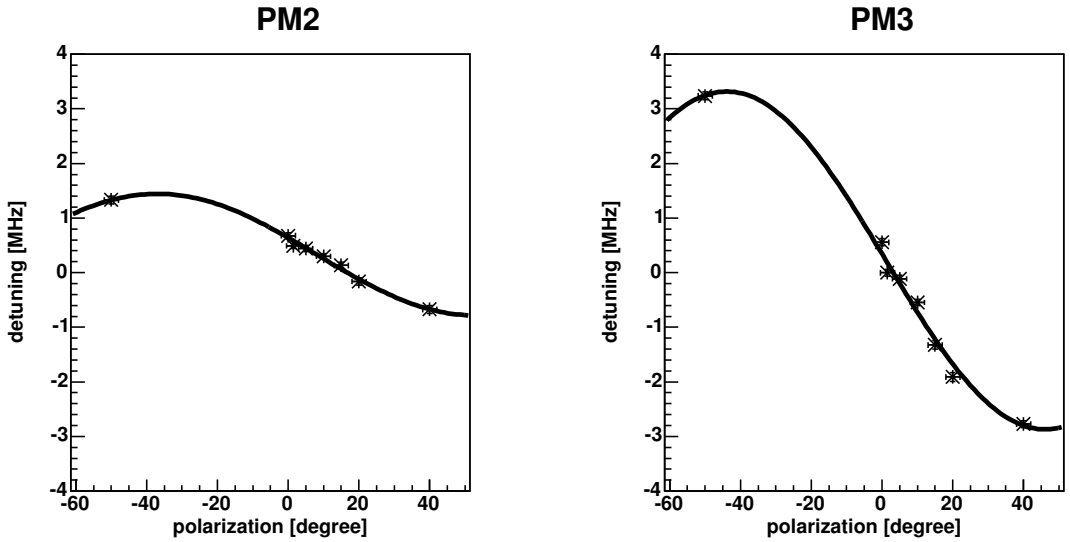

Figure 7.33: Dependence of the line position on polarization ($\beta = 0.03$). An external magnetic field of 2 Gauss is applied just in front of PM3.

magnetic field. A measurement of the magnetic field is possible during the time when the section with the photomultipliers is not installed in the TSR. It shows that the size of the magnetic field is in the mean 0.5 to 0.8 Gauss. This is in principle the size of the magnetic field of the earth. The magnetic fields at PM2 are a little bit higher compared to the position of PM3 but it is not clear how the magnetic field change when the section is build into the ring.

The measurements with the external field show the same behavior as at the low velocity measurement, but with a much smaller amplitude of the sine even though the magnetic field is 4 Gauss. The amplitude is (0.41 ± 0.05) MHz for PM2 and (2.10 ± 0.05) MHz for PM3. This observation corroborates the second explanation of why practically no polarization induced frequency shift is detectable at PM2 for high ion velocity.

The absolute frequency measurements were carried out with linear polarized light (98% of the light is linear polarized) to reduce the influence of the magnetic field effects. For the absolute frequency measurements an uncertainty due to magnetic effects is deduced from the amplitudes of the sine fits and the uncertainty of the degree of linear polarization is estimated. For all photomultipliers a value of 50 kHz is used except for the measurements at low velocity with PM2, here a value of 200 kHz is used.

7.7 Frequency measurements

Now the frequencies ν_{01} ($\beta = 0.03$) and ν_{02} ($\beta = 0.064$) are determined from the square root of the products of the laboratory frequencies of the laser beams via equation 6.27, including the term b_{uncorr}, that is treated as uncertainty in the frequency measurement, and b_{corr}. The uncertainty of ν_{01} and ν_{02} is connected to the uncertainties of the other

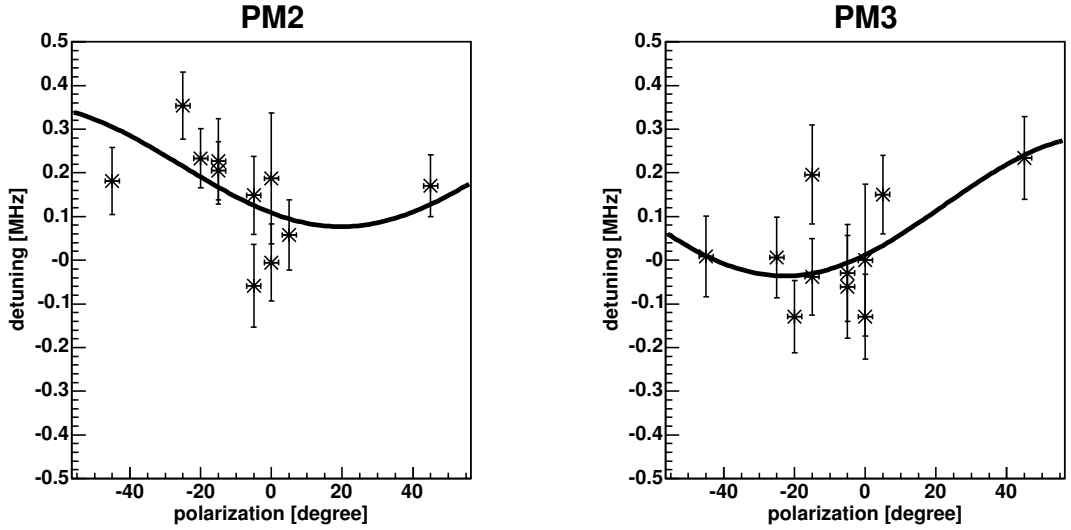

Figure 7.34: Dependence of the line position on polarization without an external magnetic field ($\beta = 0.064$).

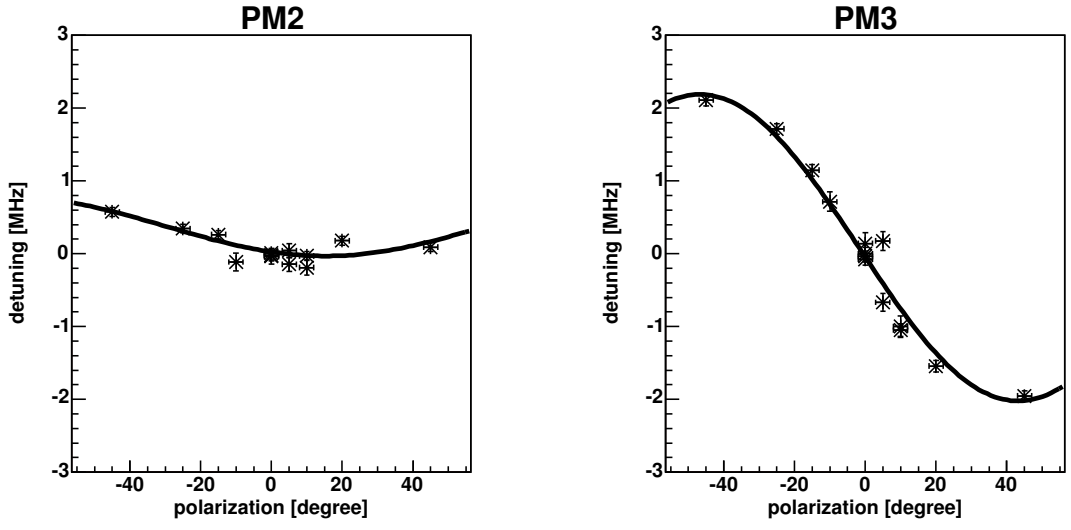

Figure 7.35: Dependence of the line position on polarization ($\beta = 0.064$) with an external magnetic field of 4 Gauss at the position of PM3.

values by

$$\Delta\nu_{0x} = \sqrt{\left(\frac{\Delta b_{corr}}{2}\right)^2 + \left(\frac{b_{uncorr}}{2}\right)^2 + \left(\frac{\nu_{ax}\Delta\nu_{px}}{2\sqrt{\nu_{ax}\nu_{px}}}\right)^2 + \left(\frac{\nu_{px}\Delta\nu_{ax}}{2\sqrt{\nu_{ax}\nu_{px}}}\right)^2}. \quad (7.9)$$

For a single measurement point, the uncertainty b_{uncorr} and the uncertainty of the Lamb dip center determination, that is part of $\Delta\nu_{ax}$, is considered. All other uncertainties and correction b_{corr} are applied to the extrapolated frequency at zero laser power. Only those measurements are used where the measured line-shape can be well described by a Lorentzian function. As quality factor, a χ^2-test with a confidence level of 95% is used. This is not done for the measurements in section 7.5. There all available measurements are used. For small and moderate laser power (approximately up to 3 times the saturation power) the confidence level is fulfilled by the most measurements (s. figure 7.36). At higher laser powers the confidence level is only fulfilled for a few measurements. An example for a measurement, that is not taken into account, is shown in figure 7.37. The background is not constant but can be described better by a linear function. That the signal gets an antisymmetric feature, as already been demonstrated in section 7.5. To include such measurements in the data analysis, a broader frequency range should have been measured until the unmodified background is reached but this is not done in the current work. Also a better understanding of the line shape would be necessary.

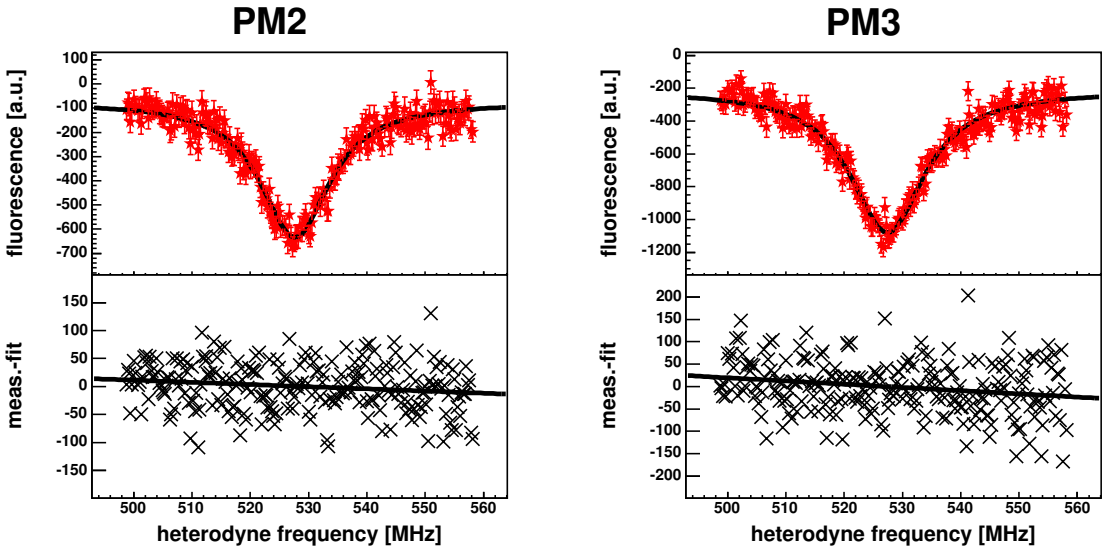

Figure 7.36: Measurement at low laser power ($S \approx 2$) at $\beta = 0.03$. The probability for the measurement at PM2 with a $\chi^2 > 252$ for 224 degree of freedoms is 9%. For PM3 the measurement with a $\chi^2 > 213$ for 224 degree of freedoms is 69%. The difference between the measured signal and the fitted Lorentz function with a constant background is also plotted with a fitted linear function.

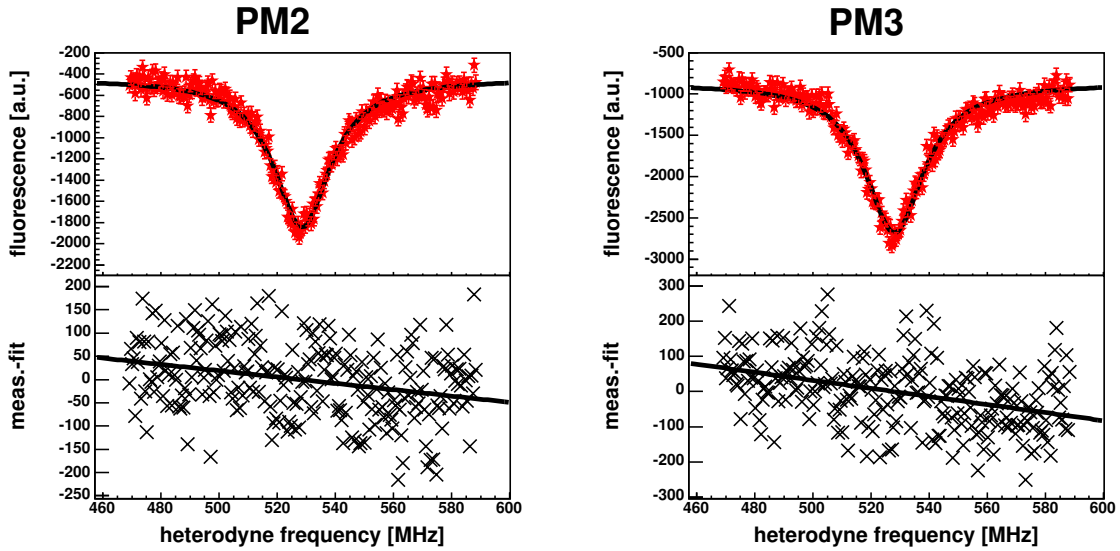

Figure 7.37: Measurement at high laser power ($S \approx 7$) at $\beta = 0.03$. The probability for the measurement at PM2 with a $\chi^2 > 312$ for 234 degree of freedoms is 0.04%. For PM3 the measurement with a $\chi^2 > 338$ for 224 degree of freedoms is 0.001%. The difference between the measured signal and the fitted Lorentz function with a constant background is also plotted with a fitted linear function.

contribute	value	uncertainty
R(56)32-0 a_{10}	563 260 223 513 kHz	5 kHz
R(57)32-0 a_1-R(56)32-0 a_{10}	−50 946 885 kHz	5 kHz
pressure difference	6.6 Pa	
frequency shift due to pressure	−28 kHz	13 kHz
R(57)32-0 a_1	563 209 278 600 kHz	15 kHz

Table 7.1: Determination of the transition frequency of R(57)32-0 a_1 at 6°C.

7.7.1 Low velocity $\beta = 0.03$

Measurement 1. At low velocity, the frequency of the parallel laser beam is stabilized to the transition frequency of the iodine line R(57)32-0 a_1. The transition frequency is given in [Qui03] as a relative frequency distance to the well known value of the transition R(56)32-0 a_{10}, that is measured at a temperature of $-15°C \hat{=} 0.8$ Pa. The frequency shift as function of the pressure in the iodine cell is estimated as -4.2 ± 2 kHz/Pa. With this information the absolute frequency of R(57)32-0 a_1 is corrected for the cold finger temperature of the iodine cell of $6°C \hat{=} 7.4$ Pa used in the present work (s. table 7.1). For the antiparallel beam, the scanning dye laser is offset-locked relative to the second dye laser, that is locked to the transition P(80)21-1 a_{10}. The absolute frequency of this transition was separately measured by a frequency comb at the used temperature (s. appendix B). The value is (530 222 434 291 ± 73) kHz. Because for the absolute frequency measurement as well as for the time dilation experiment the same setup and electronics was used, the uncertainty should stay the same. The calculation of the

antiparallel beam	value [kHz]	uncertainty [kHz]
iodine line P(80)21-1 a_{10}	530 222 434 291	73
AOM of spectroscopy	−80 000/2	< 1
AOM for switching	220 000	< 1
ion beam divergence	25	25
$\nu_{a1} + \nu_{beat}$	530 222 614 316	77
parallel beam		
iodine line R(57)32-0 a_1	563 209 278 600	7
lock uncertainty	–	73
AOM of spectroscopy	−80 000/2	< 1
AOM for switching	220 000	< 1
ν_{p1}	563 209 458 600	75
b_{corr} PM2:	−60	71
b_{corr} PM3:	−39	
b_{uncorr} single measurement	–	$\begin{cases} +170 \\ -60 \end{cases}$
b_{uncorr} extrapolated value	–	50
magnetic fields PM2:	–	200
magnetic fields PM3:		50
light pressure shift PM2:	−164	164
light pressure shift PM3:	−110	110

Table 7.2: The frequencies and uncertainties (1σ-values) contributing to the determination of ν_{01} ($\beta = 0.03$).

labortary frequencies of the light beams interacting with ions is given in table 7.2. The measured heterodyne frequency ν_{beat} between the two dye lasers must be subtracted from the iodine stabilized dye laser frequency, because the light in the ring is lower in frequency than the light of the iodine stabilized dye laser. The heterodyne frequency is of the order 528 MHz (s. figure 7.38). In figure 7.39 the resulting values for $\nu_{01} = \sqrt{\nu_{a1}\nu_{p1}}$ are illustrated; the given uncertainties only contain the uncertainty of the center of the Lamb dip and b_{uncorr} according to eq. 6.27. The linear fit takes the asymmetry of the uncertainties into account. The final extrapolated value to zero laser power for ν_{01} is $(546\ 466\ 918\ 858 \pm 36)$ kHz for PM2 and $(546\ 466\ 918\ 697 \pm 43)$ kHz for PM3 (s. figure 7.39). When the phasefront correction b_{corr} is applied to these values one obtains

$$\mathrm{PM2} : \nu_{01} = (546\ 466\ 918\ 888 \pm 51)\ \mathrm{kHz} \quad (7.10)$$

$$\mathrm{PM3} : \nu_{01} = (546\ 466\ 918\ 717 \pm 56)\ \mathrm{kHz}. \quad (7.11)$$

Between PM2 and PM3 there is a frequency difference of (171 ± 75) kHz observed. The light pressure shift is not included at this point but the difference of this contribution between PM3 and PM2 is of the order of 54 kHz and this is not large enough to explain the difference. This may be due to the fact that PM2 sees a larger magnetic field than PM3. This may introduce a shift even for perfectly linearly polarized light, that can occur if the population of the Zeeman levels of the ground state are asymmetric and

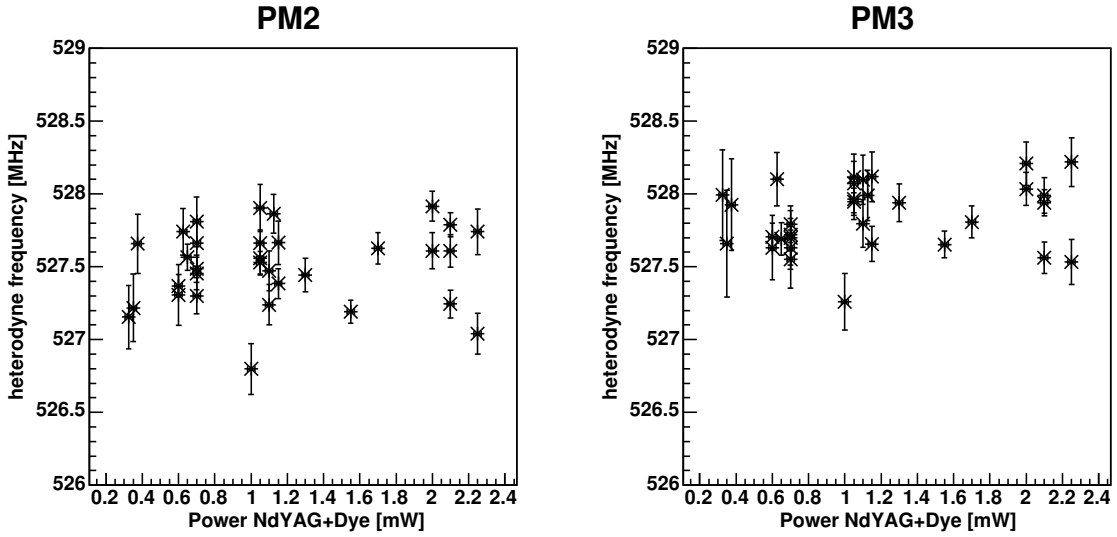

Figure 7.38: Measured values of the Lamb dip position ν_{beat} as a function of the laser power ($\beta = 0.03$, measurement 1.).

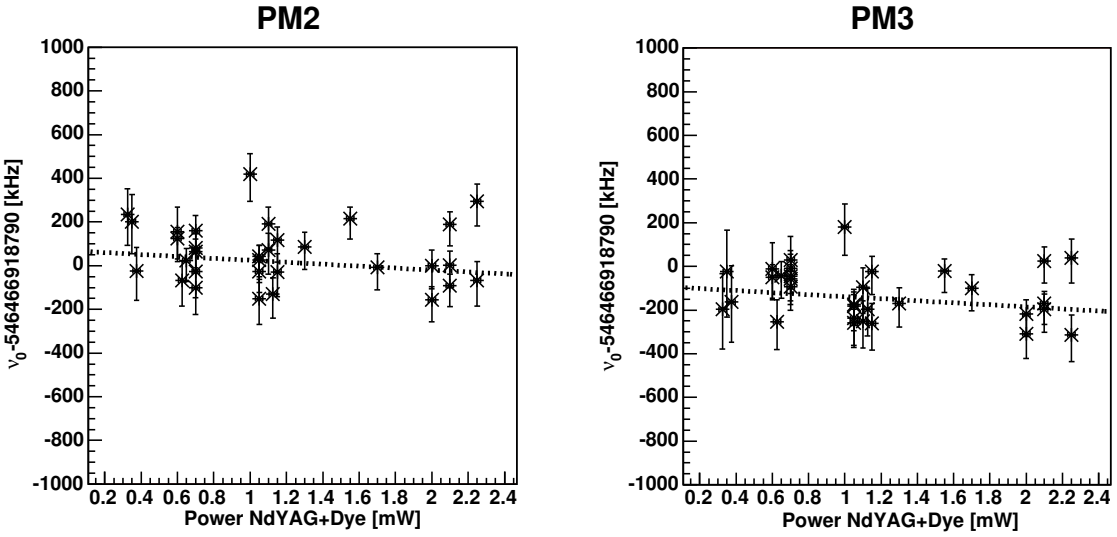

Figure 7.39: Measurement values of ν_{01} containing the line-position uncertainty of the Lamb dip and b_{uncorr} ($\beta = 0.03$, measurement 1.).

levels with positive m_F are stronger populated as explained in section 7.6.2 so a higher frequency is measured. If this argument applies, a magnetic field would introduce a shift of the measured frequency even if the light is fully linear polarized. The measurements with different polarizations of the light indicates also a possible asymmetric population of the ground state, because in figure 7.32 the sine fit is not symmetric to the zero point. The final frequency values ν_{01} with all known uncertainties included are

$$\nu_{01}^{PM2} = (546\ 466\ 918\ 724 \pm 270)\ \text{kHz} \quad (7.12)$$
$$\nu_{01}^{PM3} = (546\ 466\ 918\ 607 \pm 146)\ \text{kHz}. \quad (7.13)$$

Measurement 2. The second measurement is done in the same way like the first. The used frequencies are equal to the given values in table 7.2 except for the values of b_{corr}. The values here are (-148 ± 71) kHz for PM2 and (-76 ± 71) kHz for PM3. The measured Lamb dip position as heterodyne frequency between the two dye laser is shown in figure 7.40 and the square root of the product of the frequencies is plotted in figure 7.41. The final extrapolated value is $(546\ 466\ 918\ 856 \pm 89)$ kHz for PM2 and $(546\ 466\ 918\ 636 \pm 95)$ kHz for PM3. Applying the phasefrontcorrection b_{corr} one obtains

$$\text{PM2} : \nu_{01} = (546\ 466\ 918\ 930 \pm 96)\ \text{kHz} \quad (7.14)$$
$$\text{PM3} : \nu_{01} = (546\ 466\ 918\ 674 \pm 101)\ \text{kHz}. \quad (7.15)$$

These values agree within their uncertainties with the corresponding results from the first measurements given by eq. 7.12 and 7.13. The final frequency values ν_{01} with all known uncertainties included are

$$\nu_{01}^{PM2} = 546\ 466\ 918\ 766 \pm 282\ \text{kHz} \quad (7.16)$$
$$\nu_{01}^{PM3} = 546\ 466\ 918\ 564 \pm 168\ \text{kHz}. \quad (7.17)$$

7.7.2 High velocity $\beta = 0.064$

The data analysis is equal to the analysis at low velocity. The lasers for the high velocity measurement are locked also to iodine transitions. For the parallel beam the transition P(13)43-1 a_3 is used. In [JCH$^+$02] the frequency is given for an iodine cell at -5°C$\hat{=}$2.4 Pa with a pressure shift of -2.5 ± 0.5 kHz/Pa. A second measurement [GAKL$^+$04] confirms the results. The frequency at a temperature of 6°C is given in table 7.3.

The antiparallel laser beam uses the transition P(10)14-1 a_{15} at 585 nm(s. appendix B). The heterodyne frequency is in the range of 514 MHz (s. figure 7.42) and must be added to the frequency of the iodine stabilized dye laser. All frequencies are given in table 7.4 and the measured values at high velocity are shown in figure 7.43. The final extrapolated value is $(546\ 466\ 918\ 455 \pm 69)$ kHz for PM2 and $(546\ 466\ 918\ 483 \pm 77)$

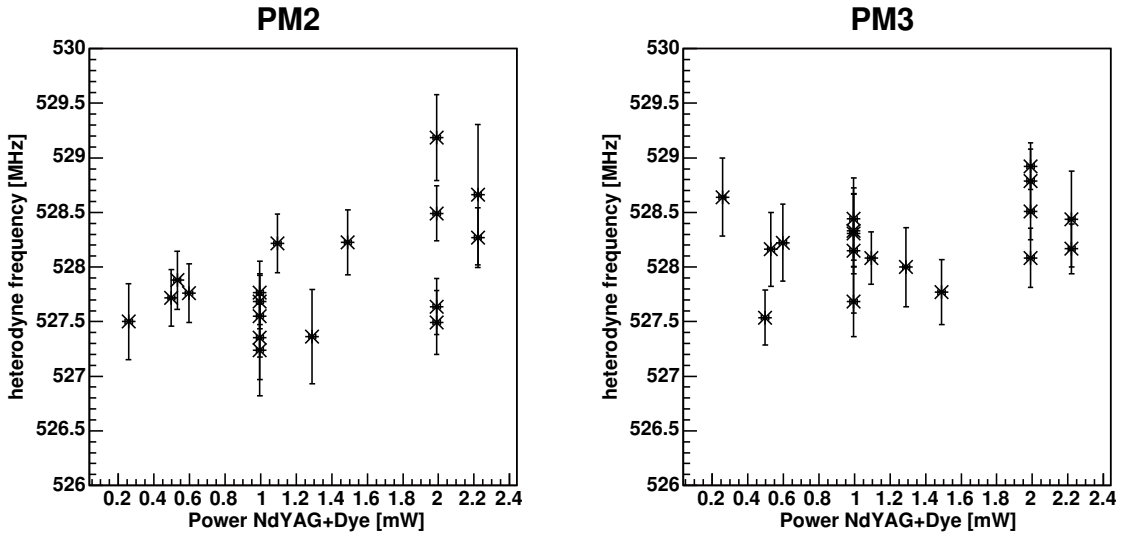

Figure 7.40: Measured values of the Lamb dip position ν_{beat} as a function of the laser power ($\beta = 0.03$, measurement 2.).

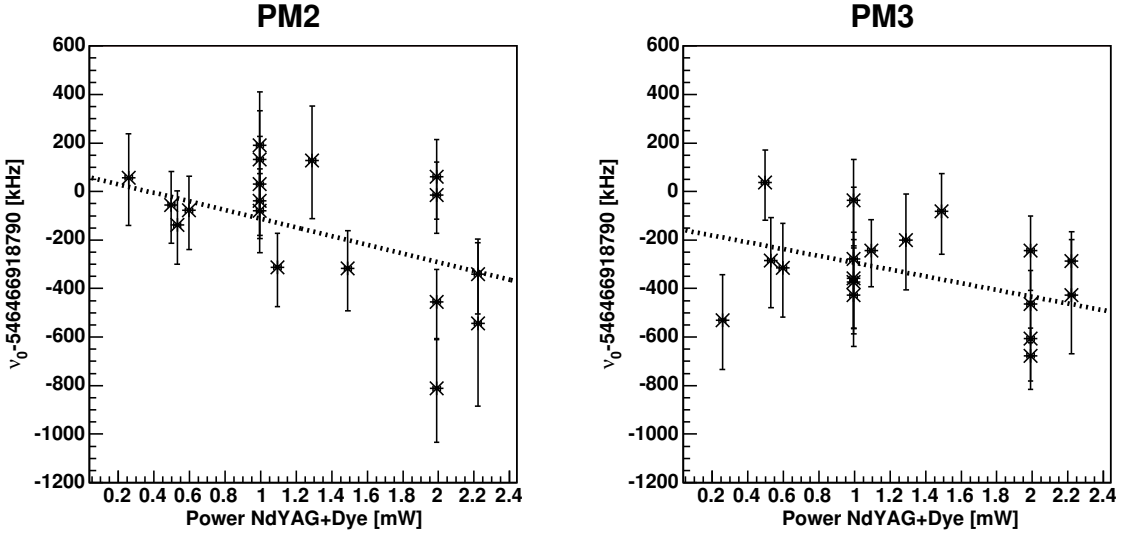

Figure 7.41: Measurement values of ν_{01} containing the line-position uncertainty of the Lamb dip and b_{uncorr} ($\beta = 0.03$, measurement 2.).

contribute	value	uncertainty
P(13)43-1 a_3 [JCH$^+$02]	582 490 603 442 kHz	2 kHz
P(13)43-1 a_3 [GAKL$^+$04]	582 490 603 443 kHz	1 kHz
pressure difference	5.0 Pa	
frequency shift due pressure	−13 kHz	3 kHz
P(13)43-1 a_1	582 490 603 430 kHz	3 kHz

Table 7.3: Determination of transition frequency of P(13)43-1 a_3 at $6°C$. The rounded mean value of the measurements is taken.

antiparallel beam	value [kHz]	uncertainty [kHz]
iodine line P(10)14-1 a_{15}	512 671 028 075	73
AOM of spectroscopy	$-80\,000/2$	< 1
AOM for switching	$-200\,000$	< 1
ion beam divergence	50	50
$\nu_{a2} - \nu_{beat}$	512 670 788 125	88
parallel beam		
iodine line P(13))43-1 a_3	582 490 603 430	3
lock uncertainty	–	73
AOM of spectroscopy	$-80\,000/2$	< 1
AOM for switching	$-200\,000$	< 1
ν_{p2}	582 490 363 430	73
b_{corr} PM2:	-186	141
b_{corr} PM3:	-62	
b_{uncorr} single measurement	–	$^{+300}_{-150}$
b_{uncorr} extrapolated value	–	100
magnetic fields PM2:	–	50
magnetic fields PM3:		50
light pressure shift PM2:	-59	59
light pressure shift PM3:	-35	35

Table 7.4: The frequencies and 1σ-uncertainties contributing to the determinations of ν_{02} ($\beta = 0.064$).

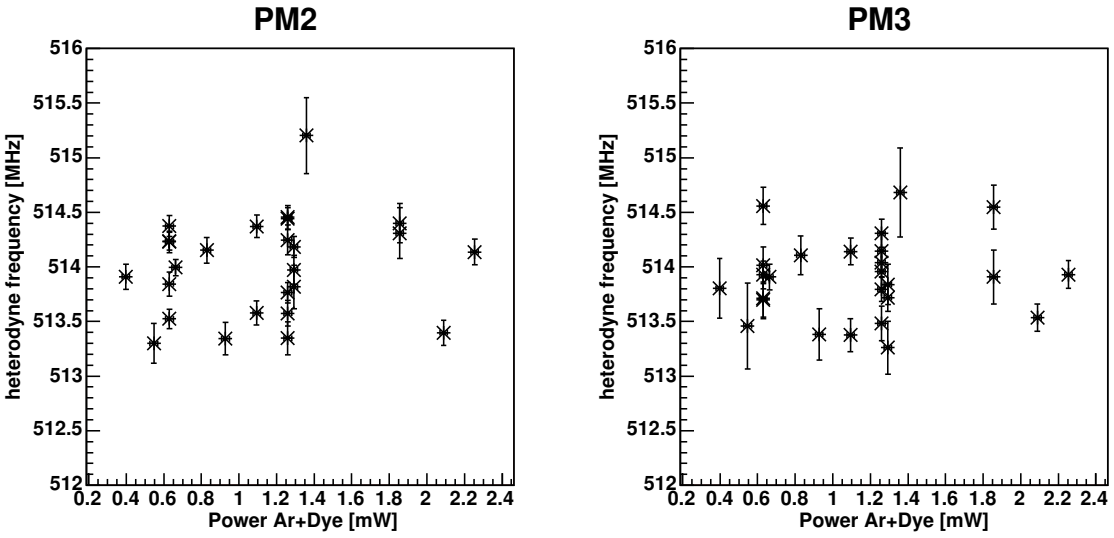

Figure 7.42: Measured values of the Lamb dip position ν_{beat} as a function of the laser power ($\beta = 0.064$).

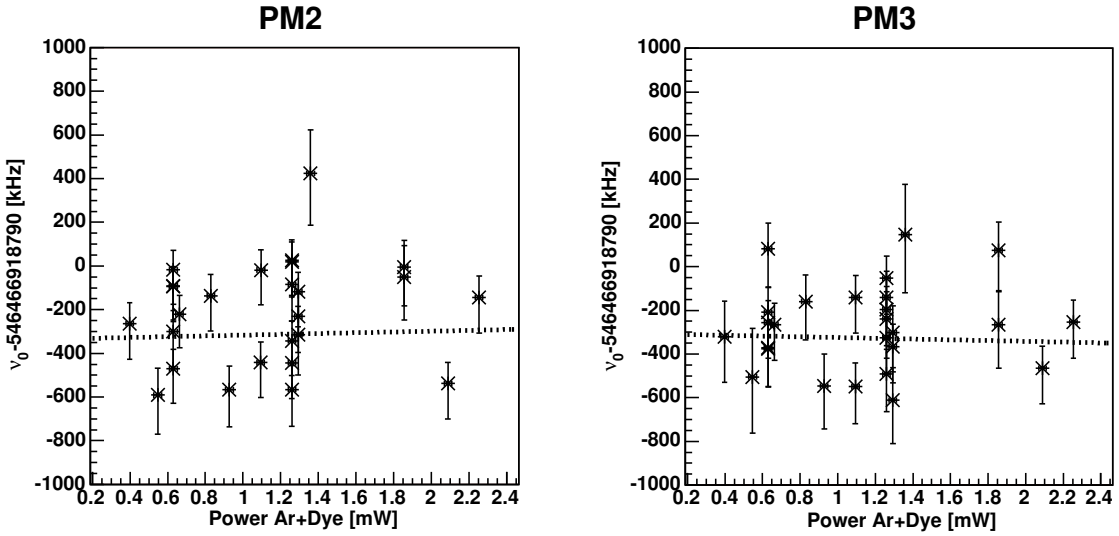

Figure 7.43: Measurement values of ν_{02} containing the line-position uncertainty of the Lamb dip and b_{uncorr} ($\beta = 0.064$).

kHz for PM3. The values obtained after the correction of b_{corr} are

$$\text{PM2} : \nu_{02} = (546\ 466\ 918\ 548 \pm 99)\ \text{kHz} \quad (7.18)$$
$$\text{PM3} : \nu_{02} = (546\ 466\ 918\ 526 \pm 104)\ \text{kHz}. \quad (7.19)$$

The difference between the two frequencies is (22 ± 144) kHz, so here the two measured frequencies are equal in the range of the given uncertainties . The final frequency values ν_{02} with all known uncertainties included are

$$\nu_{02}^{PM2} = (546\ 466\ 918\ 489 \pm 147)\ \text{kHz} \quad (7.20)$$
$$\nu_{02}^{PM3} = (546\ 466\ 918\ 491 \pm 143)\ \text{kHz} \quad (7.21)$$

7.7.3 Verification of the phasefrontcorrection ($\beta = 0.064$)

With the laser beam profiles given in section 7.4.3, which are intended to produce large phasefront shifts, some frequencies measurements are carried out. The results in terms of rest frequency ν_{02} are plotted in figure 7.44. The extrapolated values are $(546\ 466\ 917\ 920 \pm 179)$ kHz for PM2 and $(546\ 466\ 917\ 733 \pm 211)$ kHz for PM3. Compared with the corresponding values given in the previous section the values are about 700 kHz to small. The values corrected by b_{corr} are (s. section 7.4.3).

$$\text{PM2} : \nu_{02} = (546\ 466\ 918\ 570 \pm 235)\ \text{kHz} \quad (7.22)$$
$$\text{PM3} : \nu_{02} = (546\ 466\ 918\ 633 \pm 292)\ \text{kHz}. \quad (7.23)$$

These values agree with the corrected values (eqs. 7.18 and 7.19) of the previous section indicates that the on-axis phasefront correction are well under control.

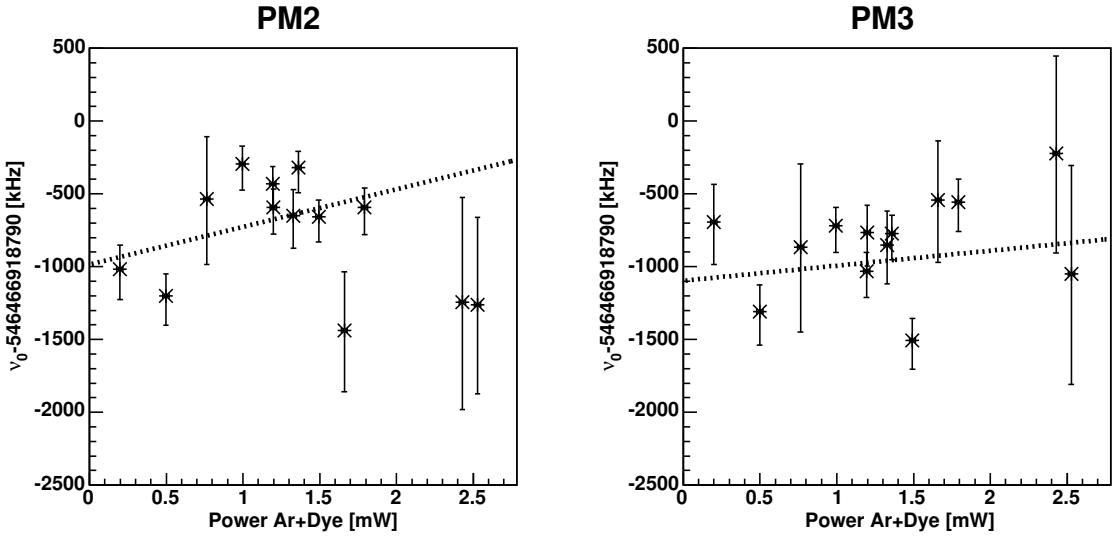

Figure 7.44: Measured rest frequency as a function of laser power, when the focus of the parallel beam is placed near the position of PM3 ($\beta = 0.064$).

The final frequency values ν_{02} with all known uncertainties (s. table 7.4, the same values are used except for the b_{uncorr} part, here see section 7.4.3) included are

$$\nu_{02}^{PM2} = (546\ 466\ 918\ 511 \pm 265)\ \text{kHz} \quad (7.24)$$

$$\nu_{02}^{PM3} = (546\ 466\ 918\ 598 \pm 313)\ \text{kHz} \quad (7.25)$$

7.7.4 Analysis of older measurements

The measurement in [SKE+03] is reanalyzed using the more precise iodine frequencies now available and applying a small additional uncertainty due to the magnetic field effects and the shift introduced by the light force (s. table 7.5). Applying the same procedure as before the final value for the measured frequency at PM3 of the lithium ion is

$$\nu_{02}^{PM3} = (546\ 466\ 918\ 658 \pm 374)\ \text{kHz}. \quad (7.26)$$

This value agrees with the measurements of this work.

7.8 Determination of α and ν_0

Because two measurements made at two different velocities, $\hat{\alpha}$ and ν_0 can be determined separately. In table 7.6 all measured frequencies are compiled. It can be noted that all final values of ν_{0i} (which include all error sources) obtained at the two velocities are consisting which each other. All these values will be included to determine $\hat{\alpha}$ and ν_0. To proper distinguished between statistical and various systematic uncertainties the averaged values ν_{01} and ν_{02} are determined in several steps (s. table 7.7 for $\beta = 0.03$

antiparallel beam	value [kHz]	uncertainty [kHz]
iodine line P(10)14-1 a_{15}	512 671 028 078	73
AOM for switching	414 000	< 1
ion beam divergence	–	50
frequency calibration	–	50
laser-laser angle	–	40
laser-ion angle	–	10
offset Lamb dip	1 550	460
ν_{a1}	512 671 443 628	473
parallel beam		
iodine line P(13))43-1 a_3	582 490 603 430	3
lock uncertainty	–	61
AOM for switching	−400 000	< 1
ν_{p1}	582 490 203 430	70
b_{corr} only PM3	486	175
magnetic fields	–	50
light pressure shift	−35	35

Table 7.5: Uncertainties for the reanalyzed data measured in [SKE+03] ($\beta = 0.064$).

measurement	b_{corr} value [kHz]	final value [kHz]
$\beta = 0.03$	measurement 1. (1)	
PM2	546 466 918 888 ± 51	546 466 918 724 ± 270
PM3	546 466 918 717 ± 56	546 466 918 607 ± 146
$\beta = 0.03$	measurement 2. (2)	
PM2	546 466 918 930 ± 96	546 466 918 766 ± 282
PM3	546 466 918 674 ± 101	546 466 918 564 ± 168
$\beta = 0.064$	normal measurement (3)	
PM2	546 466 918 548 ± 99	546 466 918 489 ± 147
PM3	546 466 918 526 ± 104	546 466 918 491 ± 143
$\beta = 0.064$	measurement for verification (4)	
PM2	546 466 918 570 ± 235	546 466 918 511 ± 265
PM3	546 466 918 633 ± 292	546 466 918 598 ± 313
$\beta = 0.064$	reanalyzed value (5)	
PM3		546 466 918 658 ± 374

Table 7.6: Overview of all measured frequencies ν_{0i} (1σ uncertainty). The different measurements are numbered for distinction.

and in table 7.8 for $\beta = 0.064$). To the uncertainty of the b_{corr} corrected ν_{0i} values (step 0.) the uncertainty of b_{uncorr} is included in (step 1.), from which the weighted mean for each photomultiplier and velocity is determined (step 2.) then the corrections due to the light pressure and magnetic fields are applied (step 3.) and the results for PM2 and PM3 are averaged (step 4.) and finally the uncertainties of the laser frequencies are included (step 5.). The measured transition frequency for $\beta = 0.03$ is thus

$$\nu_{01} = (546\ 466\ 918\ 624 \pm 130)\ \text{kHz}. \tag{7.27}$$

For the high velocity ($\beta = 0.064$) the value of the reanalyzed measurement from [SKE+03] (s. eq. 7.26) and the value obtained in this work are averaged. The weighted mean is

$$\nu_{02} = (546\ 466\ 918\ 511 \pm 102)\ \text{kHz}. \tag{7.28}$$

Using eq. 2.44 and eq. 2.45 with the values given in eqs. 7.27 and 7.28 $\hat{\alpha}$ and ν_0 are

$$\begin{aligned} \hat{\alpha} &= (-6.5 \pm 9.5) \cdot 10^{-8} \\ \nu_0 &= (546\ 466\ 918\ 656 \pm 169)\ \text{kHz}. \end{aligned}$$

If it is assumed, that Special Relativity is correct, a more precise value ν_0^{SR} for the transition frequency of the transition $2^3\mathrm{S}_1(F = 5/2) \rightarrow 2^3\mathrm{P}_2(F = 7/2)$ in the $^7\mathrm{Li}^+$-ion can be calculated by averaging the obtained frequency at low (eq. 7.27) and high (eq. 7.28) velocity. The weighted mean is

$$\nu_0^{SR} = (546\ 466\ 918\ 554 \pm 80)\ \text{kHz}. \tag{7.29}$$

	$\beta = 0.03$			
	PM2		PM3	
measurement	(1)[kHz]	(2)[kHz]	(1)[kHz]	(2)[kHz]
step 0.	546 466 918 888 ± 51	546 466 918 930 ± 96	546 466 918 717 ± 56	546 466 918 674 ± 101
step 1.	546 466 918 888 ± 57	546 466 918 930 ± 99	546 466 918 717 ± 61	546 466 918 674 ± 104
step 2.	546 466 918 898 ± 49		546 466 918 706 ± 53	
step 3.	546 466 918 734 ± 263		546 466 918 596 ± 132	
step 4.	546 466 918 624 ± 118			
step 5.	546 466 918 624 ± 130			

Table 7.7: Calculating the mean value ν_{01} for $\beta = 0.03$

	$\beta = 0.064$			
	PM2		PM3	
measurement	(3)[kHz]	(4)[kHz]	(3)[kHz]	(4)[kHz]
step 0.	546 466 918 548 ± 99	546 466 918 570 ± 235	546 466 918 526 ± 104	546 466 918 633 ± 292
step 1.	546 466 918 548 ± 111	546 466 918 570 ± 247	546 466 918 526 ± 115	546 466 918 633 ± 301
step 2.	546 466 918 552 ± 101		546 466 918 540 ± 108	
step 3.	546 466 918 493 ± 127		546 466 918 505 ± 124	
step 4.	546 466 918 499 ± 88			
step 5.	546 466 918 499 ± 106			

Table 7.8: Calculating the mean value ν_{02} for $\beta = 0.064$.

Chapter 8

Conclusion and outlook

8.1 Conclusion

In the current work measurements were carried out to improve the understanding of spectroscopy of fast stored lithium ions and sensitivity on the parameter $\hat{\alpha}$, which describes a modification on the time dilation compared to Special Relativity.

The setup used allows a spectroscopy with high controllability and sensitivity. The frequencies of all lasers are known to a value of 10^{-10} all the time and are controlled on the same level. Thus the statistical uncertainty of the Lamb dip frequency for a single measurement could be pushed down to about 150 kHz, which is two to three times better than previous measurements [Saa02]. Moreover, the phasefront corrections were shown to work as expected within the given uncertainties.

The laser power dependence of the transition frequency of the lithium ion is strongly reduced by faster switching between the different states of the lasers. A possible way to a better understand of the light force effects is to switch the lasers in phase with the ion movement in the ring as it is explained in [Mer00] in order to control the interaction time between ions and lasers. Also a modification in the switching scheme of the lasers, e. g. first applying the states where only one laser interacts with the ions instead of the state where both lasers interact with the ions, would be conceivable to confirm some of our conjectures, because no overcompensation at high switching frequencies would be expected in this case.

The influence of magnetics fields on the transition frequency is not negligible even if linear polarized light is used. Due to asymmetric population of the Zeeman states in the ground level, a line shift can be generated as soon as a small magnetic field (< 1 Gauss) is present. By changing the polarization of the laser light it is possible to detect potential magnetic fields. An interesting measurement would be a repetition of the experiment on $^6Li^+$, which has roughly the same transition-frequencies so the same lasers can be used at the same ion velocity. Because of the even nuclear spin of the nucleus, the hyperfine-structure levels with total angular momentum of zero are available. Transitions from the F=0 to F=1 state cannot be influenced by an asymmetric population of the ground level, because it has only one sublevel. By applying an external magnetic field over the whole interaction length single Zeeman sublevels could be excited. However, since the

$F = 0 \rightarrow F = 1$ transition is not a closed two level system and an additional repump mechanism (for example a laser) has to be applied in these measurements, because the upper state can decay in other hyperfine states $F = 1$ and $F = 2$ as well.

Two measurements of the transition frequency of the lithium ion have been done at two different velocities to determine the rest frequency ν_0, which was not precisely enough known[RSP+94], independently of $\hat{\alpha}$. The combined measurements at $\beta = 0.03$ and $\beta = 0.064$ lead to a transition frequency at rest with 1σ-uncertainty of

$$\nu_0 \quad = \quad (546\ 466\ 918\ 656 \pm 169)\ \text{kHz}$$

and to a $\hat{\alpha}$ of

$$\hat{\alpha} \quad = \quad (-6.5 \pm 9.5) \cdot 10^{-8}.$$

The value of $\hat{\alpha}$ is in the 1σ uncertainty and it is compatible to zero so no deviation to Special Relativity is observed. Compared to the best previous measurement $|\hat{\alpha}| < 2.2 \cdot 10^{-7}$ [SKE+03] the sensitivity on $\hat{\alpha}$ is improved by more than a factor of two.

The frequency of the transition $2^3\mathrm{S}_1(F = 5/2) \rightarrow 2^3\mathrm{P}_2(F = 7/2)$ of the $^7\mathrm{Li}^+$-ion is confirmed with an uncertainty of below 200 kHz, if a $\hat{\alpha} \neq 0$ is allowed. If it is assumed that Special Relativity is valid ($\hat{\alpha} = 0$), the uncertainty of the transition frequency is below 100 kHz

$$\nu_0^{SR} \quad = \quad (546\ 466\ 918\ 554 \pm 80)\ \text{kHz}.$$

All measured transition frequencies confirms the best known value of (546 466 918 790 ± 400) kHz [RSP+94].

A further improvement of the experiment on the TSR would require a better understanding of the influence of velocities changes and light forces on the line shape and a possibility to measure and perhaps modify the magnetic field in the whole experimental section during a measurement. Also the alignment of the laser and ion beam needs to be improved for further improvement.

8.2 Outlook

Beyond the suggestions in the previous subsection, an experiment at considerably higher velocity is prepared at the Gesellschaft für Schwerionenforschung (GSI) in Darmstadt using the Experimentierspeicherring (ESR). The ESR has a circumference of 108 m with a maximum bending power of 10 Tm, which allows a maximum velocity of $\beta = 0.42$ for $^7\mathrm{Li}^+$. Using $\beta = 0.34$, the sensitivity to $\hat{\alpha}$ is increased by a factor of 28 compared to the measurements at $\beta = 0.064$, if the uncertainties of the Lamb dip frequency measurement can be conserved (Because many systematic uncertainties depend also on the ion velocity, the increase in sensitivity is expected to be some what smaller but still sizeable).

The wavelength required for the parallel laser is 386 nm and for the antiparallel laser 780 nm. The antiparallel laser is locked to a transition of Rubidium and the parallel laser is the doubled frequency of a laser, that is locked to a reference of a molecular iodine line

as in the current experiment. An optical frequency comb generator [HUH$^+$00] will be used to measure the laser frequencies all the time to verify that the frequency is known with a accuracy of at least 10^{-10}. The alignment between the lasers and the ions must be better than the alignment in the current work, because this uncertainties scales at least linearly with the velocity. The goal of the ESR measurement is a sensitivity of $5 \cdot 10^{-9}$ for $\hat{\alpha}$.

Appendix A

Polarization of light

The polarization of light can be given in a linear base or in a circular base (details in textbooks like [KF88]). It is now discussed how the polarization of a linearly polarized light beam changes, if it travels through a quarter wave plate under angle ψ relative to the fast axis of the wave plate. The linear light can be described as

$$E_x = E_0 \cos\psi \cos(\omega t) \tag{A.1}$$
$$E_y = E_0 \sin\psi \cos(\omega t). \tag{A.2}$$

After the light has traveled through the wave plate, the components of the electric field are

$$E'_x = E_0 \cos\psi \cos(\omega t) \tag{A.3}$$
$$E'_y = E_0 \sin\psi \cos(\omega t - \pi/2) = E_0 \sin\psi \sin(\omega t). \tag{A.4}$$

For $\psi > 0$ the light is called left elliptically polarized light and if $\psi < 0$ the light is called right elliptically polarized light.
Light is called circularly polarized light, if the amplitude in x and y axis are equal and the phase between them differs by $\pm\pi/2$. For $+\pi/2$ the light is called right circularly polarized light and for $-\pi/2$ the light is called left circularly polarized light. In a linear base the circularly polarized light is given by

$$E_x = E_c \cos(\omega t) \tag{A.5}$$
$$E_y = E_c \cos(\omega t \pm \pi/2) = \mp E_c \sin(\omega t). \tag{A.6}$$

For the Zeeman splitting and optical pumping investigations in this work an interesting point is the ratio of the left and right circularly polarized light as a function the angle ψ between the incoming linear polarized light and the fast axis of the quarter wave plate. Now the linearly polarized light can be given in the base of circularly polarized light. The x component is the sum of left and right circular light components, that have no phase difference. The y component is the sum of left and right circular light components that have a phase difference of π. The amplitude for the x and y axis after the quarter

wave plate are

$$\underbrace{E_0 \cos\psi}_{A_x} = E_c^L + E_c^R \tag{A.7}$$

$$\underbrace{E_0 \sin\psi}_{A_y} = E_c^L - E_c^R. \tag{A.8}$$

The amplitudes of the left and right circularly polarized light are

$$E_c^L = \frac{A_x + A_y}{2} \tag{A.9}$$

$$E_c^R = \frac{A_x - A_y}{2}. \tag{A.10}$$

The ratio of left and right circularly polarized light is

$$\frac{E_c^L}{E_c^R} = \frac{A_x + A_y}{A_x - A_y} \tag{A.11}$$

$$\Rightarrow = \frac{\cos\psi + \sin\psi}{\cos\psi - \sin\psi}. \tag{A.12}$$

For the case of $\psi = \pi/4$ the ratio is infinite, so the light is fully left circularly polarized as expected. For the spectroscopy, the ratio of the intensities is interesting

$$\left(\frac{E_c^L}{E_c^R}\right)^2 = \frac{1 + \sin(2\psi)}{1 - \sin(2\psi)}. \tag{A.13}$$

The sum of the circularly polarized intensities must be equal to the incoming intensity E_0^2. The intensities for the circularly polarized lights are

$$(E_c^L)^2 = \frac{E_0^2}{2}(1 + \sin(2\psi)) \tag{A.14}$$

$$(E_c^R)^2 = \frac{E_0^2}{2}(1 - \sin(2\psi)). \tag{A.15}$$

Appendix B

Absolute frequency measurements in $^{127}I_2$

The frequency of all lasers used in the experiment are determined by a hyperfine-structure transition of the molecular iodine. Iodine is a recommended secondary frequency standard of the International Committee for Weights and Measures (CIPM) [Qui03], and a few transitions are known up to an uncertainty level of 10^{-11} in the frequency range of 500 nm to 650 nm. The reason is, that iodine has a rich strong absorption spectrum[1] at an easy to reach temperature range of -15 to 15°C with a moderate vapour pressure, thus the effects of pressure broadening and shift are small. The vapour pressure can be approximated by the formula given in [Bax15]

$$\log(p) \quad = \quad 9.7522 - \frac{2863,54}{T-19}. \tag{B.1}$$

T is the temperature of the vapour in Kelvin and p is the vapour pressure in Torr. The vapour pressure at 0°C is 4.1 Pascal or 0.031 Torr. The pressure shift is normally below 10 kHz/Pa. The natural linewidth of a hyperfine transition is of the order of 100 kHz [BCD79]. For the used pressure at 6°C this linewidth is increased to 2 MHz. This is small enough to stabilize a laser to better than 10^{-10} in frequency. Also the sensitivity to external magnetic fields is very small and of the order of 10^{-13} per Gauss [GGKSC91][GNS96].

The nomenclature of an electronic $X^1\Sigma_g^+ \rightarrow B^3\Pi_{0_u^+}$ transition is of the structure A(J')v"-v'. A can be P, if the rotational quantum of the excited state J" is bigger by one compared to the rotational quantum number J' of the ground state, and R, if J" is smaller by one. v" is the vibrational quantum number of the excited state and v' is the vibrational quantum number of the lower state. Because the molecule is homonuclear and the iodine atom has a nuclear spin of 5/2 there are selection rules. Due to the nuclear spin, a single transition is split into several hyperfine-structure levels. For even rotational quantum numbers J' 15 and for odd J' 21 hyperfine-structure lines are expected. The hyperfine-structure components are marked by a_x, where x starts with 1 for the transition with the lowest frequency and is increased by one for every additional line at higher frequencies.

[1] more than 50000 rovibronical transitions

The frequencies of the transitions for the parallel laser beams are already known to high degree of accuracy. The transitions, that are used for antiparallel beams, must be measured for the experiment. The transition P(10)14-1 a_{15} at 585 nm is already known to a level of 150 kHz [Rei02] and was used in [SKE$^+$03]. The transition P(80)21-1 a_{10} at 565 nm is only known to an accuracy of 1.6 MHz given in the Doppler-free iodine atlas [Kat00] and this too large for the time dilation experiment. The absolute frequencies for both transitions are measured separately by a self-referenced frequency comb at the Max Planck Institute of Quantum Optics [HUH$^+$00].

B.1 Frequency comb and principle of measurement

The self-referenced frequency comb is today the tool for frequency measurements in the optical region. The advantage is that the cesium time standard with a frequency of 9.192631770 GHz can be directly compared to an optical frequency. The principle of operation is that a comb of frequencies with a well known spacing between adjacent comb lines is generated by a femtosecond laser, whose spectrum is broadened by a photonic fiber so that the comb is spanning an octave. The frequency doubled red end can then be directly compared to the blue end of the comb. This is necessary to determine the offset frequency of the comb due to the phase shift of the carrier envelope phase from pulse to pulse (s. figure B.1). The frequency of a mode of the comb is given by

$$\nu_n = f_o + n f_r. \tag{B.2}$$

The offset frequency f_o is of the order of 37 to 80 MHz and the repetition frequency

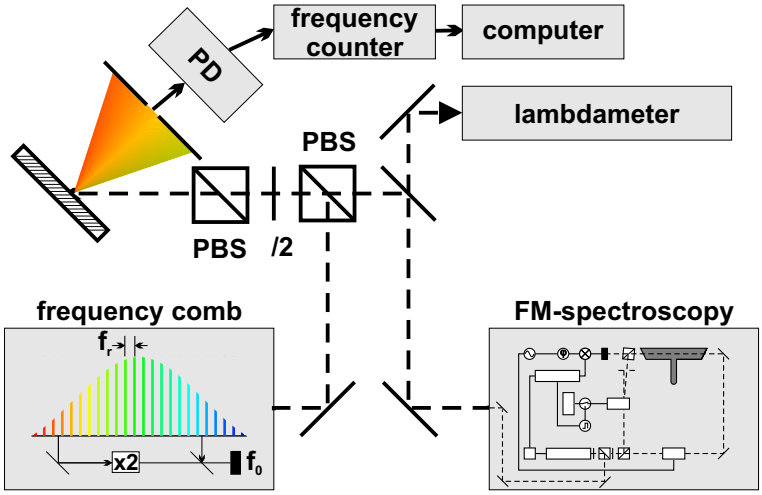

Figure B.1: Principle of a frequency measurement with a frequency comb.

f_r of the femtosecond laser is 800 MHz. These frequencies can be easily compared and controlled to the primary time standard. To measure the frequency of a laser, the heterodyne frequency between the laser and the nearest mode ν_n is measured. The mode number n is normally determined by a wavemeter, that has a resolution better than the repetition rate.

B.2 Frequency measurements

The laser is stabilized as it is explained in chapter 5 and overlapped with light of the frequency comb. Because the line P(80)21-1 a_{10} was never measured before to this accuracy, the complete transition is shown in figure B.2. The measured absolute

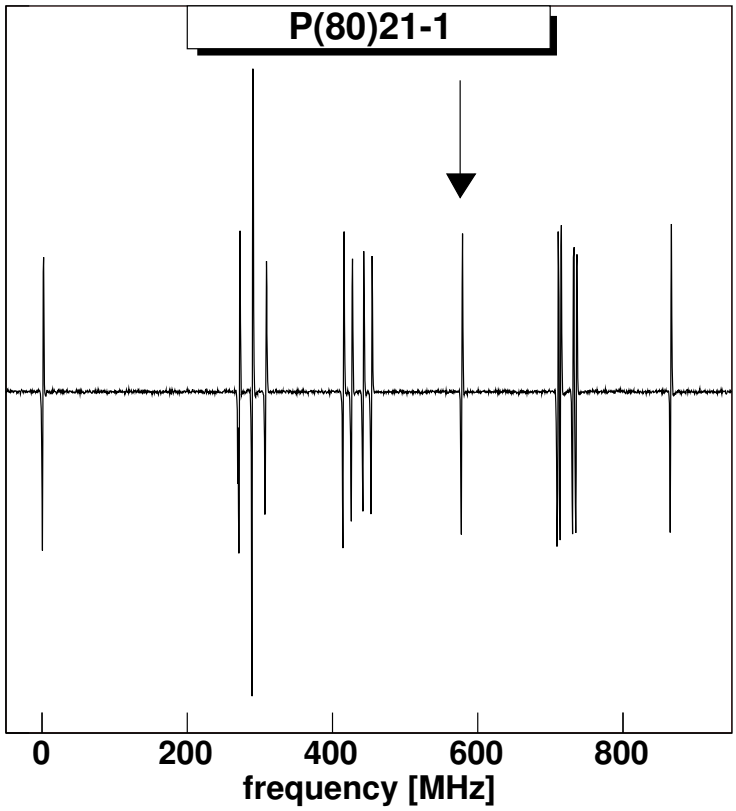

Figure B.2: Overview over the transition P(80)21-1. The line a_{10} is indicated by an arrow. Some lines are not resolved, but six separated groups of lines containing 1, 4, 4, 1, 4 and 1 lines are shown (from left to right).

frequencies of the two transitions can be given at a iodine cell temperature of 6°C to

$$\begin{aligned} \text{585 nm: P(10)14-1}\nu_{a15} &= (512\ 671\ 028\ 075 \pm 73)\text{kHz} \\ \text{565 nm: P(80)21-1}\nu_{a10} &= (530\ 222\ 434\ 291 \pm 73)\text{kHz}. \end{aligned}$$

The main uncertainty is due to instabilities of the used electronics for the laser stabilization. The frequency at 585 nm can also be measured by measuring the frequency difference of a laser stabilized to the transition R(99)15-1 a_{13}, that absolute frequency is known by another measurement [GBDH94], and a laser stabilized to P(10)14-1 a_{15}. The result of this measurement is $(3\ 405\ 290 \pm 30)$ kHz and this leads to an absolute frequency of $(512\ 671\ 028\ 067 \pm 73)$ kHz, which is equal to the frequency comb measurements. This is also an indicator that the used stabilization system does not generate a

significant frequency offset that could cause possible deviations in the measured transition frequency of the lithium ion at different velocities. A detailed description of the frequency measurements is published separately [RSK$^+$05].

Bibliography

[AB93] Arie, Ady ; Byer, Robert L.: Laser heterodyne spectroscopy of $^{127}I_2$ hyperfine structure near 532 nm. In: *J. Opt. Soc. Am. B* 10 (1993), November, Nr. 11, S. 1990–1997

[ACM00] Artoni, M. ; Carusotto, I. ; Minardi, F.: Light-force-induced fluorescence line-center shifts in high-precision optical spectroscopy: Simple model and experiment. In: *Physical Review A* 62 (2000), S. 023402/1–8

[AOGS05] Antonini, P. ; Okhapkin, M. ; Göklü, E. ; Schiller, S.: Test of constancy of speed of light with rotating cryogenic optical resonators. In: *Physical Review A* 71 (2005), S. 050101/1–4

[Bax15] Baxter: In: *J. Am. Chem. Soc.* 37 (1915), 1061 S

[BBC+77] Bailey, J. ; Borer, K. ; Combley, F. ; Drumm, H. ; Krienen, F. ; Lange, F. ; Picasso, E. ; Ruden, W. von ; Farley, F. J. M. ; Field, J. H. ; Flegel, W. ; Hattersley, P. M.: Measurements of relativistic time dilatation for positive and negative muons in a circular orbit. In: *Nature* 268 (1977), S. 301–305

[BCD79] Bordé, C. J. ; Camy, G. ; Decomps, B.: Measurement of the recoil shift of saturation resonances of $^{127}I_2$ at 5145 Å: A test of accuarcy for high-resolution saturation spectroscopy. In: *Physical Review A* 20 (1979), July, Nr. 1, S. 254–268

[Beu00] Beutelspacher, Michael: *Systematische Untersuchungen zur Elektronenkühlung am Heidelberger Speicherring TSR*, University Heidelberg, Diss., 2000

[BL75] Bjorkholm, J. E. ; Liao, P. F.: Optically Induced Atomic Energy Level Shifts and Two-Photon Spectroscopy. In: Haroche, S. (Hrsg.) ; Pebay-Peyroula, J. C. (Hrsg.) ; Hänsch, T. W. (Hrsg.) ; Harris, S. E. (Hrsg.): *Laser Spectroscopy*, Springer, 1975 (Lecture Notes in Physics 43), S. 176–185

[BL83] Bjorklund, G. C. ; Leveson, M. D.: Frequency Modulation (FM) Spectroscopy. In: *Applied Physics B* 32 (1983), S. 145–152

[Bou85] Boussard, D.: *Advanced Accelerator Physics*. CERN, 1985 (CERN Accelerator School)

[CGS00] Cordinale, P. ; Galzerano, G. ; Schnatz, H.: International comparision of two iodine-stabilized frequency-doubled Nd:YAG lasers at λ=532 nm. In: *Metrologia* 37 (2000), S. 177–182

[CIK63] Champeney, D. C. ; Isaac, G. R. ; Kahn, A. M.: An aether drift experiment based on the Mössbauer effect. In: *Physics Letters* 7 (1963), S. 241–243. – The similar announced [Isa70] but unpublished work of G. R. Isaak claims a upper limit of 10^{-7} for $\hat{\alpha}$

[CK97] Colladay, D. ; Kostelecký, V. A.: CPT violation and the standard model. In: *Phys. Rev. D* 55 (1997), S. 6760–6774

[CK98] Colladay, D. ; Kostelecký, V. A.: Lorentz-violating extension of the standard model. In: *Phys. Rev. D* 58 (1998), S. 116002/1–23

[CS02] Chernenko, A. A. ; Shishaev, A. V.: Light-pressure-unduced line-shape of the saturation resonance dip in an atomic gas. In: *Optics Communication* 211 (2002), October, S. 249–255

[CW03] Clarke, J. J. ; Wijngaarden, W. A.: Hyperfine and fine-structure measurements of $^{6,7}Li^{+}$ 1s2s ^{3}S and 1s2p ^{3}P states. In: *Physical Review A* 67 (2003), S. 012506/1–5

[Dem03] Demtröder, W.: *Laser Spectroscopy*. 3. Springer, 2003

[Dra66] Drake, G. W. F.: *Atomic, Molecular and Optical Physics Handbook*. AID Press, 1966

[Ein05] Einstein, Albert: Zur Elektrodynamik bewegter Körper. In: *Annalen der Physik* (1905), S. 891–921

[Eis98] Eisenbarth, Udo: *Kühlung hochenergetischer Ionenstrahlen am Speicherring TSR: neuartige Bunchformen und Raumladungseffekte*, University of Heidelberg, Diplomarbeit, 1998

[Gab94] Gabrysch, Mathias: *Chirpkomensation durch elektrooptische Phasenmodulation bei gepulsten Farbstofflaserverstärkern*, University Heidelberg, Diplomarbeit, 1994

[GAKL+04] Goncharov, A. ; Amy-Klein, A. ; Lopez, O. ; Burck, F. D. ; Chardonnet, C.: Absolute frequency measurement of the iodine-stabilized Ar^{+} laser at 514.6 nm using a femtosecond optical frequency comb. In: *Applied Physics B* 78 (2004), S. 725–731

[GB85] Gehrtz, Manfred ; Bjorklund, Gary C.: Quantum-limited laser frequency-modulation spectroscopy. In: *J. Opt. Soc. Am. B* 2 (1985), September, Nr. 9, S. 1510–1525

[GBD+94] Grieser, R. ; Bönsch, G. ; Dickopf, S. ; Klaft, I. ; Knobloch, P. ; Merz, P. ; Albrecht, F. ; Grieser, M. ; Habs, D. ; Schwalm, D. ; Kühl, T.: A test of special relativity with stored lithium ions. In: *Applied Physcis B* 59 (1994), S. 127–133

[GBDH94] Grieser, R. ; Bönsch, G. ; Dickopf, S. ; Huber, G.: Precision measurement of two iodine lines at 585 nm and 549 nm. In: *Zeitschrift für Physik A* 348 (1994), S. 147–150

[GGKSC91] Goncharov, A. N. ; Gateva-Kosteva, S. V. ; Skvortsov, M. N. ; Chebotayev, V. P.: Direct Observation of the Anomalous Zeeman Effect at the $X \rightarrow B$ Transition of Molecular Iodine by the Method of Nonlinear Laser Spectroscopy. In: *Applied Physics B* 52 (1991), S. 311–314

[GM89a] Grimm, R. ; Mlynek, J.: The Effect of Resonant Light Pressure in Saturation Spectroscopy. In: *Applied Physics B* 49 (1989), S. 179–189

[GM89b] Grimm, Rudolf ; Mlynek, Jürgen: Light-Pressure-Induced Line-Shape Asymmetry of the Saturation Dip in an Atomic Gas. In: *Physical Review Letters* 63 (1989), July, Nr. 3, S. 232–235

[GM90] Grimm, Rudolf ; Mylnek, Jürgen: Light-pressure-induced nonlinear dispersion of a laser field interacting with an atomic gas. In: *Physcial Review A* 42 (1990), September, Nr. 2, S. 2890–2905

[GNS96] Goncharov, A. N. ; Nevsky, A. Y. ; Skvortsov, M. N.: Second-order Zeeman effect of the $X \rightarrow B$ transition in molecular iodine. In: *Applied Physics B* 62 (1996), S. 427–430

[Gri] Grieser, M.: *Private Communication*

[Gri94] Grieser, Ralf: *Test der lokalen Lorentz-Invarianz am Heidelberger Testspeicherring*, University of Mainz, Diss., 1994

[Gwi05] Gwinner, Gerald: Experimental Tests of Time Dilation in Special Relativity. In: *Modern Physics Letters A* 20 (2005), March, Nr. 11, S. 791–805

[HBB+89] Habs, D. ; Baumann, W. ; Berger, J. ; Blatt, P. ; Faulstich, A. ; Krause, P. ; Kilgus, G. ; Neumann, R. ; Petrich, W. ; Stokstad, R. ; Schwalm, D. ; Szmola, E. ; Welti, K. ; Wolf, A. ; Zwickler, S. ; Jaeschke, E. ; Krämer, D. ; Bisoffi, G. ; Blum, M. ; Friedrich, A. ; Geyer, C. ; Grieser, M. ; Heyng, H. W. ; Holzer, B. ; Ihde, R. ; Jung, M. ; Matl, K. ; Ott, W. ; Povh, B. ; Repnow, R. ; Steck, M. ; Steffens, E. ; Dutta, D. ; Kühl, T. ; Marx, D. ; Schröder, S. ; Gerhard, M. ; Grieser, R. ; Huber, G. ; Klein, R. ; Krieg, M. ; Schmidt, N. ; Schuch, R. ; Babb, J. F. ; Spruch, L. ; Arnold, W. ; Noda, A.: First Experiments with the Heidelberg Test Storage Ring TSR. In: *Nuclear Instruments and Methods in Physics Research B* 43 (1989), S. 390–410

[HHBR81] Hall, J. L. ; Hollberg, L. ; Baer, T. ; Robinson, H. G.: Optical heterodyne saturation spectroscopy. In: *Appl. Phys. Lett.* 39 (1981), November, Nr. 9, S. 680–682

[HOW+05] Hollberg, L. ; Oates, C. W. ; Wilpers, G. ; Hoyt, C. W. ; Barber, Z. W. ; Diddams, S. A. ; Oskay, W. H. ; Bergquist, J. C.: Optical frequency/wavelength references. In: *Journal of Physics B* 38 (2005), S. 469–495

[HUH+00] Holzwart, R. ; Udem, Th. ; Hänsch, T. W. ; Knight, J. C. ; Wadsworth, W. J. ; Russel, P. St. J.: Optical Frequency Synthesizer for Prescision Spectroscopy. In: *Physical Review Letters* 85 (2000), Nr. 11, S. 2264–2267

[IS38] Ives, H. E. ; Stilwell, G. R.: An Experimental Study of the Rate of a Moving Atmoic Clock. In: *Journal of the Optical Society of America* 28 (1938), July, Nr. 7, S. 215–226

[Isa70] Isaak, G. R.: In: *Phys. Bull.* 21 (1970), 255 S

[JC98] Jaatinen, E. ; Chartier, J.-M.: Possible influence of residual amplitude modulation when using modulation transfer with iodine transition at 543 nm. In: *Metrologia* 35 (1998), S. 75–81

[JCH+02] Jones, R. J. ; Cheng, W.-Y. ; Holman, K. W. ; Chen, L. ; Hall, J. L. ; Ye, J.: Absolute-frequency measurement of the iodine-based standard at 514.67 nm. In: *Applied Physics B* 74 (2002), S. 597–601

[Kat00] Katô, Hajime: *Doppler-Free High Resolution Spectral Atlas of iodine Moleculae 15000 to 19000 cm^{-1}*. Japan Society for the promotion of science, 2000

[KF88] Klein, Miless V. ; Furtak, Thomas E.: *Optik*. Springer, 1988

[Kle91] Klein, Roman: *Präzisionsspektroskopie an gekühlten Li^+ Ionen im Schwerionenspeicherring als experimenteller Test der speziellen Relativitätstheorie*, University of Mainz, Diss., November 1991

[KM02] Kostelecký, V. A. ; Mewes, Matthew: Signals for Lorentz Violation in Electrodynamics. In: *Phys. Rev. D* 66 (2002), S. 056005/1–24

[KNN+83] Kowalski, J. ; Neumann, R. ; Noehte, S. ; Suhr, H. ; Putlitz, G. zu ; Herman, R.: Triplet-Singlet Interaction in the 1s 2s $^3S_1$ Hyperfine Splitting of He-Like Li^+. In: *Zeitschrift für Physik A* 313 (1983), S. 147–150

[KPR85] Kaivola, Matti ; Poulsen, Ove ; Riis, Erling: Measurement of the Relativistic Doppler Shift in Neon. In: *Physical Review Letters* 54 (1985), January, Nr. 4, S. 255–258

[Kre92] Kretzschmar, M.: Doppler spectroscopy on relativistic particle beams in the light of a test theory of special relativity. In: *Zeitschrift für Physik A* 342 (1992), Nr. 4, S. 463–469

[Lan05] Lane, Chales D.: Probing Lorentz violation with Doppler-shift experiemnts. In: *Physical Review D* 72 (2005), S. 016005/1–9

[Let76] Letokhov, V. S.: Saturation Spectroscopy. In: Shimoda, K. (Hrsg.): *High-Resolution Laser Spectroscopy*. Springer, 1976 (Topics in Applied Physics), Kapitel 4, S. 95–165

[Mac86] MacArthur, D. W.: Special relativity: Understanding experimental tests and formulations. In: *Physical Review A* 33 (1986), January, Nr. 1, S. 1–3

[MACI99] Minardi, F. ; Artoni, M. ; Cancio, P. ; Inguscio, M.: Frequency shift in saturation spectroscopy induced by mechanical effects of light. In: *Physical Review A* 60 (1999), Nr. 5, S. 4164–4167

[MBC+86] MacArthur, D. W. ; Butterfield, K. B. ; Clark, D. A. ; Donahue, J. B. ; Gram, P. A. M.: Test of the Special-Relativistic Doppler Formula at $\beta = 0.84$. In: *Physical Review Letters* 56 (1986), January, Nr. 4, S. 282–285

[McK79] McKinley, John M.: Relativistic transformations of light power. In: *Am. J. Phys. 47(7)* (1979), July, S. 602–605

[Mer00] Merz, Peter: *Präparation eines reinen metastabilen $^7Li^+$-Ionenstrahl für die Präzisionsspektroskopie im Speicherring*, University of Mainz, Diss., 2000

[Mes99] Meschede, D.: *Optik, Licht und Laser*. Teubner, 1999

[MGSL93] McGowan, Roger W. ; Giltner, David M. ; Sternberg, Scott J. ; Lee, Siu A.: New Measurement of the realtivistic Doppler Shift in Neon. In: *Physical Review Letter* 70 (1993), January, Nr. 3, S. 251–254

[MK97] Mayer-Kuckuk, T.: *Atomphysik*. 5. B. G. Teubner, 1997

[MS77a] Mansouri, Reza ; Sexl, Roman U.: A Test Theory of Special Relativity: I. Simultaneity and Clock Synchronization. In: *General Relativity and Gravitation* 8 (1977), Nr. 7, S. 497–513

[MS77b] Mansouri, Reza ; Sexl, Roman U.: A Test Theory of Special Relativity: II. First Order Tests. In: *General Relativity and Gravitation* 8 (1977), Nr. 7, S. 515–524

[MS77c] Mansouri, Reza ; Sexl, Roman U.: A Test Theory of Special Relativity: III. Second-Order Tests. In: *General Relativity and Gravitation* 8 (1977), Nr. 10, S. 809–814

[Pot90] Poth, H.: Electron cooling: Theory, experiment, application. In: *Physics Reports* (1990), S. 196

[Qui03] Quinn, T. J.: Practical realization of the definition of the metre, including recommended radiations of other optical frequency standards (2001). In: *Metrologia* 40 (2003), S. 103–133

[RABP88] Riis, Erling ; Andersen, Lars-Ulrik A. ; Bjerre, Nis ; Poulsen, Ove: Test of the Isotropy of the Speed of Light Using Fast-Beam Laser Spectroscopy. In: *Physical Review Letters* 60 (1988), January, Nr. 2, S. 81–84

[RCGW04] Ritt, G. ; Cennini, G. ; Geckeler, C. ; Weitz, M.: Laser frequency offset locking using a side of filter technique. In: *Applied Physics B* 79 (2004), S. 363–365

[Rei02] Reinhardt, Sascha: *Frequenzmessung im $^{127}I_2$-Spektrum bei 585 nm*, University of Heidelberg, Diplomarbeit, 2002

[RGK+98] Rong, H. ; Grafström, S. ; Kowalski, J. ; Neumann, R. ; Putlitz, G. zu: A new precise value of the absolute 2^3S_1, $F = 5/2 - 2^3P_2$, $F = 7/2$ transition frequency in $^7Li^+$. In: *The European Physcial Journal D* 3 (1998), S. 217–222

[Rob49] Robertson, H. P.: Postulate versus Observation in the Special Theory of Relativity. In: *Review of Modern Physics* 21 (1949), S. 378

[RSK+05] Reinhardt, S. ; Saathoff, G. ; Karpuk, S. ; Novotny, C. ; Huber, G. ; Zimmermann, M. ; Holzwarth, R. ; Udem, Th. ; Hänsch, T. ; Gwinner, G.: Planed to published in Optics Communications. (2005)

[RSP+94] Riis, E. ; Sinclair, A. G. ; Poulson, O. ; Drake, G. W. F. ; Rowley, W. R. C. ; Levick, A. P.: Lamb shifts and hyperfine structure in $^6Li^+$ and $^7Li^+$: Theory and Experiment. In: *Physical Review A* 49 (1994), January, Nr. 1, S. 207–220

[Saa02] Saathoff, Guido: *Experimental Test of Relativistic Time Dilation by Laser Spectroscopy of Fast Ions*, University of Heidelberg, Diss., November 2002

[Sag99] Saghiri, A. A.: *Hochauflösende Messung zur dielektronischen Rekombination von metastabilen und Grundzustand-Li^+-Ionen.*, University Heidelberg, Diss., 1999

[SEWZ99] Schünemann, U. ; Engler, H. ; Weidemüller, M. ; Zielonkowski, M.: Simple scheme for tunable frequency offset locking of two lasers. In: *Review of Scientific Instruments* 70 (1999), Nr. 1, S. 242–243

[SJ63] Szöke, A. ; Javan, A.: Isotope shift and saturation behaviour of the 1.15-μ transition of Ne. In: *Physical Review Letters* 10 (1963), Nr. 12, S. 521–524

[SKE+03] Saathoff, Guido ; Karpuk, S. ; Eisenbarth, U. ; Huber, G. ; Krohn, S. ; Horta, R. M. ; Reinhardt, S. ; Schwalm, D. ; Wolf, A. ; Gwinner, G.: Improved Test of Time Dilation in Special Relativity. In: *Physical Review Letters* 91 (2003), Nr. 19, S. 190403/1–4

[SLO+04] Sprenger, F. ; Lestinsky, M. ; Orlov, D. A. ; Schwalm, D. ; Wolf, A.: The high-resolution electron-ion collision facility at TSR. In: *Nuclear Instruments and Methods in Physics Research Section A* 532 (2004), S. 298–302

[SRBD80] Snyder, J. J. ; Raj, R. K. ; Bloch, D. ; Ducloy, M.: High-sensitivity nonlinear spectroscopy using a frequency-offset pump. In: *Optics Letters* 5 (1980), Nr. 4, S. 163–165

[SS83] Sexl, Roman ; Schmidt, Herbert K.: *Raum-Zeit-Relativität*. vieweg, 1983

[SS04] Sun, Xuan ; Scime, Earl: Measurement of Asymmetric Optical Pumping of Ions Accelerating in a Magnetic-Field Gradient. In: *Physical Review Letters* 93 (2004), S. 235002/1–4

[ST91] Saleh, B. E. A. ; Teich, M. C.: *Fundamentals of Photonics*. John Wiley & Sons, Inc., 1991

[STW+05] Stanwix, Paul L. ; Tobar, Micheal E. ; Wolf, Peter ; Susli, Mohama ; Locke, Clayton R. ; Ivanov, Eugene N. ; Winterflood, John ; Kann, Frank van: Test of the Lorentz Invariance in Electrodynamics Using Rotating Cryogenic Sapphire Microwave Oscillators. In: *Physical Review Letters* 95 (2005), S. 040404/1–4

[TWFH05] Tobar, Michael E. ; Wolf, Peter ; Fowler, Alison ; Hartnett, John G.: New methods of testing Lorentz violation in electrodynamics. In: *Physical Review D* 71 (2005), S. 025004/1–15

[WGG+98] Wanner, B. ; Grimm, R. ; Gruber, A. ; Habs, D. ; Miesner, H.-J. ; Nielsen, J. S. ; Schwalm, D.: Rapid adiabatic passage in laser coooling of fast stored ion beams. In: *Physical Review A* 58 (1998), Nr. 3, S. 2242–2251

[Wil92a] Will, Clifford M.: Clock synchronization and isotropy of the one-way speed of light. In: *Physical Review D* 45 (1992), January, Nr. 2, S. 403–411

[Wil92b] Wille, K.: *Physik der Teilchenbeschleuniger und Synchrotronstrahlungsquellen*. Teubner, 1992

[WP97] Wolf, Peter ; Petit, Gerard: Satillite test of special relativity using the global positiong system. In: *Physical Review A* 56 (1997), December, Nr. 6, S. 4405–4409

[WTB+04] Wolf, Peter ; Tobar, Michael E. ; Bize, Sébastian ; Clairon, André ; Luiten, André N. ; Santarelli, Giorgio: Whispering Gallery Resonators and Tests of Lorentz Invariance. In: *General Relativity and Gravitation* 36 (2004), Nr. 10, S. 2351–2372

[Zha97] Zhang, Yuan Z.: *Special Relativity and its experimental foundations.* World Scientific, 1997 (Advanced Series on Theoretical Science)